



Michigan Technological University
Create the Future Digital Commons @ Michigan Tech

Dissertations, Master's Theses and Master's
Reports - Open

Dissertations, Master's Theses and Master's
Reports

2013

NANOSCALE ELECTROCHEMISTRY BY IN-SITU TRANSMISSION ELECTRON MICROSCOPY

Qi Gao

Michigan Technological University

Follow this and additional works at: <https://digitalcommons.mtu.edu/etds>



Part of the [Nanoscience and Nanotechnology Commons](#), and the [Power and Energy Commons](#)

Copyright 2013 Qi Gao

Recommended Citation

Gao, Qi, "NANOSCALE ELECTROCHEMISTRY BY IN-SITU TRANSMISSION ELECTRON MICROSCOPY",
Dissertation, Michigan Technological University, 2013.
<https://doi.org/10.37099/mtu.dc.etds/649>

Follow this and additional works at: <https://digitalcommons.mtu.edu/etds>



Part of the [Nanoscience and Nanotechnology Commons](#), and the [Power and Energy Commons](#)

NANOSCALE ELECTROCHEMISTRY BY *IN-SITU* TRANSMISSION ELECTRON
MICROSCOPY

By

Qi Gao

A DISSERTATION

Submitted in partial fulfillment of the requirements for the degree of

DOCTOR OF PHILOSOPHY

In Mechanical Engineering-Engineering Mechanics

MICHIGAN TECHNOLOGICAL UNIVERSITY

2013

This dissertation has been approved in partial fulfillment of the requirements for the Degree of DOCTOR OF PHILOSOPHY in Mechanical Engineering-Engineering Mechanics.

Department of Mechanical Engineering-Engineering Mechanics

Dissertation Advisor: *Reza Shahbazian Yassar*

Committee Member: *Desheng Meng*

Committee Member: *Kazuya Tajiri*

Committee Member: *Patricia A Heiden*

Department Chair: *William W. Predebon*

Table of Content

Table of Content	3
List of Figures	6
List of Tables	12
Preface.....	13
Acknowledgments.....	15
Abstract	17
1. Introduction.....	19
1.1. Battery Development Throughout the Years.....	19
1.2. Lithium Ion Batteries.....	21
1.3. Titanium Dioxide Materials	24
1.4. Amorphous TiO ₂ as anodes for Li-ion Batteries	27
1.5. The Order of Chapters in the PhD Dissertation	30
2. Experimental Method.....	34
2.1. TiO ₂ Nanotube Synthesis	34
2.2. <i>In Situ</i> TEM Setup.....	36
3. Effect of Processing Parameters on the Physical Characteristics of Anodized TiO ₂ Nanotubes	38
3.1. Introduction	38
3.2. Experimental Procedure	40
3.3. Result and Discussion	41
3.3.1. Mechanism of TiO ₂ Nanotubes Formation	41
3.3.2. Anodization Current-Voltage Behavior	43
3.3.3. The Effect of Anodization Time on the Diameter of Nanotubes	45
3.3.4. The Effect of Anodization Voltage on the Diameter of Nanotubes	46
3.3.5. The Effect of Anodization Time on the Length of Nanotubes	49
3.3.6. The Effect of Anodization Voltage on the Length of Nanotubes	51
3.4. Conclusion.....	53
4. Structural Instabilities in TiO ₂ Nanotubes	54
4.1. Introduction	54
4.2. Experimental Procedure	56
4.2.1. Synthesis	56
4.2.2. Characterization	57
4.3. Results	57
4.4. Discussion	66
4.5. Conclusions	68

5. A Real Time Observation of Phase Transition of Anatase TiO ₂ Nanotubes into Rutile Nanoparticles by In-Situ Joule Heating Inside Transmission Electron Microscope	70
5.1. Introduction	70
5.2. Experimental Procedure	71
5.3. Results Discussion.....	72
5.4. Conclusion.....	81
6. A Study on the Modulation of the Electrical Transport by Mechanical Straining of Individual Titanium Dioxide Nanotube	83
6.1. Introduction	83
6.2. Experimental Procedure	84
6.3. Results Discussion.....	84
6.4. Conclusion.....	92
7. Deformation-Driven Electrical Transport in Amorphous TiO ₂ Nanotubes	93
7.1. Introduction	93
7.2. Experimental section	95
7.3. Results and discussion.....	96
7.4. Conclusion.....	106
8. Evidence of Lithium-induced Atomic Ordering in Amorphous TiO ₂ Nanotubes	108
8.1. Introduction	108
8.2. EXPERIMENTAL METHODS	110
8.2.1. TiO ₂ Nanotube Synthesis	110
8.2.2. <i>In Situ</i> TEM Setup	111
8.3. RESULTS AND DISCUSSION	112
8.4. Conclusion.....	126
9. Conclusion	127
10. Future Work	130
10.1. <i>In Situ</i> Electrochemistry of Anatase TiO ₂ Nanotubes.....	130
10.2. <i>In Situ</i> Electrochemistry of TiO ₂ (B) Nanostructures	132
10.3. <i>In situ</i> Electrochemistry of Rutile TiO ₂ Nanostructures	135
References.....	140
Appendix A: The Delithiated and Electrical Behaviors of Individual Amorphous TiO ₂ Nanotubes.	177
A.1. Delithiation Process of Amorphous TNTs	177
A.2. Electrical Behavior of Amorphous TNTs	179
Appendix B: The Electrochemical Property of Si Nanowires	181
Appendix C: <i>In Situ</i> TEM Operation Procedure.....	185
C.1. Sample Preparation.....	185
C.2. Glove Box Operation.....	188

C.3. Nanofactory Software Setup	191
Appendix D: Copyright Permissions	195

List of Figures

Figure 1.1	The schematic picture of battery system.	19
Figure 1.2	Comparison of the different battery technologies in terms of volumetric and gravimetric energy density. ¹	20
Figure 1.3	The schematic picture of lithium ion battery with the positive electrode of LiCoO ₂ and negative electrode of carbon graphite. The green and blue arrows represent charge and discharge process, respectively.	22
Figure 1.4	Amorphous structures of TiO ₂ , (a) simulation structure, ¹⁶ and (b) TEM image. Anatase structures of TiO ₂ , (c) unit cell, and (d) HRTEM image showing the lattice structures.	26
Figure 1.5	The phase diagram of Li-Ti-O obtained using MaterialsProject.com.	27
Figure 1.6	Charge and discharge curves for amorphous TiO ₂ nanotube. ³² (a) the charge-discharge curves in various rate, (b) cycling performance and (c) coulomb efficiency of amorphous TiO ₂ at the current densities of 10 and 30 A g ⁻¹	29
Figure 2.1	(a) Anodization setup. (b) Schematic of synthesis process of TiO ₂ nanotubes. (c-d) FESEM images of surface and cross section views of TiO ₂ nanotubes.	35
Figure 2.2	(a) Configuration of <i>in situ</i> holder. (b) Experimental view of <i>in situ</i> holder in the TEM.	36
Figure 2.3	Schematic illustration of the <i>in situ</i> TEM setup for the lithiation/delithiation studies of amorphous TiO ₂ nanotubes. The nanotubes are placed on the STM tip that is biased negatively with respect to the Li/Li ₂ O counter electrode.	37
Figure 3.1	Schematic diagram of TiO ₂ nanotubes formation: (a) formation of oxide layer, (b) pore growth due to dissolution reaction, (c) nanotubes formation layer by layer, and (d) SEM image of bamboo-type nanotubes.	43
Figure 3.2	Current density (J-t) curves at three different anodization voltages.	44
Figure 3.3	FE-SEM images of the free end of the nanotubular structure obtained under 40 V after different anodization time (a) 4, (b) 8, and (c) 16 hrs. (d) The plot for diameter distribution of nanotubes. The average diameter was calculated to be 66, 67 and 74 nm for 4, 8 and 16 hours, respectively.	46

Figure 3.4	FE-SEM images of the tubular structures obtained after 16 hours anodization under different voltage: (a) 20 V, and (b) 60 V. (c) The plot for diameter distribution of nanotubes. The average diameter was 54, 74 and 144 nm for 20, 40 and 60 V, respectively.	47
Figure 3.5	The change in diameter of TiO ₂ nanotubes arrays as a function of anodization time and voltage.	49
Figure 3.6	The tubular structures under 60 V after various anodization time (a) 4, (b) 8, and (c) 16 hours, respectively.	50
Figure 3.7	The tubular structures after 16 hours anodization under different voltage: (a) 20, and (b) 40 V, respectively.	51
Figure 3.8	The change in length of TiO ₂ nanotubes arrays as a function of anodization time and voltage.	52
Figure 4.1	The SEM images of (a) as-synthesized TiO ₂ nanotubes arrays and (b) close of nanotubes shown in (a).	58
Figure 4.2	The bright field (a), diffraction pattern (b), and high resolution TEM (c) images of as-synthesized TiO ₂ nanotubes.	59
Figure 4.3	[(a) and (b)] The SEM images of TiO ₂ nanotubes treated by NH ₄ OH for 30 min.	59
Figure 4.4	(Color online) The SEM images show (a) as-synthesized TiO ₂ nanotubes after annealing in 500 °C. [(b) and (c)] The bright field TEM image and diffraction pattern of nanotubes shown in (a) indicate the transformation of amorphous morphology to crystalline order in the nanotubes. (d) The high resolution TEM image confirms the crystalline order of anatase phase and the presence of structural defects (appear as dark contrasts).	60
Figure 4.5	The SEM images show the morphology of the NH ₃ -treated TiO ₂ nanotubes after calcination at 500 °C for 2 h. The treated nanotubes collapsed into nanoparticles upon heat treatment at anatase phase transformation temperature.	61
Figure 4.6	The SEM images of NH ₄ OH-treated TiO ₂ nanotubes after 0(a), 10(b), and 30 (c) minutes of calcination at 500 °C. The treated nanotubes start to disintegrate into small particles.	62
Figure 4.7	(Color online) The XRD patterns of untreated and ammonium hydroxide [designated by (N)] TiO ₂ nanotubes.	63
Figure 4.8	The Raman spectroscopy of the Ti foil, untreated and ammonium hydroxide-treated TiO ₂ nanotubes. The A in parenthesis stands for anatase.	64

Figure 4.9	Bright field TEM images of nanoparticles after the collapse of TiO ₂ nanotubes by NH ₃ -treatment and annealing at 500 °C. The inset shows the diffraction pattern of particles and indicates that the crystal structure is anatase.....	65
Figure 4.10	(Color online) (a) The as-synthesized TiO ₂ nanotubes show imperfections on the surface (marked by the arrows). (b) The elastic modulus map of TiO ₂ nanotubes before immersion in the ammonia hydroxyl media is shown. The dark brownish color indicates areas of high stiffness and areas of bright yellowish correspond to low stiffness values. The scanned area is 500 nm and the color key represents qualitative comparison of the modulus.....	66
Figure 4.11	(Color online) A schematic of the observed structural instability in TiO ₂ nanotubes treated with NH ₄ OH and calcinated at 500 °C. The surface roughness is shown in the larger scale than the nanotube dimension. The nanotube disintegrated into anatase particles after 10 and 30 min of calcination but maintained the overall configuration of nanotube. After 2 h the nanotubes collapsed into nanoparticles.....	68
Figure 5.1	The image showing the experimental setup for STM-TEM holder.....	72
Figure 5.2	(a) TEM bright field (BF) image of the as-synthesized TiO ₂ nanotubes and its corresponding electron diffraction pattern (inset) and (b) the high resolution image.....	74
Figure 5.3	(a) An overall view of the anatase titania nanotube and the corresponding diffraction pattern (inset) and (b) the high resolution lattice image from a single anatase nanotube (inset).	74
Figure 5.4	Images from the FIB system showing (a) the as grown TiO ₂ nanotube sample; (b) FIB probe attached with a single nanotube dispersed on the Cu mesh (c) the FIB probe with a nanotube approaching the tip of the tungsten wire and (d) Schematic of the experimental setup for current–voltage measurement.	76
Figure 5.5	The BF image of the TiO ₂ nanotube (a) in contact with the STM tip (b) undergone the heat treatment at constant bias voltage of 10 V for 180 seconds (c) the bias heated at 20 V for 130 seconds (d) undergone the bias heating at 30 V.....	77
Figure 5.6	The current (I) versus time (t) plot for the TiO ₂ nanotube under the different bias heating voltages, as marked in the plot.....	78
Figure 5.7	(a) The high resolution lattice image and the corresponding diffraction pattern (inset) taken from TiO ₂ nanotube undergone a bias heating at 10 V (b) the high resolution lattice image of the nanotube bias heated at 20 V	

	and the corresponding diffraction pattern (inset) (c) The diffraction pattern from the agglomeration formed at the bias heating of 30 V.	79
Figure 6.1	(Color online) (a) An overall view of the anatase titania nanotube and the corresponding diffraction pattern (inset) and (b) the high resolution lattice image from a single anatase nanotube (inset).	85
Figure 6.2	Images from the FIB system show (a) the as grown TiO ₂ nanotube sample; (b) FIB probe attached with a single nanotube, dispersed on the Cu mesh; (c) the FIB probe with a nanotube approaching the tip of the tungsten wire and; (d) schematic of the experimental setup for current–voltage measurement.	86
Figure 6.3	(Color online) The bright field image of the TiO ₂ nanotube (a) approaching the STM tip; (b) in contact with the STM tip; [(c)–(e)] undergoing a gradual increase in its bending curvature; (f) a series of the representative <i>I</i> – <i>V</i> curves measured during the deformation of the TiO ₂ nanotubes.	88
Figure 6.4	(Color online) The <i>ln I</i> – <i>V</i> curves corresponding to (a) curve <i>d</i> and (b) curve <i>e</i> in Figure 6.3(f), respectively. (c) The linear fits of the curves in [(a) and (b)]	89
Figure 7.1	The image shows the experimental configuration for the STM–TEM holder (Nanofactory)	96
Figure 7.2	TEM bright field (BF) image of the amorphous TiO ₂ nanotubes and its corresponding electron diffraction pattern (inset)	97
Figure 7.3	Images from the FIB system showing (a) the as-grown TiO ₂ nanotube sample, (b) the FIB probe attached with a single nanotube, dispersed on the Cu mesh, (c) the FIB probe with a nanotube approaching the tip of the tungsten wire, (d) schematic of the experimental setup for current–voltage measurement.	98
Figure 7.4	The bright field image of a TiO ₂ nanotube (a) approaching the STM tip, (b) in contact with the STM tip, (c), (d), and (e) undergoing a gradual increase in the bending curvature, (f) a series of the representative <i>I</i> – <i>V</i> curves measured during the deformation of the TiO ₂ nanotubes.	100
Figure 7.5	The <i>ln I</i> – <i>V</i> curves corresponding to (a) curve c and (b) curve e in Figure 7.4(f), respectively. (c) The linear fits of the curves in (a) and (b).	103
Figure 8.1	Serial snapshot images of lithiation process for an individual a-TNT. (a) The whole structural view of a selected a-TNT with diameter of around 130 nm. (b–f) A selected area of lithiation process monitored from the reference 0s (b) to 1740s (f). The evolution of Li ₂ O layer formation is observed on the surface of the nanotube as marked by green arrow. The HRTEM images of Li ₂ O layer formation on the surface of an individual a-	

	TNT are shown as (g-i). (g) A pristine TiO_2 nanotube with diameter of 107 nm. (h) A thickness of 11 ± 2 nm layer formation on the lithiated nanotube. (i) Corresponding diffraction pattern of the Li_2O layer.	114
Figure 8.2	EELS spectra of Li <i>K</i> edge, Ti <i>L</i> edge and O <i>K</i> edge taken from the selected area of the nanotube before and after lithiation. (a) The EELS spectrums show Li <i>K</i> edge of pristine, lithiated TiO_2 nanotube, and Li_2O as a reference. (b) A comparison between Ti <i>L</i> edge in pristine and lithiated TiO_2 nanotubes is shown. (c) Showing O <i>K</i> edge in pristine and lithiated TiO_2 nanotubes.....	115
Figure 8.3	Bright field TEM images of an individual a-TNT (a) before lithiation, and (b) after lithiation. The white arrows in (a) and (b) indicate that the wall thickness increases from ~ 24 to ~ 26 nm during lithiation, while no obvious change is seen for the nanotube inner diameter (~ 59 nm). Several dark contrast particles are detected in the lithiated a-TNT (marked by white dotted circles in (b)). (c-d) Corresponding SAED patterns of pristine and lithiated a-TNTs. The nanotube is demonstrated to be amorphous before lithiation in (c). The electron diffraction rings in (d) are indexed to be Li_2O and $\text{Li}_2\text{Ti}_2\text{O}_4$, respectively.....	118
Figure 8.4	TEM images reveal the formation of $\text{Li}_2\text{Ti}_2\text{O}_4$ crystals within the amorphous matrix. (a) A zoom-out image of an area within lithiated amorphous TiO_2 where the presence of several crystalline particles are marked by white arrows. (b) A closer view of the crystalline particles shows the lattice fringes of crystalline particles. (c) High resolution TEM image of the particle marked by the red dotted box in (b) shows the atomic ordering within the crystalline particles. The particles are viewed along [001] zone axis and the interatomic distance of 2.09 Å was correlated to (400) planes in $\text{Li}_2\text{Ti}_2\text{O}_4$ crystals. (d-e) The existence of the crystalline particles within the lithiated amorphous matrix was also confirmed in other locations. (f) A unit cell of the $\text{Li}_2\text{Ti}_2\text{O}_4$ crystals viewed along [001] zone axis.....	121
Figure 8.5	The STEM-EELS mapping of an individual a-TNT before and after lithiation shows the chemical distribution of Ti, O and Li in the nanotube. A selected area of EELS mapping shows the uniform distribution of O and Ti before lithiation (a-d) and after lithiation (e-h). (i) Li distribution by EELS mapping indicating the successful lithiation in the nanotube. (j) EELS mapping of Li, O, and Ti in the lithiated nanotube, showing the Li ions distributing randomly in the matrix.....	123
Figure 8.6	(a) Three distinctive regions are captured during lithiation of a single a-TNT. In region (I), the nanotube is fully lithiated as evident by the formation of polycrystalline Li_2O layer and crystalline $\text{Li}_2\text{Ti}_2\text{O}_4$ islands. In region (II), the nanotube is partially lithiated as evident by the progressive	

	formation of Li_2O layer. No crystalline $\text{Li}_2\text{Ti}_2\text{O}_4$ islands could be detected. In region (III), the very end of the nanotube is still in pristine state (unlithiated). (b) The schematic graph shows various stages of lithiation process in a-TNTs.	125
Figure 10.1	(a) unit cell of anatase, (b) initial three charge/discharge curves of anatase TiO_2 nanotubes, ²⁵⁹ (c) capacity and coulomb efficiency of anatase TiO_2 nanotubes versus cycling numbers. ²⁵⁹	131
Figure 10.2	TiO_2 (B) crystal structure (a) TiO_6 octahedral unit cell, (b) lithium intercalation sites in the unit cell: A1, A2, and C, ²⁶⁶ (c-d) HRTEM images with corresponding diffraction pattern of TiO_2 (B) nanofibers. ²⁶⁷	133
Figure 10.3	(a) charge/discharge curves of TiO_2 (B) nanosheets under various rates, (b) cycling performance of TiO_2 (B) nanosheets. ²⁷⁰	135
Figure 10.4	(a) The unit cell of rutile TiO_2 , (b-d) HRTEM image of rutile nanorods with corresponding diffraction pattern, ²⁸⁰ (e) the charge/discharge curves of various sized rutile TiO_2 , ²⁷⁵ (f) electrochemical cycling of nanosized rutile TiO_2 under various rate. ²⁷⁵	137
Figure A.1	Snapshot images of the delithiation process for a selected area of a-TNT. (a-d) Delithiation process monitored from beginning (0s) to end (660s). (e-f) The high-magnification TEM images of delithiated an a-TNT show the existence of particles in the amorphous matrix. (g-h) EELS spectrums of Ti <i>L</i> edge and O <i>K</i> edge after delithiation are compared with the same signals from pristine and lithiated nanotubes, respectively.	178
Figure A.2	<i>I-V</i> curves of an individual a-TNT under the bias ranging from -25 V to 25 V. Each color represents the nanotube in different states: As-grown (black), 1 st lithiation (red), 1 st delithiation (blue), 2 nd lithiation (green), and 2 nd delithiation (pink).	180
Figure B.1	The volume expansion behavior of two different crystallographic orientations of Si nanowires. (a-d) isotropic volume expansion of individual Si nanowire with $\langle 111 \rangle$ orientation. (e-h) Anisotropic volume expansion of individual Si nanowire with $\langle 112 \rangle$ orientation.	182
Figure B.2	The cross section of various crystallographic orientations of Si nanowires with corresponding volume expansion of lithiated $\langle 100 \rangle$, ^{293, 294} $\langle 110 \rangle$, ^{293, 294} $\langle 111 \rangle$, and $\langle 112 \rangle$ nanowires.	183
Figure B.3	The delithiation process of individual Si nanowire. (a-d) shows the diameter of the nanowire shrunk back its original 85 nm.	184

List of Tables

Table 1.1 Anode materials in lithium ion batteries.....	23
Table 3.1 TiO ₂ Nanotubes Synthesized by Various Methods.....	39
Table 6.1 Electrical Parameters of TiO ₂ nanotube.....	91
Table 7.1 Electrical parameters of TiO ₂ nanotube	105

Preface

The publications presented in the dissertation have been part of research work carried out at Michigan Technological University, during my PhD in the period of 2008-2013. Mechanical, electrical, and electrochemical properties of TiO₂ nanotubes are studied.

Chapter 3 presents the effect of processing parameters on the physical characteristics of anodized TiO₂ nanotubes. Experiments were designed, conducted and analyzed by Mr. Qi Gao in the laboratory of Prof. Heiden. (Department of Chemistry, MTU). The distribution measurements of diameters were calculated by Mr. Nishit Parikh.

Chapter 4 presents the structural instability of TiO₂ nanotubes subjected to treatment with ammonium hydroxide solution prior to calcination at elevated temperatures. Mr. Qi Gao has designed and conducted the experiments of growing and characterizing TiO₂ nanotubes. Dr. Tolou Shokuhfar and Mr. Qi Gao collaborated to analyze the results. Parts of the experiments were conducted in the laboratory of Prof. Heiden.

Chapter 5 presents *in situ* Joule heating induced phase transformation of anatase TiO₂ nanotubes into rutile nanoparticles. Mr. Qi Gao has designed and conducted the experiments of growing TiO₂ nanotubes. Dr. Anjana Ashtana performed the *in situ* experiment and data analysis.

Chapter 6 presents the deformation-driven modulation of the electrical transport properties by mechanical straining of individual anatase TiO₂ nanotubes. Mr. Qi Gao has

designed and grown the TiO₂ nanotubes and participated in the results interpretation. Dr. Anjana Ashtana performed the *in situ* experiment and data analysis.

Chapter 7 presents the deformation-driven electrical transport in amorphous TiO₂ nanotubes. The study investigates the effect of mechanical deformation on the electrical transport properties of individual amorphous TiO₂ nanotubes. Mr. Qi Gao has designed and grown the TiO₂ nanotubes and participated in the results interpretation. Dr. Anjana Ashtana performed the *in situ* experiment and data analysis.

Chapter 8 presents the *in situ* electrochemical lithiation mechanism of individual amorphous TiO₂ nanotubes, showing the evidence of lithium-induced atomic ordering in the amorphous lithiated nanotubes matrix. Mr. Qi Gao has designed and grown the TiO₂ nanotubes, performed and interpreted the *in situ* results. Dr. Anmin Nie and Dr. Meng Gu (PNNL) have participated in conducting parts of the experiments and interpreting the results.

Acknowledgments

This PhD research project will not be finished without many people's help. I would like to express my great appreciation to my advisor, Prof. Reza Shahbazian Yassar, who insistently offered invaluable guidance, support and encouragement. I am heartily for his help of designing and developing the project, his patience of practicing my skills as a PhD, and his encouragement of overcoming the various difficulties in the project.

Additional thanks go to my committee members, Prof. Patritia Heiden, Prof. Desheng Meng, and Prof. Kazuya Tajiri, for helping me with their knowledge and assistance to conduct this project successfully. I also want to thanks my energy and nano science research group members, it was a great experience to work with them. Special thanks to Dr. Anjana Ashtana, Prof. Tolou Shokuhfar, Dr. Anmin Nie and Mr. Xiaochu Ding for the invaluable assistance. I would like to thank all my friends, making me feel like at home instead of in a foreign county. I also want to thank Mr. Owen Mills for his assistance in my work.

My deepest thanks go to my family for their endless love and constant support in my life. I could not finish this PhD degree without them. My wife, Huan Yang, keeps encouraging and supporting me when I was lost in my career. No matter what happened, she always believed me from the beginning to the end. Thanks to my mother and my mother in law for their financial support and love. The encouragement and support from my mother never changed since childhood, giving me the best environment to grow up

and letting me have the highest level of education. Her trust and love is the most valuable property in my life.

Qi Gao,

Michigan Technological University, Aug.2013

Abstract

Nanoscale research in energy storage has recently focused on investigating the properties of nanostructures in order to increase energy density, power rate, and capacity. To better understand the intrinsic properties of nanomaterials, a new and advanced *in situ* system was designed that allows atomic scale observation of materials under external fields. A special holder equipped with a scanning tunneling microscopy (STM) probe inside a transmission electron microscopy (TEM) system was used to perform the *in situ* studies on mechanical, electrical, and electrochemical properties of nanomaterials. The nanostructures of titanium dioxide (TiO_2) nanotubes are characterized by electron imaging, diffraction, and chemical analysis techniques inside TEM.

TiO_2 nanotube is one of the candidates as anode materials for lithium ion batteries. It is necessary to study their morphological, mechanical, electrical, and electrochemical properties at atomic level. The synthesis of TiO_2 nanotubes showed that the aspect ratio of TiO_2 could be controlled by processing parameters, such as anodization time and voltage. Ammonium hydroxide (NH_4OH) treated TiO_2 nanotubes showed unexpected instability. Observation revealed the nanotubes were disintegrated into nanoparticles and the tubular morphology was vanished after annealing. The nitrogen compounds incorporated in surface defects weaken the nanotube and result in the collapse of nanotube into nanoparticles during phase transformation. Next, the electrical and mechanical properties of TiO_2 nanotubes were studied by *in situ* TEM system. Phase transformation of anatase TiO_2 nanotubes into rutile nanoparticles was studied by *in situ*

Joule heating. The results showed that single anatase TiO_2 nanotubes broke into ultrafine small anatase nanoparticles. On further increasing the bias, the nanoclusters of anatase particles became prone to a solid state reaction and were grown into stable large rutile nanoparticles. The relationship between mechanical and electrical properties of TiO_2 nanotubes was also investigated. Initially, both anatase and amorphous TiO_2 nanotubes were characterized by using I - V test to demonstrate the semiconductor properties. The observation of mechanical bending on TiO_2 nanotubes revealed that the conductivity would increase when bending deformation happened. The defects on the nanotubes created by deformation helped electron transportation to increase the conductivity. Lastly, the electrochemical properties of amorphous TiO_2 nanotubes were characterized by *in situ* TEM system. The direct chemical and imaging evidence of lithium-induced atomic ordering in amorphous TiO_2 nanotubes was studied. The results indicated that the lithiation started with the valance reduction of Ti^{4+} to Ti^{3+} leading to a Li_xTiO_2 intercalation compound. The continued intercalation of Li ions in TiO_2 nanotubes triggered an amorphous to crystalline phase transformation. The crystals were formed as nano islands and identified to be $\text{Li}_2\text{Ti}_2\text{O}_4$ with cubic structure ($a = 8.375 \text{ \AA}$). This phase transformation is associated with local inhomogeneities in Li distribution. Based on these observations, a new reaction mechanism is proposed to explain the first cycle lithiation behavior in amorphous TiO_2 nanotubes

Chapter 1 Introduction

1.1. Battery Development Throughout the Years

Energy storage has been a hot topic in recent times, since the natural sources have been nearly depleted from the US Energy Information Administration (EIA). It is necessary to develop new and efficiency materials for energy storage. Batteries have been attracted much attention as one type of the energy storage systems. The principle of battery system is to convert stored chemical energy into electrical energy by electrochemical reduction-oxidation reactions.¹ There are two electrodes in the batteries; a positive electrode (cathode) and a negative electrode (anode), as well as electrolytes, which can be solid or liquid to contact both of the electrodes as a bridge as shown in Figure 1.1. The two electrodes will transfer energy through electrochemical reduction-oxidation reactions to release electrons to outer circuit load.

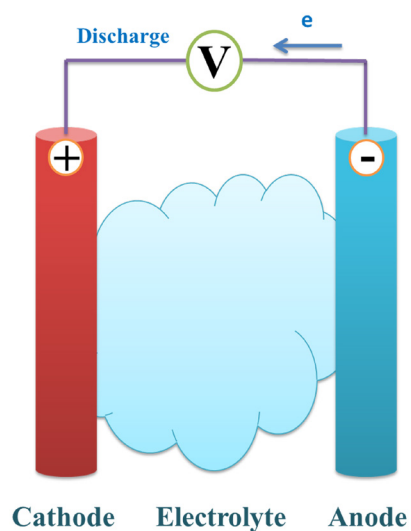


Figure 1.1 The schematic picture of battery system.

The battery, which consists of zinc as negative electrode, copper as positive electrode and sulfuric acid as electrolyte, was first invented by Alessandro Volta in 1800. Since then, many other types of battery systems have been developed as shown in Figure 1.2.

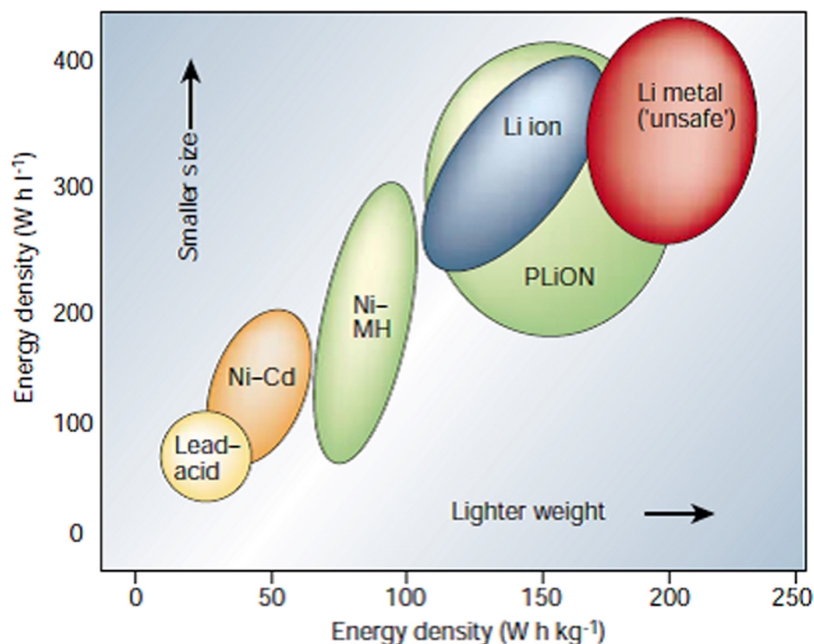


Figure 1.2 Comparison of the different battery technologies in terms of volumetric and gravimetric energy density.¹ (Reprint with the permission from Nature, 2001, 414, 359-367. Copyright, 2001, Nature Publishing Group)

Energy density, which is the amount of energy stored in the system, is one major criterion to evaluate the battery performance. Energy density is usually measured in two ways, mass and volume. Gravimetric energy density is measured by mass (m) and volumetric energy density is measured by volume (v). The energy in a battery is

determined by the time (t) of depth of discharge, the current (I) in the battery, and the voltage (V) in the system as shown in Equation (1.1).

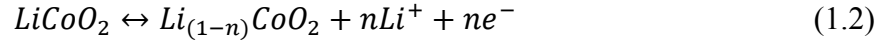
$$\text{Energy density} = \frac{I \times v \times t}{m \text{ or } v} \left(\frac{W \times h}{kg \text{ or } L} \right) \quad (1.1)$$

In Figure 1.2, from the known battery technologies of lead-acid, nickel-cadmium, nickel metal hydroxide and plastic-LiON, lithium batteries have the highest gravimetric energy density as well as the volumetric energy density. For lithium batteries, lithium metal was initially a good candidate as an anode material because of its light weight ($0.53 \text{ g}\cdot\text{cm}^{-3}$), high specific capacity ($3862 \text{ mAh}\cdot\text{g}^{-1}$), and highest operation voltage (-3.04 V). However it did not become widely used in market today because of the drawbacks of fast degradation and short circuit¹. In 1991, Sony developed the first lithium ion battery that used carbonaceous as electrodes, which could safely store lithium². After that, lithium ion battery becomes one of the most popular batteries in commercial world based on its light weight, small size, and high capacity.³

1.2. Lithium Ion Batteries

The scheme of lithium ion battery is shown in Figure 1.3, consisting of LiCoO_2 as cathode and carbon graphite as anode. When charging, the lithium ions will be produced by the positive electrode and move by force through an electrolyte to the negative electrode. LiCoO_2 produces lithium ions and graphite stores the lithium ions among layers. When discharging, the negative electrode will release electrons to load in outer circuit and the lithium ions will go back to the positive electrode. The reduction-oxidation reactions in both electrodes are shown below in Equation (1.2) and (1.3).

Positive electrode:



Negative electrode:

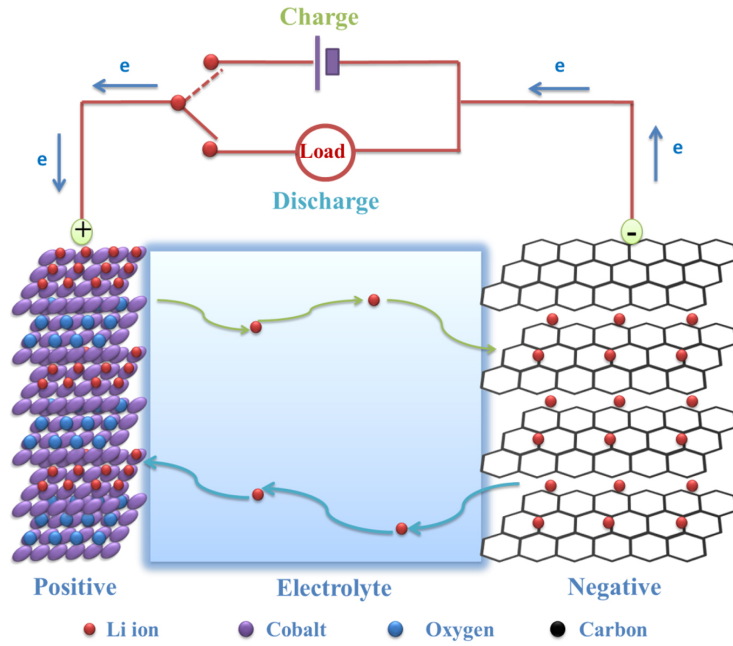


Figure 1.3 The schematic picture of lithium ion battery with the positive electrode of LiCoO_2 and negative electrode of carbon graphite. The green and blue arrows represent charge and discharge process, respectively.

However, with the increasing needs for new electronic devices and vehicles, how to increase the power and improve the performance of batteries has been an issue. Thus, the batteries are being modified through replacing electrode materials and electrolytes in order to increase the energy density. One way of fulfilling the goal is to change the anode

materials to improve the performance, including capacity and cycling life. In recent years, many new anode materials have been researched as listed in Table 1.1.

Table 1.1 Anode materials in lithium ion batteries.

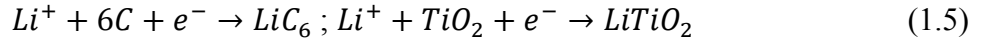
Anode Materials (fully lithiated phase)	Operating Voltage	Theoretical Capacity
Graphite (LiC_6)	0.1-0.2 V ⁴	372 mA·h/g
TiO_2 (LiTiO_2)	1-2 V ⁴	336 mA·h/g
Si ($\text{Li}_{4.4}\text{Si}$)	0.5-1 V ⁵	4212 mA·h/g
Ge ($\text{Li}_{4.4}\text{Ge}$)	0.7-1.2 V ⁶	1624 mA·h/g
Al(AlLi)	0.01-0.26 ⁷	993 mA·h/g
SnO_2 ($\text{Li}_{4.4}\text{Sn}$)	0.05-3 ^{8,9}	781 mA·h/g
ZnO ($\text{Li}_2\text{O}+\text{LiZn}$)	1.5-2.5 V ¹⁰	978 mA·h/g

In a battery, the overall voltage is decided by the potential difference between cathode and anode. When the cathode material is selected, the potential of anode material will determine the voltage of a battery. Table 1.1 lists several interesting anode materials, including their operational voltages versus Li/Li^+ and theoretical capacities. The operating voltage of anode materials is the voltage of initialing lithiation and delithiation reactions. At the operational voltage, lithium ions can insert into and exact from anode

materials. The theoretical capacity is the maximum amount of lithium ions that can be stored in anode materials. The value is calculated according to Equation (1.4).

$$\text{Theoretical capacity} = \frac{n \times F}{M} \left(\frac{c \times \text{mol}^{-1}}{g \times \text{mol}^{-1}} \right) = \frac{n \times F}{M} \left(\frac{A \times s}{g} \right) = \frac{n \times F}{M \times 3.6} \left(\frac{mA \times h}{g} \right) \quad (1.4)$$

In Equation (1.4), n is the number of ions (electrons transferred) involving in the lithiation reaction. F is the Faraday constant ($96485 \text{ C} \cdot \text{mol}^{-1}$) and M ($\text{g} \cdot \text{mol}^{-1}$) is the molar mass of the anode. Examples of calculations are listed in Equation (1.5).



For graphite, one Li^+ will react with 6 carbons to form LiC_6 . Based on Equation (1.5), n is 1 and M is $72 \text{ g} \cdot \text{mol}^{-1}$. Thus, the theoretical capacity equals to $372 \text{ mAh} \cdot \text{g}^{-1}$. For TiO_2 , the total number of electrons transferred is 1 ($n = 1$) and M is $79.87 \text{ g} \cdot \text{mol}^{-1}$. The calculated theoretical capacity according to Equation (1.4) is $336 \text{ mAh} \cdot \text{g}^{-1}$.

Among these anode materials, titanium dioxide nanotubes have been studied in my PhD research and the details will be discussed in the coming sections.

1.3. Titanium Dioxide Materials

Titanium dioxide (TiO_2) is an n-type semiconductor and a typical photocatalyst, attracting much attention from both fundamental and practical viewpoints.¹¹ In recent years, many low dimensional TiO_2 materials, such as nanowires, nanotubes, and nanorods have been successfully synthesized. Among them, TiO_2 nanotubes are particularly interesting, partly because of their large specific surface areas and their tubular structures,

which may supply a sufficient numbers of points for the reaction. Researchers increased attention on TiO_2 nanotubes due to their unique properties in energy storage application like batteries. Compared to graphite, TiO_2 nanotube has almost the same theoretical capacity ($\sim 336 \text{ mAh/g}$) based on Equation (1.4) as that of commercially used graphite ($\sim 372 \text{ mAh/g}$), but its volume expansion is only about 3%.¹² In addition, the operation voltage of graphite is 0.1 V (Li^+/Li redox couple), which may lead to the possibility of lithium plating during charge when exposed to the air.¹³ However, for TiO_2 nanotube, it is as high as 1.7 V (Li/Li^+ redox couple). The higher operation voltage not only bring safer battery operation, lower self-discharge and good capacity retention during cycling⁴ because of chemical stability and small volume expansion, but also works with several novel cathode materials (LiCoPO_4 ¹⁴ and $\text{LiCo}_{0.5}\text{Mn}_{1.5}\text{O}_4$ ¹⁵) to achieve Li-ion batteries with high voltage (5 V).

The morphological structures of TiO_2 nanotube can be divided into amorphous and crystalline.¹¹ The simulation structure of amorphous TiO_2 and corresponding TEM image are shown in Figure 1.4(a-b). In the simulation structure, one can notice that the atoms of Ti and O are randomly distributed in the structure and no unit cell exists.¹⁶ As an n-type semiconductor, the band gap of TiO_2 in amorphous state is 3.2-3.5 eV,¹⁷ illustrating the poor electronic performance. The amorphous TiO_2 is thermal stable in the room temperature and the structures will transform to crystalline with the temperature higher than 300°C .¹⁸ Because of the good mechanical properties of amorphous TiO_2 with high strength-to-weight, it can be applied in the biochemical field such as bone implant¹⁹ with the Young's Modulus of as high as 230 GPa.

Anatase is one of the crystalline forms of TiO_2 as shown in Figure 1.4(c-d). This is a tetragonal structure where every Ti octahedrally bonds to six O ions.²⁰ Unlike amorphous TiO_2 with many defects in the structure, the anatase has ordered structures, which can help electrons transportation in the structures. The results show that in anatase state, the band gap of TiO_2 is 3.2 eV,^{21, 22} which is smaller than in amorphous state. As previous discussed, the amorphous TiO_2 will transform to anatase when the temperature is higher than 300 °C, which means the anatase is more thermal stable than amorphous. In the range of 300-800 °C,¹⁸ the anatase will hold its whole or partial structures. When the temperature is higher than 800 °C, the rutile structures will form. The mechanical performance of anatase without many defects behaves a little better than amorphous.

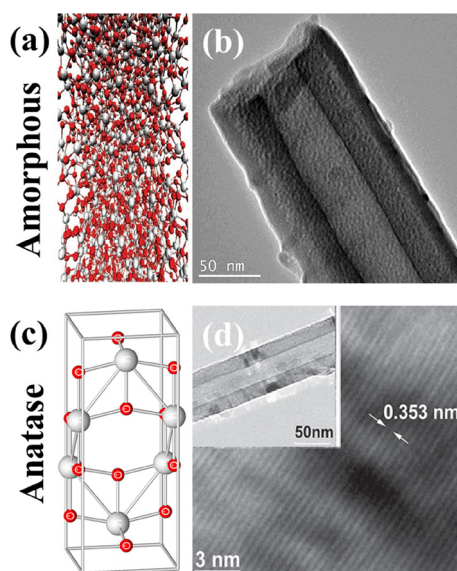


Figure 1.4 Amorphous structures of TiO_2 , (a) simulation structure,¹⁶ and (b) TEM image. Anatase structures of TiO_2 , (c) unit cell, and (d) HRTEM image showing the lattice structures. (Reprint with the permission from The Journal of Physical Chemistry C, 2011, 115, 15661-15673. Copyright, 2001, American Chemical Society)

1.4. Amorphous TiO₂ as anodes for Li-ion Batteries

Figure 1.5 depicts the phase diagram of Li-Ti-O. In the diagram, two stable phases can be found during lithium insertion, which are Li_{0.5}TiO₂ and LiTiO₂, respectively

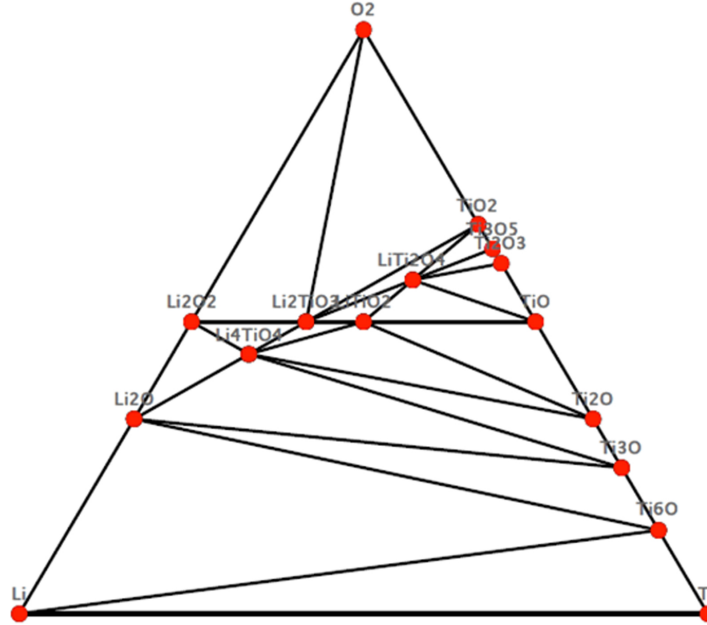
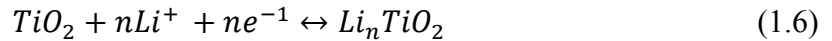


Figure 1.5 The phase diagram of Li-Ti-O obtained using MaterialsProject.com.

The insertion reaction of Li ions into both amorphous and crystalline TiO₂ nanotubes can be totally expressed as Equation (1.6):²³



In this redox reaction, the insertion of positively charged Li⁺ is balanced with an uptake of electrons to compensate for Ti³⁺ cations in the Ti⁴⁺ sublattice. The theoretical calculations have been predicted the relationship between Ti³⁺ and x .^{20, 24-29} The experimental results observed in X-ray photoelectron spectroscopy (XPS) have proved

the presence of Ti^{3+} states in Li_xTiO_2 . The x value determined from core level (Ti 2p) peak intensities is correlated to the amount of Li^+ .^{30, 31} The energy density of TiO_2 in mass and volume under the voltage of 1.8 V has been calculated in Equation (1.7) and (1.8), respectively.

$$\text{Energy density (mass)} = \frac{I \times V \times t}{m} \left(\frac{mA \times V \times h}{g} \right) = 336 \times 1.8 \left(\frac{Wh}{kg} \right) = 605 \left(\frac{Wh}{kg} \right) \quad (1.7)$$

$$\text{Energy density (volume)} = \frac{I \times V \times t}{v} \left(\frac{mA \times V \times h}{\frac{g}{\rho}} \right) = 336 \times 1.8 \times 4.23 \left(\frac{Wh}{l} \right) = 2558 \left(\frac{Wh}{kg} \right) \quad (1.8)$$

The behavior of charge and discharge curves for amorphous TiO_2 nanotube is shown in Figure 1.6. The charge-discharge cycles can be operated in a large range of potential ($\sim 1\text{-}3$ V), which is attributed to the considerable disordered structures and defects in amorphous TiO_2 . The various rate of charge-discharge showing in different color is presented in Figure 1.6(a). The discharge capacity is controlled by the rate and when increasing the rate, the capacity will decrease. Figure 1.6(b) depicts the cycling ability of amorphous TiO_2 in two different current densities of 10 and 30 A g^{-1} . The specific capacity decreases slightly after the first discharge due to the irreversible capacity loss in the first cycle and remains stable after hundreds of cycles. The coulomb efficiency after hundreds of cycles is also plotted in Figure 1.6(c), showing the good cycling performance of amorphous TiO_2 .³²

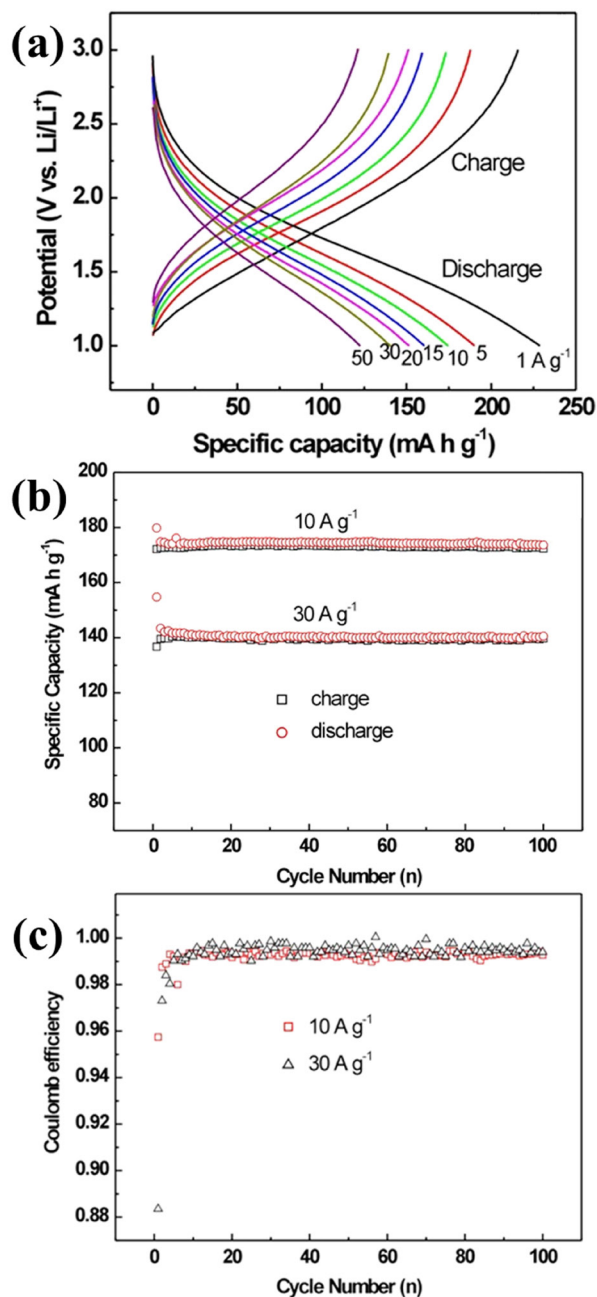


Figure 1.6 Charge and discharge curves for amorphous TiO_2 nanotube.³² (a) the charge-discharge curves in various rate, (b) cycling performance and (c) coulomb efficiency of amorphous TiO_2 at the current densities of 10 and 30 A g^{-1} . (Reprint with the permission from Nanotechnology, 2009, 20, 225701. Copyright, 2009, IOP Publishing)

1.5. The Order of Chapters in the PhD Dissertation

Chapter 2 describes the experimental method of growing TiO₂ nanotubes. There are many synthesis methods as mentioned in the introduction and each growing method has its unique features. In this research project, the TiO₂ nanotubes were synthesized by electrochemical method (anodization methods). The easiest set up and flexible environment are one of the advantages for anodization methods. Also, the as-grown nanotubes have uniform and aligned structures. In addition, an *in situ* transmission electron microscopy (TEM) holder equipped with scanning tunneling microscopy (STM) tip was introduced. The configuration of the holder and way of sample preparation were described in the chapter. This new technique helps to investigate structural evolution in real time.

Chapter 3 introduces a systematic study was conducted to correlate diameter and length of TiO₂ nanotubes to the anodization voltage and time. The nanotubes arrays were directly synthesized by anodization in ethylene glycol electrolyte containing NH₄F solution, which is less dangerous than conventional HF electrolyte. The current-voltage behavior of nanotubes during anodization was explained based on the nanotube growth theory. The physical properties of TiO₂ nanotubes were quantitatively measured and compared after 4, 8, and 16 hours anodization under 20, 40 and 60 V. This study found that the average diameter of the nanotubes remained unchanged with increasing anodizing time, but increased with voltage because of the stronger electrical field density related with higher voltage. The length of the nanotubes increased with higher anodization voltage and longer anodization time.

Chapter 4 investigates the structural instability of TiO₂ nanotubes subjected to treatment with ammonium hydroxide (NH₄OH) solution prior to calcination at elevated temperatures. The nanotubes were disintegrated into nanoparticles and the tubular morphology vanished after 2 hours of calcination at 500 °C. The nature of the structural collapse in the NH₄OH treated TiO₂ nanotubes was studied. It was found that the volumetric changes during the amorphous to anatase phase transformation and surface cracking were key during the collapse of NH₄OH-treated TiO₂ nanotubes.

Besides analyzing phase transformations of nanotubes in the traditional way, a new and fast way is created by in situ Joule heating in Chapter 5. A high-resolution transmission electron microscope (TEM) equipped with a scanning tunneling microscopy (STM) probe by Joule heating was used to induce phase transformation of anatase TiO₂ nanotubes into rutile nanoparticles. The phase transformation involved three processes. Under a bias heating of 10 V, the anatase TiO₂ nanotube broke into ultrafine anatase nanoparticles of average size between 5–10 nm. On further increasing the bias voltage to 20 V, the nanoclusters of anatase particles became prone to a solid state reaction and was grown into stable rutile nanoparticles of size ranging between 20–25 nm. The formation of rutile nanoparticles was confirmed by the observation of diffraction pattern and high resolution imaging of these particles, which corresponds to the tetragonal TiO₂ rutile phase.

In situ STEM system can also help to observe the materials structures changing in real time. In Chapter 6, the deformation driven modulation of the electrical transport properties of an individual anatase TiO₂ nanotube was studied. The current-voltage

characteristics of each individual anatase TiO_2 nanotube revealed that under bending deformation within the elastic limit, the electrical conductivity of a TiO_2 nanotube could be enhanced. High resolution TEM (HRTEM) and electron diffraction pattern revealed that TiO_2 nanotubes had tetragonal structure ($a=0.378$ nm, $c=0.9513$ nm, $I41/amd$). Analysis based on a metal-semiconductor-metal model suggested that in-shell, surface defect-driven conduction modes and the electron-phonon coupling effect were responsible for the modulated semiconducting behaviors.

Chapter 7 continues the study of deformation driven modulation by *in situ* STEM system to analyze the effect of mechanical deformation on the electrical transport properties of an amorphous TiO_2 nanotube. Under no mechanical straining, it was found that TiO_2 nanotubes behaved as electrical insulators. However, the nanotubes showed semiconducting behavior when they were in a highly deformed state. On the basis of a metal-semiconductor-metal model, it was suggested that in-shell defects, surface defect-driven conduction modes and the electron-phonon coupling effect were responsible for the appearance of semiconducting behaviors.

Chapter 8 discusses electrochemical behavior of TiO_2 nanotubes as anode materials in lithium ion batteries by *in situ* TEM. In this chapter, we report the first direct chemical and imaging evidence of lithium-induced atomic ordering in amorphous TiO_2 nanomaterials and propose new reaction mechanisms that contradict the general belief on the lithiation behavior of these materials. The lithiation process was conducted *in situ* inside an atomic resolution transmission electron microscopy. Our results indicate that the lithiation started with the valance reduction of Ti^{4+} to Ti^{3+} leading to a Li_xTiO_2

intercalation compound. The continued intercalation of Li ions in TiO₂ nanotubes triggered an amorphous to crystalline phase transformation. The crystals were formed as nano islands and identified to be Li₂Ti₂O₄ with cubic structure ($a = 8.375 \text{ \AA}$). The size of the crystalline islands provides a characteristic length scale ($\sim 5 \text{ nm}$) at which the atomic bonding configuration has been changed within a short time period. This phase transformation is associated with local inhomogeneities in Li distribution. Based on these observations, a new reaction mechanism is proposed to explain the first cycle lithiation behavior in amorphous TiO₂ nanotubes.

Chapter 2 Experimental Method

As mentioned in the introduction chapter, four major methods are listed for synthesizing TiO_2 nanotubes. In this research project, TiO_2 nanotubes were grown by anodization method, which was first invented by Gong.³³ The details about TiO_2 nanotubes synthesis procedure and in situ TEM sample preparation are discussed below.

2.1. TiO_2 Nanotube Synthesis

The TiO_2 nanotubes were grown by the anodization setup. Titanium foil (Sigma-Aldrich, 0.25 mm thick, 99.99%) was used as the substrate for growth of the oxide nanotube arrays. The foils were sonicated in the sequence of ethanol, deionized water, and acetone for 10 minutes each. Titanium foils served as the anodic electrode while platinum was used as the cathodic electrode. Electrolyte used in the experiment was 0.2 wt% NH_4F solution in a plastic beaker, which was prepared with NH_4F crystals, ethylene glycol, and deionized water with the ratio of 49:1 that helped dissolve the NH_4F crystals. Figure 2.1(a) shows the detailed setup.

Initially, Ti reacted with electrolyte to form a TiO_2 layer on the surface. The TiO_2 layer would react with NH_4F when F^- is the dominant ion in the system.³⁴ In this condition, the surface of the compact oxide layer was selected to dissolve in the electrolyte (known as etching). The etching rate varied at different areas of the oxide layer due to the differences in the magnitude of stress on the surface of oxide film. This selective etching produces porous structures on the surface.³⁴ The nanotubular structures

are formed through two processes: oxidation of titanium and oxide dissolution, which can be summarized as two reactions.³⁵⁻³⁷ The whole nanotubes growing process and reaction mechanism are shown in Figure 2.1(b).

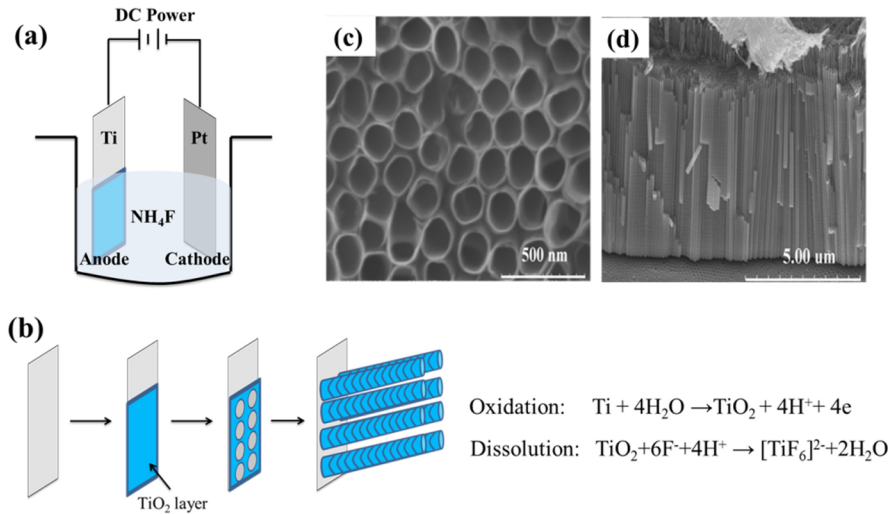


Figure 2.1 (a) Anodization setup. (b) Schematic of synthesis process of TiO_2 nanotubes. (c-d) FESEM images of surface and cross section views of TiO_2 nanotubes.

The anodization process was conducted at the voltage of 60 V for the processing time of 16 hours at room temperature. After completing the anodization experiments, the titanium foils were rinsed with deionized water and dried in the atmosphere. The TiO_2 nanotubes were characterized by FESEM and the surface and cross section images were shown in Figure 2.1(c-d).

2.2. *In Situ* TEM Setup

A new *in situ* holder is designed recently, which could help to conduct the experiment in real time comparing with the traditional holder. The configuration of *in situ* holder is shown as Figure 2.2(a).



Figure 2.2 (a) Configuration of *in situ* holder. (b) Experimental view of *in situ* holder in the TEM.

The *in situ* holder is separated into two parts, stationary and piezo-movable. A scanning tunneling microscopy (STM) tip can be equipped into the electronic device in the stationary stage, which can apply voltage or current into the system. The gold wire can be mounted in the hat sitting on the piezo-movable stage, which can help to move the gold wire in *X*, *Y*, and *Z* directions with a precision of 1 nm. The experimental view of *in situ* holder inside TEM is shown as Figure 2.2(b). The STM tip with sample is on the left top and the gold wire with Li_2O is on the right bottom.

The details of the TiO_2 nanotubes sample preparation are described in Figure 2.3. The nanotubes were scratched off from the substrate and then glued to STM tip with conductive epoxy glue. Lithium metal was scratched by a gold wire inside the glove box,

and transferred by a sealed container with Ar gas. Both W and Au were placed on the stationary and piezo-movable sides of an in-situ scanning tunneling microscope (STM) that operated inside a TEM, respectively. The naturally grown Li_2O layer on the surface of the Li metal served as the solid electrolyte for Li transport. The $\text{Li}_2\text{O}/\text{Li}$ electrode side was moved forward to contact one of the TiO_2 nanotubes. Once a good contact was built, a potential voltage ranging from -2 to -4 was applied to the TiO_2 nanotube to initiate the lithiation.

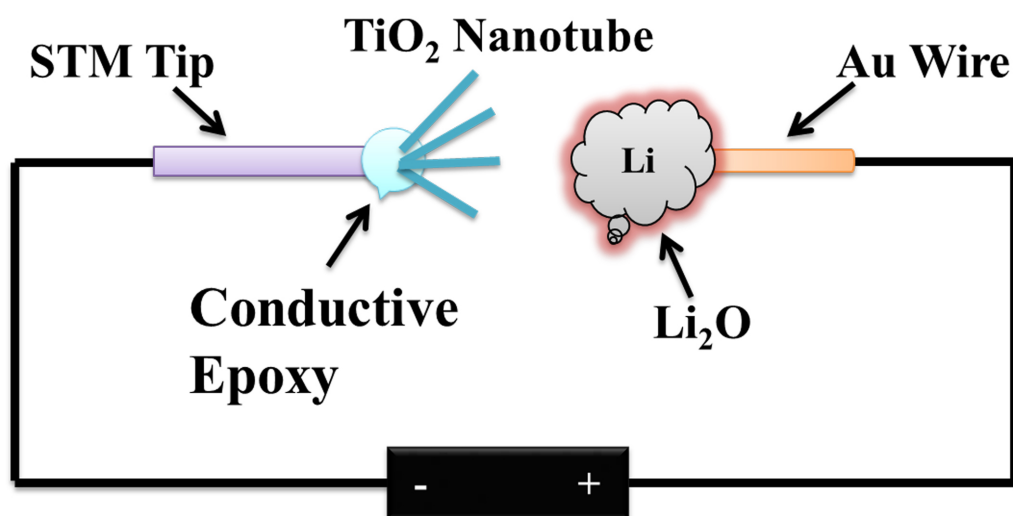


Figure 2.3 Schematic illustration of the in situ TEM setup for the lithiation/delithiation studies of amorphous TiO_2 nanotubes. The nanotubes are placed on the STM tip that is biased negatively with respect to the $\text{Li}/\text{Li}_2\text{O}$ counter electrode.

Chapter 3 Effect of Processing Parameters on the Physical Characteristics of Anodized TiO₂ Nanotubes¹

3.1. Introduction

In recent years, researchers increased work on titanium dioxides nanomaterials due to their unique properties in optics,³³ electronics,³⁸ and biology.³⁹⁻⁴³ Among various TiO₂-based nanomaterials (nanowires, nanotubes, and nanorods), TiO₂ nanotubular structures are particularly interesting because of their large specific surface areas and tube-like structures, which may supply much more reactive sites for the reaction. Gong *et al.* first produced titanium dioxide nanotubes arrays with the length up to 500 nm by electrochemical anodization in a HF aqueous electrolyte.³³ Over the past several years, the formation of titanium nanotubes arrays has been reproduced by many other methods including template synthesis,⁴⁴ layer-by-layer assembly strategy,⁴⁵ and hydrothermal processes.⁴⁶ Table 3.1 summarized the work of several research groups on the synthesis of nanotubes with different diameter and length.

¹The material contained in this chapter has been submitted to the *Materials Chemistry and Physics*. Copyright transfer agreement will become effective only after being accepted.

Table 3.1 TiO₂ Nanotubes Synthesized by Various Methods

Synthesis Methods	Diameter	Length	Preparation Materials	Reference
Anodization	65 nm	250 nm	Either HF, NaF, KF, or NH ₄ F with DMSO ^a , EG ^b , FA ^c , NMF ^d , or glycerol	33
	110 nm	4.4 μ m		47-49
	150 nm	134 μ m		50
	20-280 nm	0.2-7.4 μ m		51, 52
Hydrothermal	9-10 nm	122 nm	Precursor material with TiO ₂	11, 53
	20 nm	1 μ m	in NaOH solution	54
Sol-gel	100 nm	7 μ m	Anodic alumina template	55
	120 nm	1.5 μ m	membrane with pores dip into TiO ₂ sol	56
Layer by Layer Assembly	215 nm	60 μ m	Prepare TiO ₂ and TiO ₂ based compound using Layer by Layer strategy	45

a. Dimethyl Sulfoxide; b. Ethylene Glycol; c. Formamide. d. N-Methylformamide

Based on Table 3.1, different fabrication methods can produce TiO₂ nanotubes arrays with a broad range of diameters and lengths. Even for the same method, different synthesis conditions lead to different diameters and lengths. Among the four methods, anodization is the most popular, due to its simple operation and easy control of diameters and lengths. Many anodization factors can affect the morphology of the TiO₂ nanotubes,

such as electrolyte composition, temperature,^{57, 58} water concentration,⁵¹ anodization voltage and time, formamide,⁵⁰ ethylene glycol,³⁶ polyethylene glycol,⁵⁹ DMSO⁶⁰ and glycerol^{51, 52} containing fluoride ions have been studied as the anodization electrolyte. Due to their different viscosities, the TiO₂ nanotubes show different lengths and diameters. For NH₄F-glycerol system, the relation between the tube morphology and various anodization parameters, including the fluoride and water concentration, anodization voltage and time, have been systematically studied.⁵¹ Generally, the diameter and length of TiO₂ nanotubes increase with elevated anodization voltage. NH₄F-ethylene is another important electrolyte system. Comparing to other electrolyte candidates, especially HF, NH₄F is much safer. For NH₄F-ethylene glycol electrolyte, the effects of water concentration and acidity have been studied.⁶¹ As far as we know, there is no systematic study of quantify the effects of anodization voltage and time for NH₄F-ethylene glycol system. In practical applications, the morphology of TiO₂ nanotubes is a vital factor in determining the device performance, such as in areas of solar cell,^{11, 34, 62-69} batteries,^{70, 71} and biomedical implants.⁷²⁻⁷⁶ So, it is necessary to systematically study the NH₄F-ethylene glycol system, which is possibly as reference for a controlling the morphology of anodized TiO₂ nanotubes. In this work, a systematic study was conducted to quantitatively measure the geometrical properties of TiO₂ nanotubes to correlate them with the anodization voltage and time.

3.2. Experimental Procedure

Titanium foil (Sigma-Aldrich, 0.25 mm thick, 99.5%) was used as the substrate for growth of the TiO₂ nanotubes arrays. Prior to anodization, all the foils were sonicated in

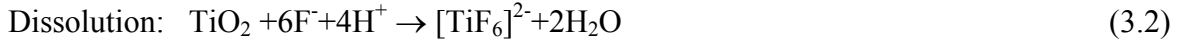
ethanol, deionized water, and acetone, each for 10 minutes. After drying, the back side and edges of the samples were wrapped with Teflon. For each foil, 1 cm x 1 cm area was left for anodization. The anodization system was composed of two-electrode electrochemical cell. Titanium foil served as the anodic electrode while platinum mesh was used as the cathodic electrode. Electrolyte used in the experiment contained 0.2 wt% NH_4F , ethylene glycol and deionized water with the volume ratio of 49:1. Voltage was applied by a DC - Power and the current was measured by a Keithley[®] 2100 Digital Multimeter. The anodization process was performed under the voltages of 20, 40 and 60 V. The anodization times were 4, 8 and 16 hours at room temperature. After the anodization experiments, the titanium foils were rinsed with deionized water and dried in the atmosphere for further characterization. The surface structures were observed by Hitachi S-4700 scanning electron microscopy (SEM) under the operating voltage of 10 kV. An in-house image analysis software was developed in Matlab software to characterize the distribution of diameters and lengths in nanotubes.

3.3. Result and Discussion

3.3.1. Mechanism of TiO_2 Nanotubes Formation

The formation mechanism of TiO_2 nanotubes has been extensively studied.³⁴⁻³⁷ Initially, titanium reacts with electrolyte to form a TiO_2 layer on the surface. The TiO_2 layer reacts with NH_4F when F^- is the dominant ion in the system.³⁴ In this case, the compact oxide begins to be etched and dissolved in some areas. The etching rate varies at different areas of the oxide layer due to the differences in the magnitude of stress on the surface of oxide film. This selective etching produces porous structures on the surface.³⁴

The formation of nanotube structure includes two processes: oxidation of titanium and TiO₂ dissolution, which can be summarized as two reactions as follows.³⁵⁻³⁷



Inside a pore, there are two interfaces: solution/oxide and oxide/metal. The oxidation of titanium (Reaction 3.1) happens on the metal/oxide interface at the pore bottom during the transport of the oxygen-containing ions [Figure 3.1(a)]. At the same time, the TiO₂ layer would dissolve in the electrolyte, indicating Ti⁴⁺ migrate from metal to the solution/oxide interface [Figure 3.1(b)], shown as Reaction 3.2. The electrical field can enhance the migration of the metal ions, which is called field-enhanced dissolution. The increase of the pore size gives the electrolyte a chance to penetrate into the oxide/metal interface to form the second oxide layer with the following etching by the electrical field. Thereafter, the morphology of TiO₂ exhibit layer by layer structures on the surface. With the increase of electrical field intensity at the pore bottom, when is much higher than that at the wall, Ti starts to be consumed at a high rate near the bottom of the pore, allowing continuous increasing the pore depth. During the increase of the pore depth, the tube starts to shrink because of the surface tension and internal surface area increasing. When the neighbored pores were close enough, the surface tension induced on the oxide layer would pull apart the pores, eventually resulting in the pore separation and the tube formation [Figure 3.1(c)]. In current work, bamboo-type TiO₂ nanotubes were found as shown in Figure 3.1(d), which support the layer by layer growth

mechanism of TiO_2 nanotubes. The formation of bamboo-type morphology is related with the fluctuation of anodization current, which is caused by the diffusion and breakdown of TiO_2 layer at nanotubes bottoms.^{52, 77}

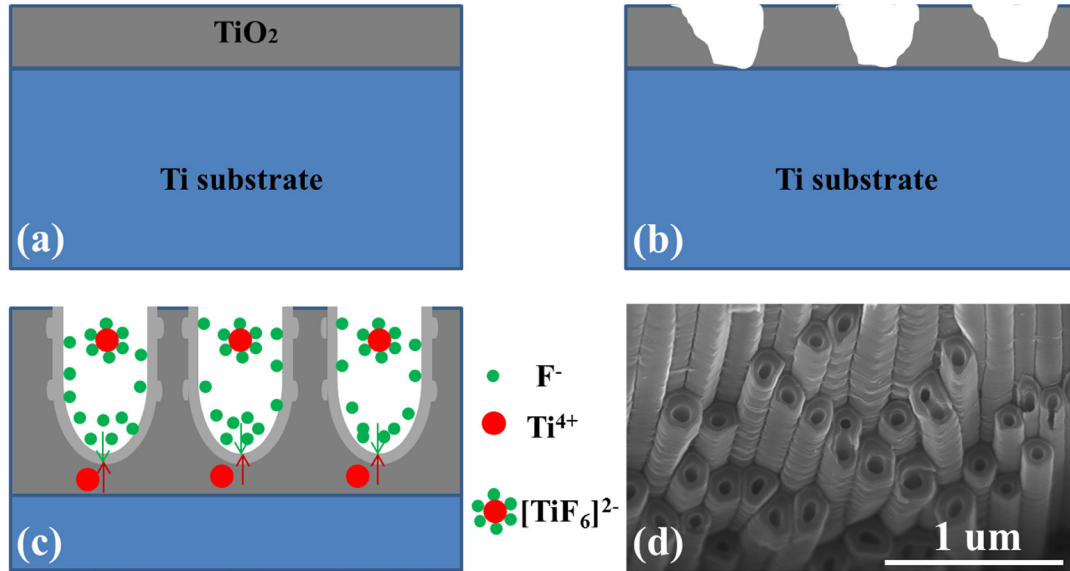


Figure 3.1 Schematic diagram of TiO_2 nanotubes formation: (a) formation of oxide layer, (b) pore growth due to dissolution reaction, (c) nanotubes formation layer by layer, and (d) SEM image of bamboo-type nanotubes.

3.3.2. Anodization Current-Voltage Behavior

Figure 3.2 shows the changes in current density as a function of time at three different anodization voltages: 20, 40, and 60 V. When the voltage was applied to the system, the current increased quickly due to the metallic nature of titanium foil. That initial drastic current was followed by a drop because of the formation of compact titanium dioxide layer on the surface, which increased the resistance. The pores started to form due to the dissolution of the titanium dioxide in solutions containing fluoride ions.

The current densities stopped decreasing until a stable and ordered pore growth had been established.

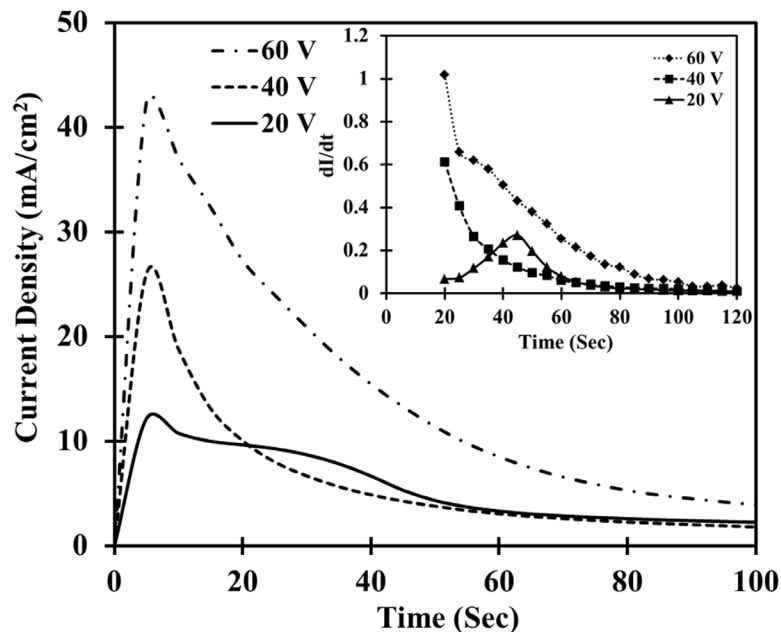


Figure 3.2 Current density (J-t) curves at three different anodization voltages.

As shown in Figure 3.2, the maximum current increases with increased voltage. Due to the same electrolyte and electrodes, the total resistance of the system remains the same in all three cases. It is expected that the higher voltage caused higher maximum current and faster oxidation reaction (Reaction 3.1). The inset in Figure 3.2 shows the current drop rate curves. The current drop rate (dI/dt) at 40 and 60 V is much higher in comparison to that at 20 V. This is related with faster growth of oxide layer in 40 and 60 V, which increase the electrical resistance of the system. In the case of 20 V, the oxide layer may have not completely covered the surface at about 20 second. That is why the peak starts to increase and then decrease between 20 and 60 seconds in the 20 V case.

3.3.3. The Effect of Anodization Time on the Diameter of Nanotubes

Figure 3.3(a-d) shows the SEM images and the corresponding diameter analysis results for samples after 4, 8, and 16 hours anodization under 40 V. As shown in Figure 3.3(d), the average diameter of nanotubes after 4 hours anodization was 66 nm. As the time increased to 8 and 16 hours, the average diameters increased to 67 and 74 nm, respectively. Even though the time increases considerably, the diameter only increases by about 10% and the difference is statistically insignificant. This relatively small increase on diameter with longer anodization time can be explained by the mechanism of TiO₂ nanotubes formation. Under applied voltage, the electric-field-assisted anodization of titanium occurs at the metal/oxide interface. After that, the dissolution process occurs. The diameter forms at the beginning stage of dissolution process, where the reaction rate is quite fast. Therefore, we believe that the anodization time will not substantially affect the diameter of nanotubes.

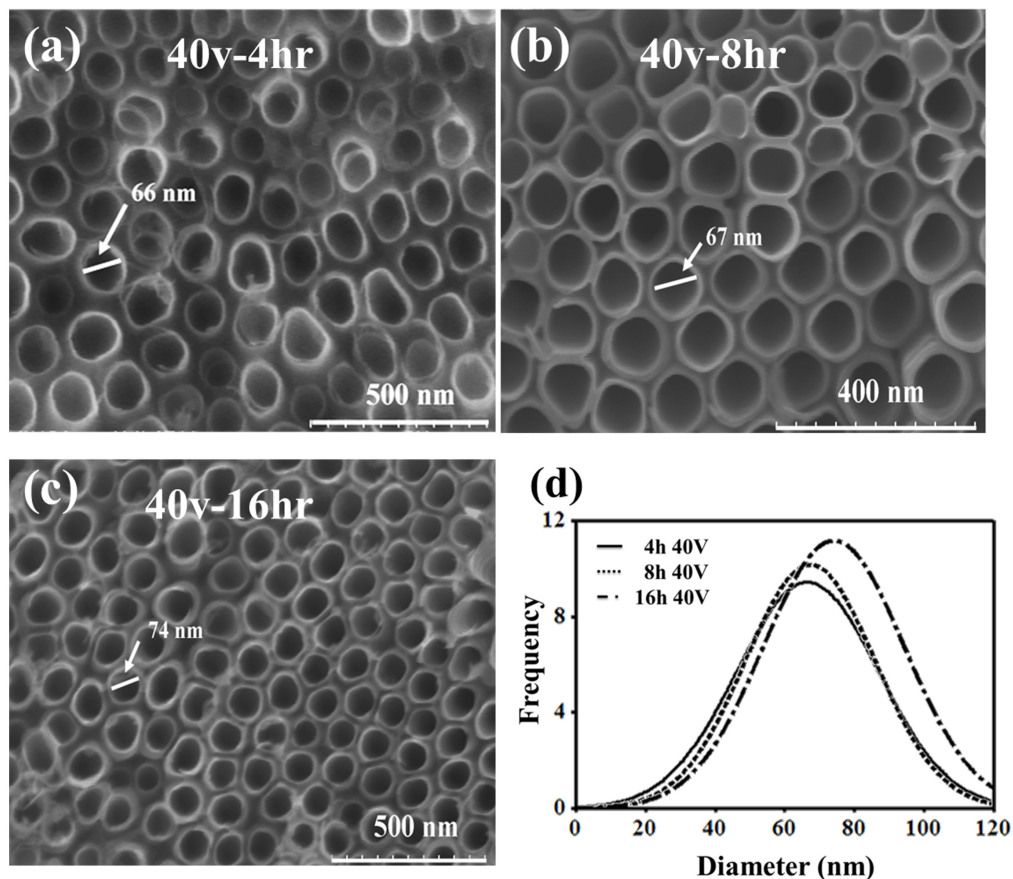


Figure 3.3 FE-SEM images of the free end of the nanotubular structure obtained under 40 V after different anodization time (a) 4, (b) 8, and (c) 16 hrs. (d) The plot for diameter distribution of nanotubes. The average diameter was calculated to be 66, 67 and 74 nm for 4, 8 and 16 hours, respectively.

3.3.4. The Effect of Anodization Voltage on the Diameter of Nanotubes

Figure 3.4 shows the diameter of nanotubes under two different voltages of 20 and 60 V after 16 hours anodization. The distribution plot in Figure 3.4(c) provides a comparison between the diameters of the nanotubes under different anodization voltages. When the voltage increases from 20 [Figure 3.4(a)] to 40 V [Figure 3.3(c)], the average

diameter of the nanotubes increases from 54 to 74 nm. With further increase to 60 V [Figure 3.4(b)], the diameter of nanotubes increase to 144 nm, which is almost the double of the diameter under 40 V. The anodization voltage is the main factor affecting the etching speed. Higher voltage supplied higher current and produced stronger electrical intensity. This directly accelerated the migration of metal ions. Therefore, more titanium metals were involved in the dissolution process, resulting in formation of TiO_2 nanotubes with large diameter.

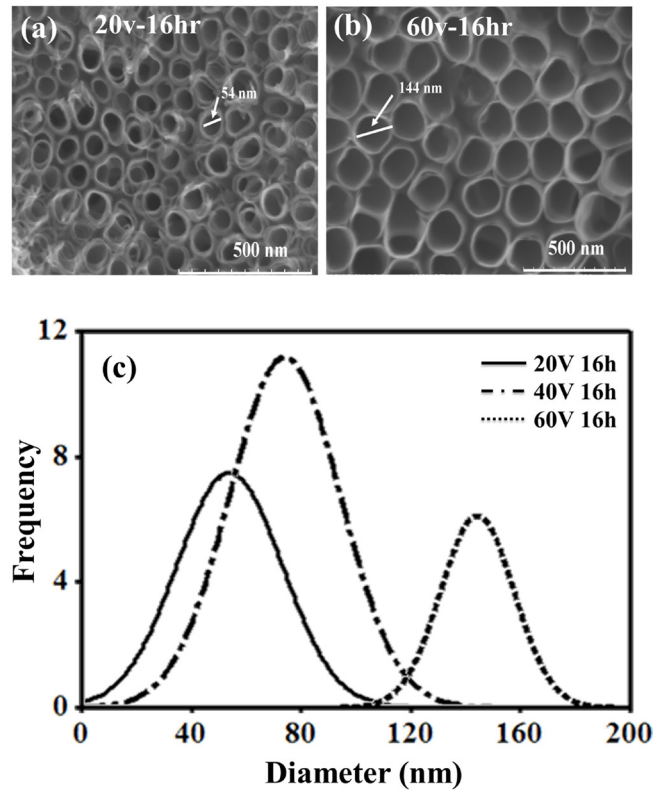


Figure 3.4 FE-SEM images of the tubular structures obtained after 16 hours anodization under different voltage: (a) 20 V, and (b) 60 V. (c) The plot for diameter distribution of nanotubes. The average diameter was 54, 74 and 144 nm for 20, 40 and 60 V, respectively.

Generally, the diameter of TiO₂ nanotube is proportional to the applied voltage and can be described as $d=k \times V$, where k is the growth coefficient.⁷⁸ In current work, the growth coefficient is about 2.3. In the glycerol-NH₄F system, the growth coefficient is about 6 where the electrolyte is composed of 0.27M NH₄F with 1:1 ratio of glycerol-NH₄F.⁵¹ The main differences are the concentration of F⁻ and electrolyte viscosity. It has been found that the concentration of F⁻ does not affect the diameter of TiO₂ nanotubes.⁵¹ The different growth coefficient is mainly caused by the different viscosity. The viscosity of 50% glycerol-50% H₂O and ethylene glycol is about 0.004 and 0.022 Pa•s, respectively.⁵⁸ The relatively higher viscosity of ethylene glycol limits the migration of ions and increases the electrical resistance of the anodization system, which reduces the diameter of the TiO₂ nanotubes.

Figure 3.5 summarizes the effect of anodization voltage and time on the diameter of nanotubes. Overall, the anodization voltage is more effective to change the diameters of TiO₂ nanotubes than that of anodization time. Under constant voltage, the diameter only increases slightly with longer time. On the other hand, under constant anodization time, the diameter increases substantially when the anodization voltage increases.

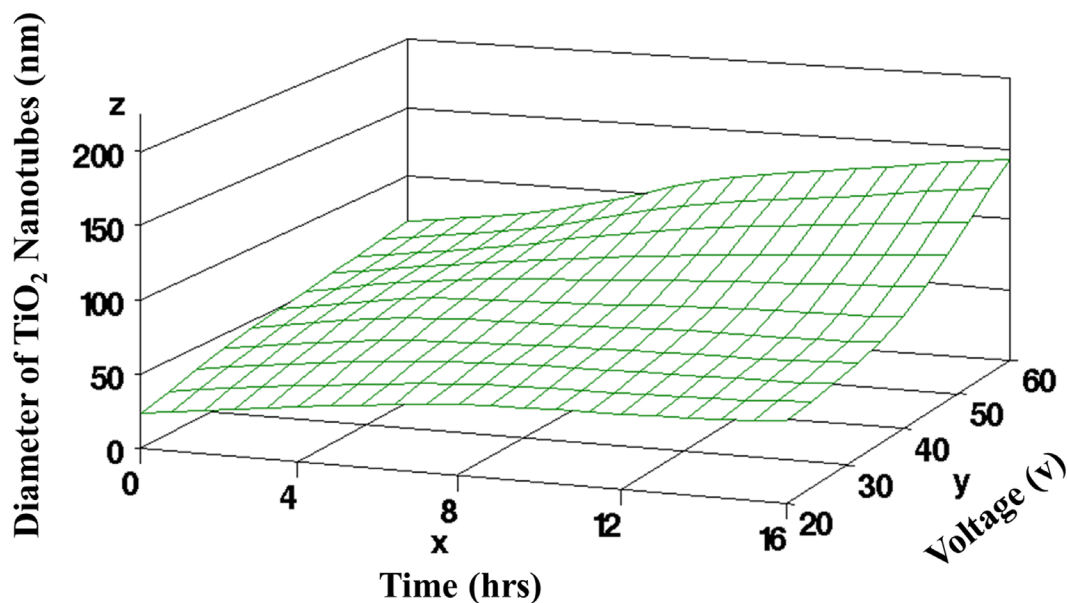


Figure 3.5 The change in diameter of TiO₂ nanotubes arrays as a function of anodization time and voltage.

3.3.5. The Effect of Anodization Time on the Length of Nanotubes

Figure 3.6 shows the SEM images after 4, 8, and 16 hours anodization under 60 V. From the cross section view in Figure 3.6(a), most of the nanotubes bundled together. Some nanotubes were broken and twisted due to the interaction forces among the nanotubes. The average length of nanotubes is 5493 nm after 4 hours anodization. When the anodization time increased from 4 to 8 hours, the length of nanotubes increased from 5493 to 6754 nm, as shown in Figure 3.6(b). With further increase to 16 hours, the length of nanotubes can increase up to 10000 nm. The chemical dissolution of oxide with time may have caused the relatively less length increase from 8 hours sample to 16 hours samples. The titanium substrate was consumed at a high rate near the bottom of the pore and supplied the continuous growth of the pore depth, which represented the length of

nanotubes. Based on the J-t curves (Figure 3.2), the reaction rate stayed in equilibrium for a long time that gave the growth process at an almost constant rate. Therefore, increasing anodization time can produce longer TiO_2 nanotubes.

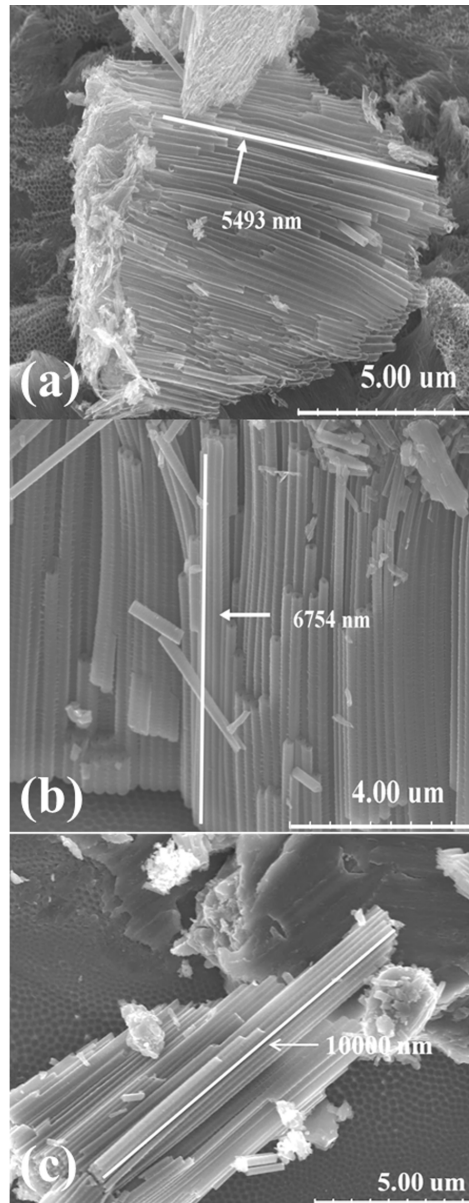


Figure 3.6 The tubular structures under 60 V after various anodization time (a) 4, (b) 8, and (c) 16 hours, respectively.

3.3.6. The Effect of Anodization Voltage on the Length of Nanotubes

Figure 3.7 shows the SEM images after 16 hours under 20 and 40 V. It is obvious that the length of nanotubes increased with elevated voltage. The length of nanotubes in Figure 3.7(a) is about 1388 nm after 16 hours anodization. The lengths of nanotubes under 40 and 60 V were 6114 nm [Figure 3.7(b)] and 10000 nm [Figure 3.6(c)], respectively. Higher voltage will produce stronger electrical field. A stronger electrical field can dissolve more titanium and allow continuous growth of the pore depth, resulting in longer nanotubes formation. Similarly, the relatively less increased should be contributed by more dissolution of oxide at higher voltage. The glycerol-NH₄F system found the similar phenomena with increased voltage.

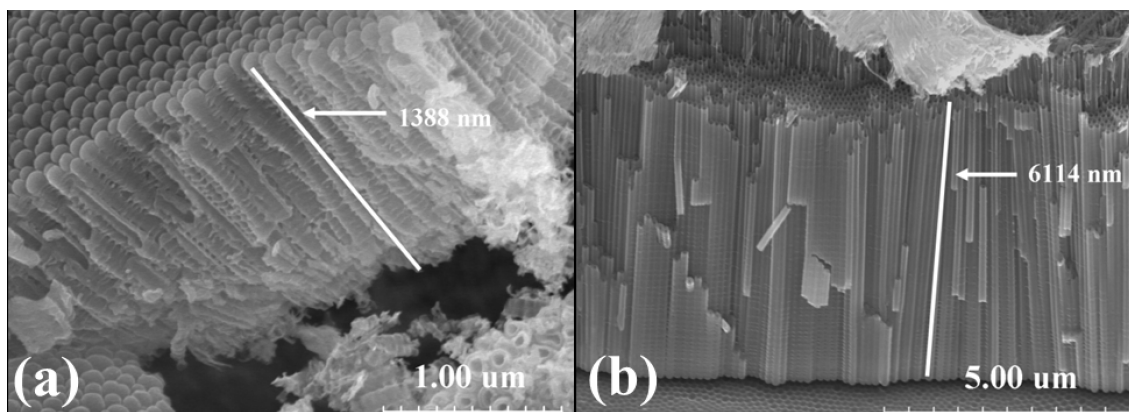


Figure 3.7 The tubular structures after 16 hours anodization under different voltage: (a) 20, and (b) 40 V, respectively.

Figure 3.8 summarizes the effect of anodization time and voltage on the length of nanotubes. Generally, both long anodization time and high voltage can increase the length of the nanotubes. But at voltage less than 20 V, even longer anodization time will not increase the length significantly due to the low etching process. When voltage was

increased to 20 V or higher, the increase of anodization time significantly increased the length of nanotubes.

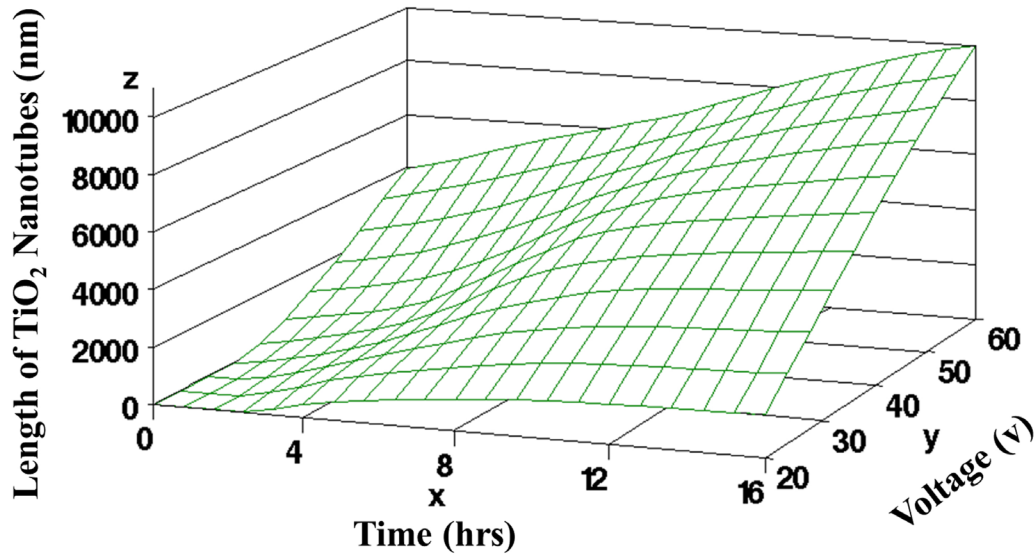


Figure 3.8 The change in length of TiO₂ nanotubes arrays as a function of anodization time and voltage.

In current work, the correlation between morphologies of TiO₂ nanotubes (diameter and length) and anodization parameters (voltage and time) were systematically investigated. It has been proved that the morphologies of TiO₂ nanotubes are critical for various practical applications. The results in the work can provide guidance for size control of TiO₂ nanotubes growth. Different size of TiO₂ nanotubes plays a key role in the charge/discharge performance in Li ion batteries. Furthermore, the Na battery system requires the diameter of TiO₂ nanotube is at least larger than 80 nm. Another advantage is that, the synthesized TiO₂ nanotubes in current work are smooth and avoid the formation of nanograss.

3.4. Conclusion

The present work investigates the change of diameter and length of TiO_2 nanotubes with different anodization time and voltage in ethylene glycol electrolyte containing NH_4F solution, which is less dangerous than conventional HF electrolyte. The current-voltage behavior of nanotubes during anodization was explained based on the nanotube growth theory. In addition, the geometrical properties of nanotubes were quantitatively measured and compared as a function of anodization voltage and time. It was found that the anodization time would not substantially affect the diameter of nanotubes. The diameter of nanotubes is mainly controlled by the applied voltage. Both the voltage and anodization time have a significant influence on the length of the TiO_2 nanotubes.

Chapter 4 Structural Instabilities in TiO₂ Nanotubes²

4.1. Introduction

Titanium dioxide (TiO₂) is a semiconductor with excellent photocatalytical properties,^{79, 80} and the recent reports on fabrication of TiO₂ nanotube layers^{33, 81-83} have opened new perspectives for solar cell applications. The method to prepare such tubes, based on anodization of Ti foils in diluted HF-containing electrolytes, has been reported in recent years.^{81, 82} To date, TiO₂ nanotube arrays of up to 1 mm length have been achieved using ethylene glycol electrolytes.⁵⁰ The electrolyte composition and *pH*, as well as anodization voltage, are important factors in determining the resulting nanotube length. Pore formation in TiO₂ nanotubes is controlled through competition between metal oxidation and oxide dissolution, with these variables in turn determined by anodization parameters including electrolyte properties.^{51, 84, 85} The resulting TiO₂ structures are composed of arrays of nanotubes with common diameter of about 100 nm and the largest known value of 350 nm.⁸⁶

²The material contained in this chapter was previously published in the *Journal of Applied Physics* (Reprinted with permission from T. Shokuhfar, Q. Gao, A. Ashtana, K. Walzack, P. Heiden, C. Friedrich, *Journal of Applied Physics*. 108, 104310 (2010). Copyright 2010, American Institute of Physics.)

Recently, Wang and Lin⁸⁷ were able to fabricate a self-organized, freestanding titania (TiO₂) membrane with ultrahigh aspect ratio of the length/diameter (1500) via electrochemical anodization of highly pure titanium (Ti) foil in fluorine containing ethylene glycol. Later on, they showed that in aqueous electrolyte, the anodization potential exerted significant influence on the formation of TiO₂ nanotube arrays, while the effect from the electrolyte temperature is little.⁸⁸ As a consequence, TiO₂ nanotube arrays with tube diameters ranging from 20 to 90 nm and film thicknesses ranging from several hundred nanometers to several micrometers were obtained.

The drawback is the high band gap energy (3.2 eV) of TiO₂, which means that it can be excited only by UV light (380 nm).⁸⁹ Over the last decades, essentially two approaches were intensively investigated in order to make the material more responsive to the natural solar spectrum. One approach is to sensitize TiO₂ with a suitable dye to construct an efficient solar cell.^{90, 91} The other approach to obtain a good photocatalytic performance is doping with impurities, e.g., transition metals or other elements, including C, N, F, P, Ru, and S. It was found that substitutional N-doping is the most promising path toward photocatalytical applications.⁹²⁻⁹⁵ It has been suggested that nitrogen ions substitute oxygen atoms in the TiO₂ lattice and thus the corresponding N 2*p* states are located above the valence band edge. Mixing of N 2*p* states with O 2*p* states results in a reduction in the band gap of the N-doped TiO₂ and as a result, higher photoelectrochemical efficiencies can be achieved under vis light irradiation.⁹⁶ The common approach to N-doped TiO₂ is its sputtering in a gas mixture of N₂ with Ar,⁹² annealing in pure ammonia gas,⁹⁴ dc magnetron sputtering of TiO₂ electrodes in Ar/O₂ /N₂ mixture,⁹³ or, alternatively, by

immersing the as-anodized TiO₂ nanotubes in nitrogen enriched media and then calcinations at high temperatures.⁹⁷

Before utilization of the titania nanotubes for different applications, factors like the crystalline nature of the structure and stability of the desired crystalline phases must be examined. The first work on disintegrating anodic TiO₂ nanotubes into single crystalline TiO₂ nanoplates was reported.⁹⁸ Their results show that high temperature annealed TiO₂ nanotube arrays could be transformed into nanoplates by strong mechanical forces, e.g., milling or simply grinding. Here, we report the structural instability of TiO₂ nanotubes exposed to concentrated aqueous ammonia solution. High-resolution transmission electron microscopy (TEM), Raman spectroscopy, x-ray diffraction (XRD), and atomic force microscopy (AFM) were used to understand the nature of structural collapse in the NH₄OH treated TiO₂ nanotubes.

4.2. Experimental Procedure

4.2.1. Synthesis

Titanium foil (Alfa Aesar, 0.25 mm thick, 99.95%) was used as the substrate for growth of the oxide nanotube arrays. All the reagents were used as provided, and the solutions were all prepared with deionized water obtained using a Milli-Q Reagent Water System (Millipore, Bedford, MA, USA). Prior to the anodization, the titanium foils were chemically polished in 1% HF aqueous solution for 2 min, rinsed with deionized water, and dried in nitrogen. The pretreated titanium foil was anodized by using platinum foil as cathode in an electrolyte containing dimethyl sulfoxide (DMSO) and hydrofluoric acid

(HF, 48% aqueous solution). The anodization voltage, HF concentration in DMSO, and duration of anodization were in the range of 60 V, 2 wt %, and 40 h, respectively. Platinum foil was used as the counter electrode. After being anodized, specimens were rinsed with distilled water immediately and dried. The as-anodized foils were then immersed in concentrated aqueous ammonium hydroxide (NH₄OH) solution for 30 min, and then calcinated at 500 °C in atmosphere for 15–120 min. The nontreated titania nanotubes were also annealed at the same condition for comparison purposes.

4.2.2. Characterization

The surface morphologies and length of the doped TiO₂ nanotube array were observed by a field emission scanning electron microscopy (SEM), and the crystallinity of the samples was investigated by XRD technique using a Scintag XDS2000 Powder diffractometer. Raman spectra were collected at room temperature with a Raman spectrometer (Jobin-Yvon HR800 Raman Spectrometer) operating with NeCd laser of 442 nm with the resolution system of $\sim 0.1 \text{ cm}^{-1}$. The crystallinity studies and elemental analysis of the titania nanotubes separated from the titanium support were performed using a JEOL-4000 FX TEM operated at 200 keV.

4.3. Results

Figures 4.1(a) and 4.1(b) show the top-view SEM morphologies of the TiO₂ nanotube arrays prepared by anodizing of titanium. The TiO₂ nanotube arrays are tubes with diameter of 60–90 nm and a wall thickness of about 20 nm. Most of the pore mouths

of nanotube are open on the top of the layer. It can be seen that the nanotube arrays are uniform over the substrate.

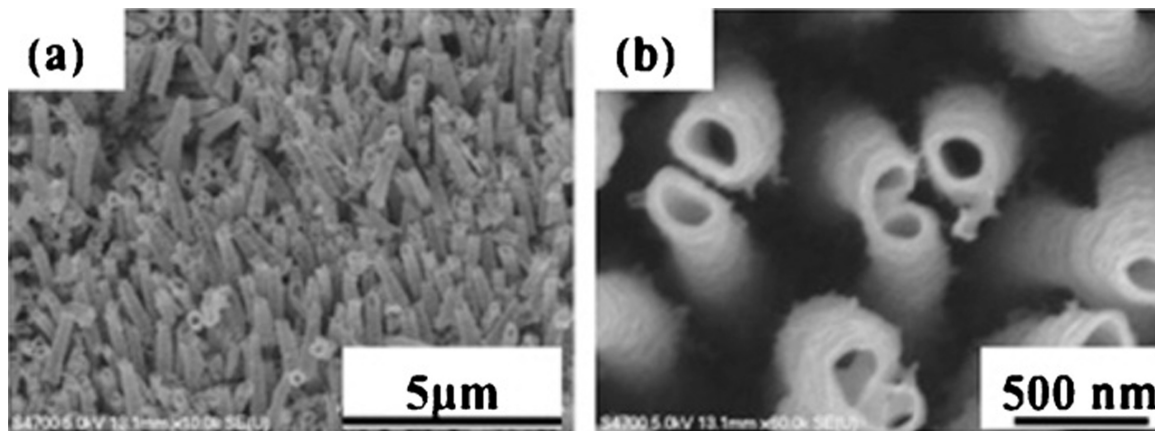


Figure 4.1 The SEM images of (a) as-synthesized TiO_2 nanotubes arrays and (b) close of nanotubes shown in (a).

To reveal the morphological structure of as-synthesized TiO_2 nanotubes, the samples were investigated by TEM. Figure 4.2 shows a bright field and corresponding diffraction pattern for the nanotubes. The tubular structure with variation in wall thickness throughout the length of the tube (marked by arrows) is evident from the figure. As one can see, the diffraction pattern [Figure 4.2(b)] shows diffuse peaks resembling the amorphous structures for the samples. A close examination of samples using high resolution imaging [Figure 4.2(c)] did not reveal any sign of distinct atomic order confirming the amorphous morphology of the as-synthesized tubes.

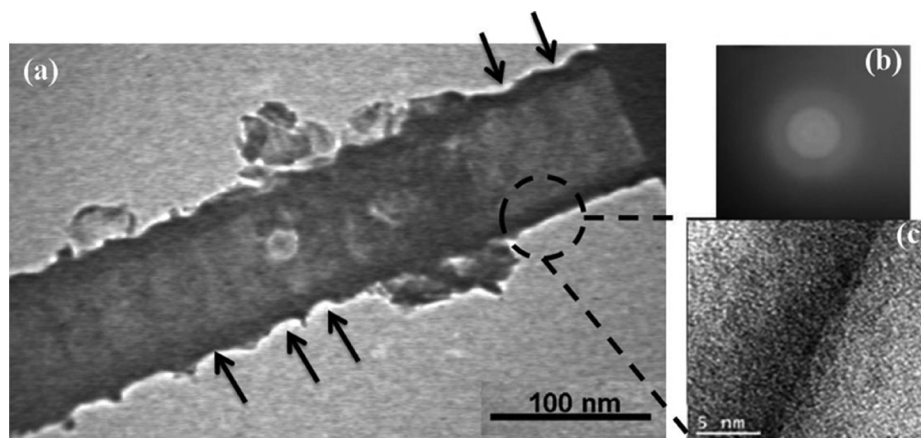


Figure 4.2 The bright field (a), diffraction pattern (b), and high resolution TEM (c) images of as-synthesized TiO₂ nanotubes.

In the next step, the samples were immersed in ammonium hydroxide solution for 30 min. After 30 min the nanotubes were let to dry in air prior to SEM imaging. Figures 4.3(a) and 4.3(b) show that the NH₄OH-treated nanotubes maintain their tubular morphology. The SEM analysis of end-on nanotubes did not reveal any changes in the tubes' diameter or length in comparison to the tubes shown in Figure 4.1.

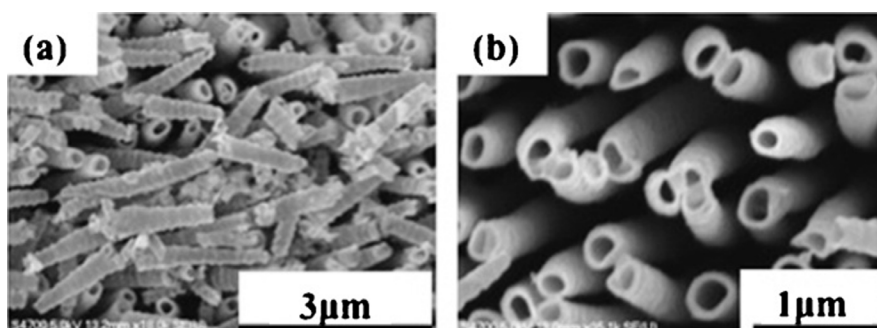


Figure 4.3 [(a) and (b)] The SEM images of TiO₂ nanotubes treated by NH₄OH for 30 min.

Both the as-synthesized and NH_4OH -treated TiO_2 nanotubes were heated to 500 °C, which is the temperature that anatase should become thermodynamically stable.¹⁸ Figure 4.4 shows SEM, bright field TEM images, and corresponding diffraction pattern of the as-synthesized nanotubes after calcinations at 500°C. As Figure 4.4(a) shows the annealing of as synthesized nanotubes did not alter apparent morphology of the tubes [compare Figure 4.4(a) and 4.1(a)]. However, the TEM diffraction pattern [Figure 4.4(c)] and high resolution imaging of the tube walls [Figure 4.4(d)] confirm the transformation of amorphous structure to anatase phase by calcination at 500 °C.

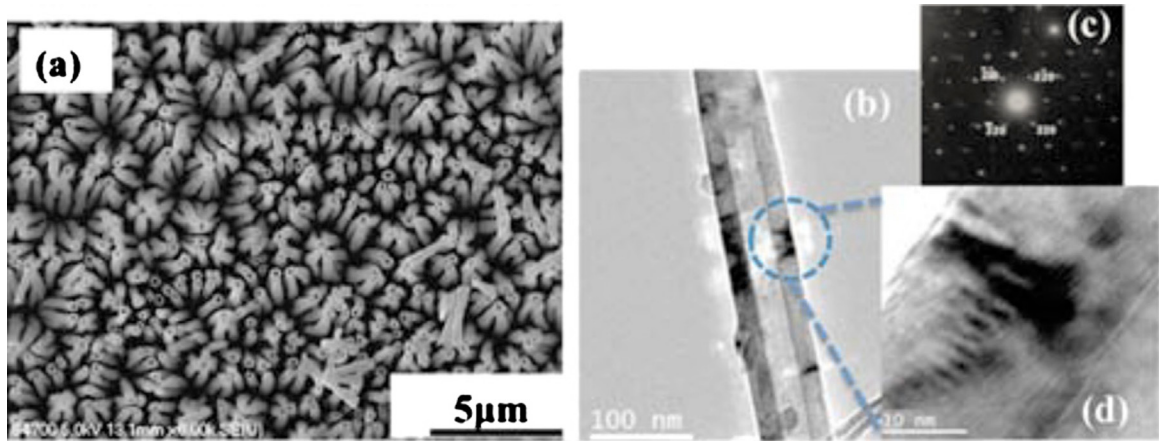


Figure 4.4 (Color online) The SEM images show (a) as-synthesized TiO_2 nanotubes after annealing in 500 °C. [(b) and (c)] The bright field TEM image and diffraction pattern of nanotubes shown in (a) indicate the transformation of amorphous morphology to crystalline order in the nanotubes. (d) The high resolution TEM image confirms the crystalline order of anatase phase and the presence of structural defects (appear as dark contrasts).

Interestingly, the structural studies of NH_4OH -treated TiO_2 nanotubes annealed at 500°C revealed an unexpected morphological transformation. Figure 4.5 shows the SEM images of the NH_4OH -treated nanotubes. While the nontreated nanotubes maintain the same structural morphology [compare Figure 4.3(a) and 4.1(a)], the NH_4OH -treated sample showed no sign of nanotube architects. Surprisingly, the nanotubes were being replaced with nanoparticles of 20–30 nm size

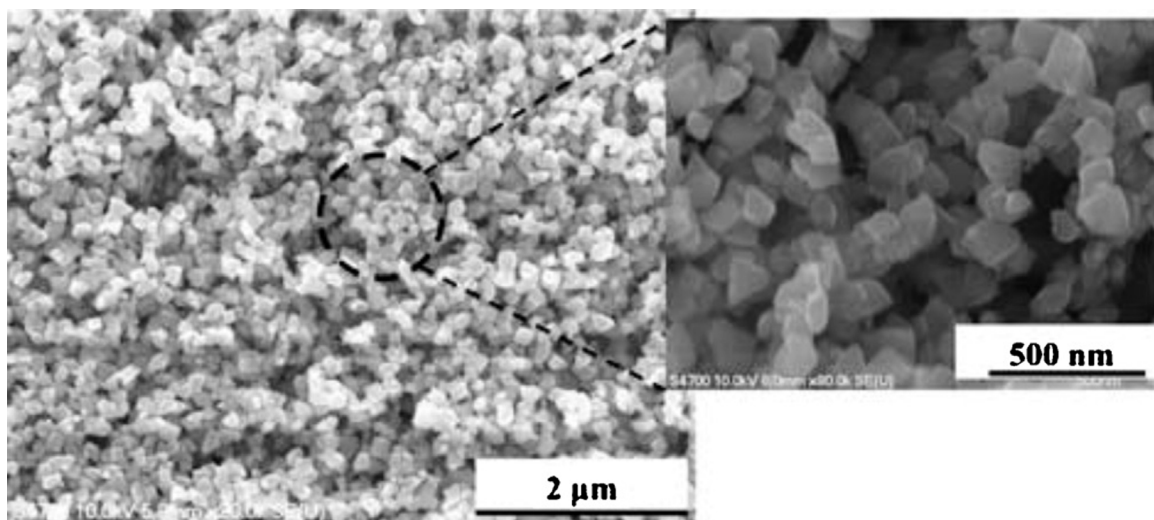


Figure 4.5 The SEM images show the morphology of the NH_3 -treated TiO_2 nanotubes after calcination at 500°C for 2 h. The treated nanotubes collapsed into nanoparticles upon heat treatment at anatase phase transformation temperature.

To study the evolution of such structural transformation, a series of calcination treatments at various time steps were carried out. Figure 4.6 shows the SEM images of NH_4OH -treated TiO_2 nanotubes after 0, 10, and 30 min of calcination at 500°C . As one can note, the morphology of NH_4OH nanotubes is relatively unchanged. However after

10 min the nanotubes start to disintegrate into small particles and this behavior is more severe after 30 min where the nanotubes are barely maintain their tubular morphology.

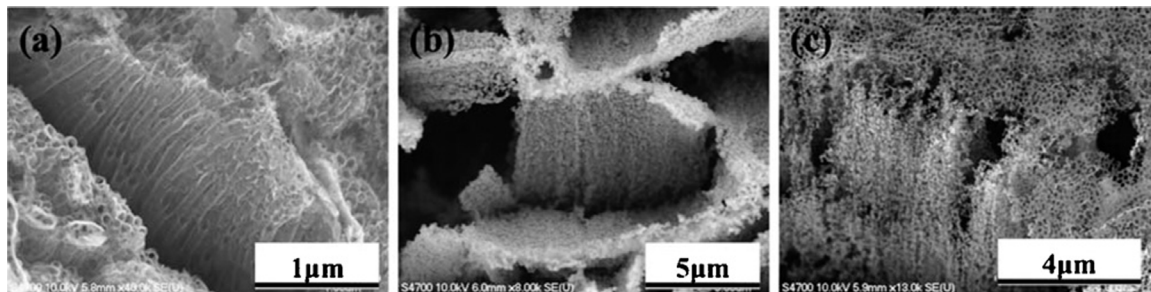


Figure 4.6 The SEM images of NH_4OH -treated TiO_2 nanotubes after 0(a), 10(b), and 30 (c) minutes of calcination at 500°C . The treated nanotubes start to disintegrate into small particles.

This unexpected structural change in the NH_4OH -treated TiO_2 nanotubes motivated us to further study the role of ammonium hydroxided titanium dioxide nanotubes by XRD, Raman, and TEM. Figure 4.7 shows the XRD patterns for the untreated TiO_2 and NH_3 -treated TiO_2 nanotubes [designated as (N)] after annealing at 300 and 500°C temperatures. For samples annealed at 300 and 500°C for 2 h, the highest intensity diffraction peaks appeared at 25.43° and 48.10° , in well accordance with the (101) and (200) peaks of anatase titania. This indicates the formation of crystalline anatase phase, whereas no evidence of the existence of rutile phase is observed. In 500°C sample, two weak peaks at 41.5° and 53.5° (marked by * symbol) appeared corresponding to Ti foil (the substrate). The NH_3 -treated titania nanotubes 300°C (N) and 500°C (N) show no obvious difference with the untreated nanotubes with respect to the diffraction peak

positions of anatase phase, indicating the amount of nitrogen incorporated is too little to affect the crystal lattice.

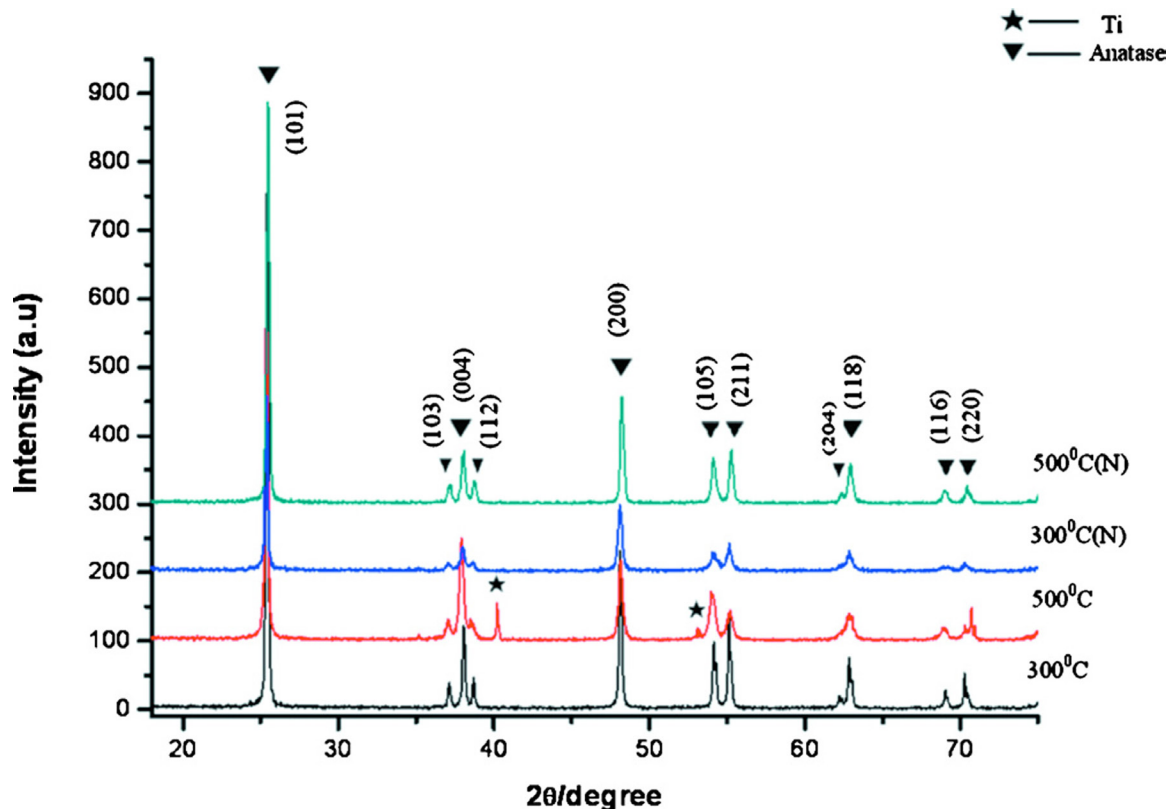


Figure 4.7 (Color online) The XRD patterns of untreated and ammonium hydroxide [designated by (N)] TiO₂ nanotubes.

Figure 4.8 shows the Raman spectra of titania nanotubes with and without NH₃ treatments after the annealing at 500 °C. The baseline with no peaks corresponds to the TiO₂ foil. In both nontreated and NH₄OH-treated cases, the nanotubes show the typical peaks at 400 cm⁻¹, 515 cm⁻¹, and 640 cm⁻¹ were all identified as B_{1g}(A), A_{1g}/B_{1g}(A), and E_g(A) vibration modes of anatase phase,^{99, 100} respectively. From the spectra of NH₃-treated nanotubes, we hardly can find the vibromold of titanium nitride, maybe this is

because the incorporation of nitrogen is very little and did not introduce obvious changes in crystal lattice, in accordance with XRD analysis.

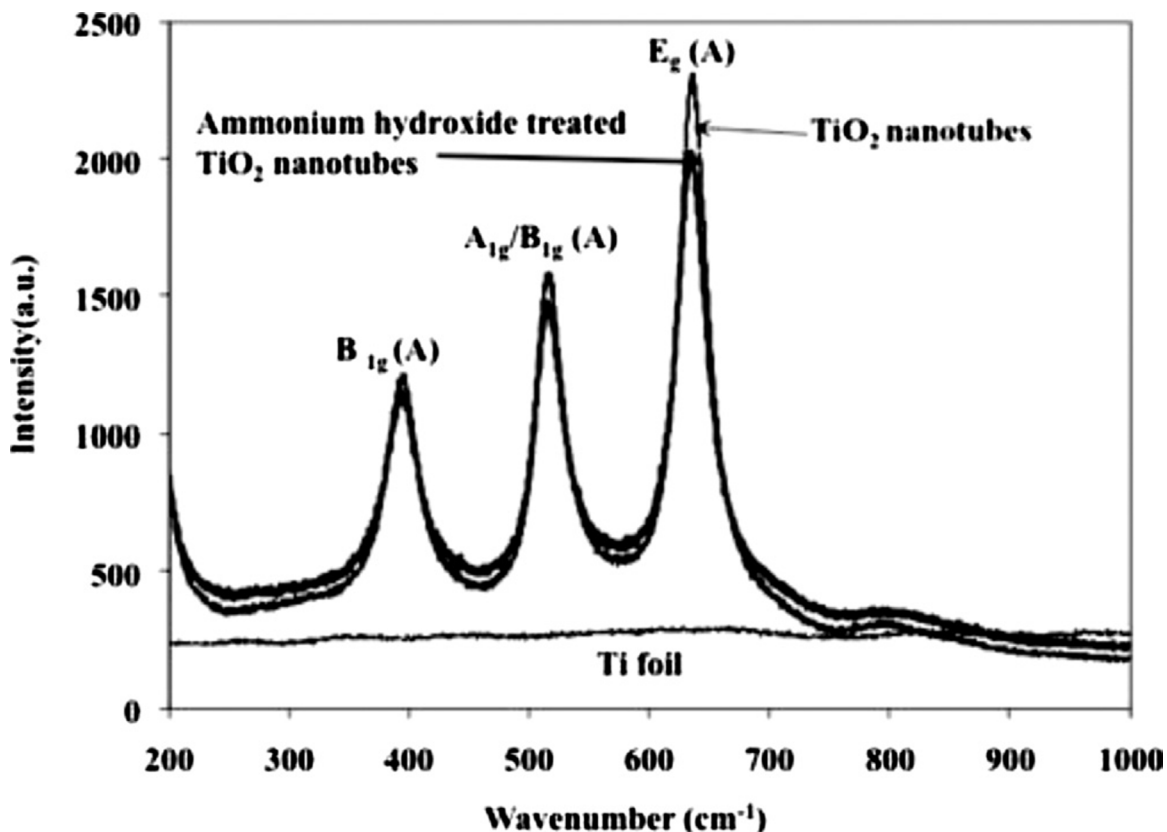


Figure 4.8 The Raman spectroscopy of the Ti foil, untreated and ammonium hydroxide-treated TiO₂ nanotubes. The A in parenthesis stands for anatase.

The high resolution TEM and diffraction analysis of the NH₄OH-treated and annealed samples revealed a structural order similar to anatase phase. The bright field image shown in Figure 4.9 indicates the presence of structural defects in the nanoparticles. In addition, the diffraction analysis confirms that the dominant phase is anatase by the presence of (101) and (103) planes in the diffraction pattern (inset in Figure 4.9). The confirmation of anatase phase is quite interesting because the initial evidence based on

the particle morphology suggests that the particles could be rutile phase. Sreekantan *et al.*¹⁰¹ reported the disintegration of the nanotube arrays into rutile particles after calcinations above 600 °C. Li *et al.*¹⁰² also reported similar phenomenon in TiO₂ nanotubes. Dong *et al.*⁹⁷ concluded that nitrogen doping could facilitate the anatase-rutile phase transition at the annealing temperature of 500 °C. In general, it is believed that rutile phase cannot be stable in nanotubular morphology of TiO₂ due to fact that the minimum nuclei size of rutile is usually larger than the wall thickness of nanotubes.¹⁸ Therefore, overall conclusion was that the formation of rutile phase is associated with the disintegration of nanotubes.

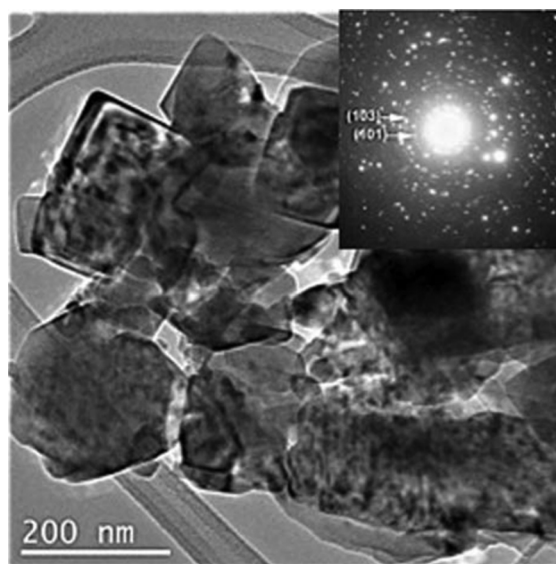


Figure 4.9 Bright field TEM images of nanoparticles after the collapse of TiO₂ nanotubes by NH₃-treatment and annealing at 500 °C. The inset shows the diffraction pattern of particles and indicates that the crystal structure is anatase.

4.4. Discussion

During the process of amorphous to anatase transformation in annealing the as-anodized nanotubes, the length and average diameter of the nanotubes had no discernible changes. It has been suggested that the initial crystallization of anatase took place both in the nanotubes and in the nanotube–foil interface at almost the same temperature.¹⁰³ In this process, some of the closely spaced anatase crystallites coalesced to form larger crystallites.

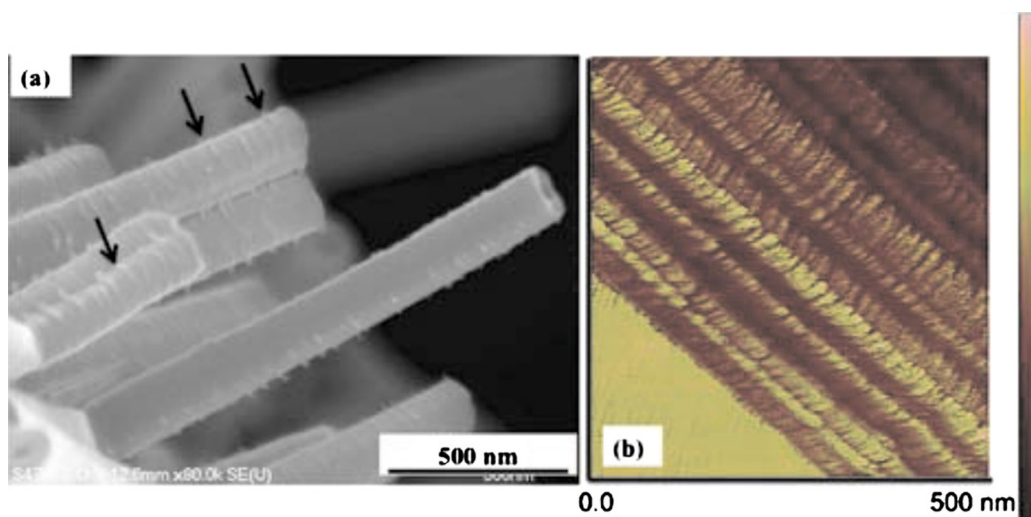


Figure 4.10 (Color online) (a) The as-synthesized TiO₂ nanotubes show imperfections on the surface (marked by the arrows). (b) The elastic modulus map of TiO₂ nanotubes before immersion in the ammonia hydroxyl media is shown. The dark brownish color indicates areas of high stiffness and areas of bright yellowish correspond to low stiffness values. The scanned area is 500 nm and the color key represents qualitative comparison of the modulus.

We found that it was difficult to incorporate nitrogen in the TiO_2 lattice by a simple NH_4OH treatment of TiO_2 nanotubes. From the XRD spectra we hardly could find the vibromold of titanium nitride, and concluded that this was because the incorporation of nitrogen was very little and did not introduce obvious changes in crystal lattice. In addition, since the atomic radius of nitrogen is a little bigger than that of oxygen, the nitrogen doping should have led to compressive stress and eventually the broadening of vibrating modes. Such effect had been observed in phosphorus doped titania.¹⁰⁴ A possible effect of NH_4OH treatment of TiO_2 nanotubes is the incorporation of nitrogen in surface roughnesses and weakening of the nanotubes.¹⁰⁵⁻¹⁰⁷ The nanotubes are in fact “nanopits” that are formed on Ti foils and therefore should inherit the grain boundaries and defects already exist in the foils. In addition, the nanotubes shown in Figure 4.1(a) and 4.10(a) exhibit surface roughness, which can be potential areas of chemical etching. The evidence of such weak boundaries is shown in Figure 4.10, which maps the stiffness of nanotubes. The peak force tapping© (PFT) mode of an AFM system was used to image the relative stiffness variation along the length of nanotubes. In PFT mode, the cantilever taps the surface and makes very small deformation indents (less than 2 nm). The maximum force required to achieve this was recorded and used to calculate the stiffness based on the unloading curves. The presence of high and low stiffness areas along the length of nanotubes indicates that these areas could potentially be the sites of misorientation regimes divided by grain boundaries.

Based on the above observations, we propose the following model (Figure 4.11) for the structural instabilities in NH_4OH -treated TiO_2 nanotubes. The treatment of nanotube

in NH_4OH solution and subsequent calcination at 500°C results in structural transformation to anatase nanoparticles and the associated volumetric change results in high stress concentrations at the surface roughness areas. The nanotubes barely maintain their tubular morphology after 30 min of calcination. After this, the nanotubes will be collapsed into nanoparticles while the transformation to anatase happens simultaneously.

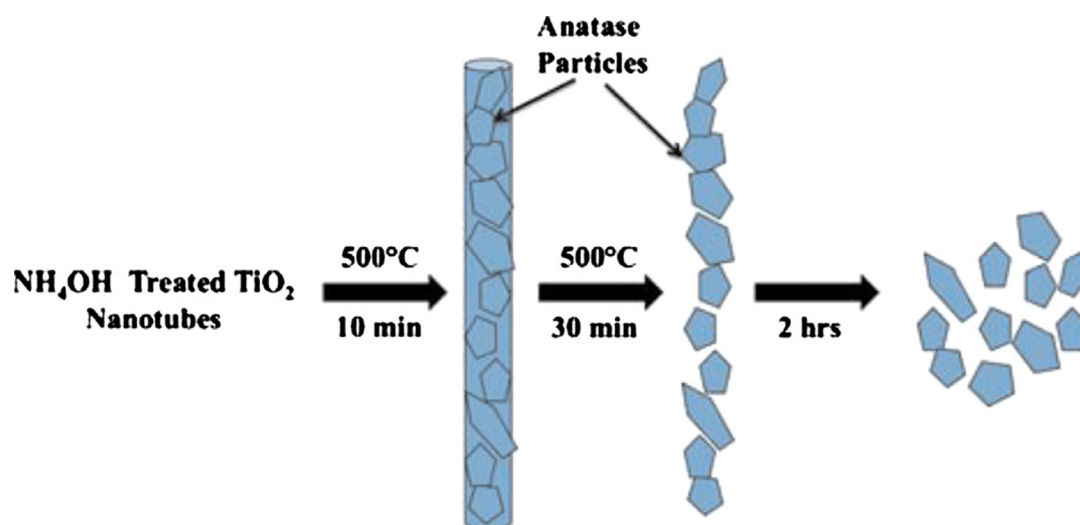


Figure 4.11 (Color online) A schematic of the observed structural instability in TiO_2 nanotubes treated with NH_4OH and calcinated at 500°C . The surface roughness is shown in the larger scale than the nanotube dimension. The nanotube disintegrated into anatase particles after 10 and 30 min of calcination but maintained the overall configuration of nanotube. After 2 h the nanotubes collapsed into nanoparticles.

4.5. Conclusions

TiO_2 nanotubes subjected to treatment with ammonium hydroxide (NH_4OH) solution followed by calcination at 500°C exhibited an unexpected structural instability

by collapsing into nanoparticles. High-resolution TEM, Raman spectroscopy, XRD, and AFM were used to understand the nature of structural collapse in the NH_4OH treated TiO_2 nanotubes. As opposed to the common belief that the transformation to rutile is the major reason for the collapse of the anatase nanotubes, it was determined that volumetric change due to phase transformation (amorphous \rightarrow anatase) and surface roughness weakening due to chemical etching had the key role during the collapse of NH_4OH -treated TiO_2 nanotubes.

Chapter 5 A Real Time Observation of Phase Transition of Anatase TiO₂ Nanotubes into Rutile Nanoparticles by In-Situ Joule Heating Inside Transmission Electron Microscope³

5.1. Introduction

Titania (TiO₂) has been widely studied because of its many useful optical, electrical and photocatalytic properties, which depend on the crystalline structure of TiO₂.¹⁰⁸⁻¹¹¹ Technological applications have been proposed for TiO₂ in bulk and thin film forms. The TiO₂ properties depend on phase composition, microstructure, crystallinity and chemical composition, which can be modified by preparation techniques, thermal treatments and metal ion doping.¹⁰⁸⁻¹¹⁵ Titania crystallizes into three natural phases: brookite (orthorhombic), anatase (tetragonal) and rutile (tetragonal).^{116, 117} The brookite and anatase crystalline phases, which are stable at low temperatures, transform into rutile when the sample is calcined at high temperature.¹¹⁸ It has been demonstrated that some properties of TiO₂ are very sensitive to its structure. Since the anatase phase is chemically

³The material contained in this chapter was previously published in the *Advanced Science Letters*. (Reprinted with permission from Anjana Asthana, Tolou Shokuhfar, Qi Gao, Patricia A. Heiden, Craig Friedrich, Reza S. Yassar. *Advanced Science Letters*, 3, 557 (2010). Copyright 2010, American Scientific Publishers)

and optically active, it is suitable for catalysts and supports.^{119, 120} Usually, the anatase phase can be transformed into rutile via post-annealing^{62, 121} because anatase is thermodynamically unstable. This anatase-to-rutile phase transition, which is dependent upon annealing temperature, induces the variation of the optical properties in TiO₂ films.¹²²⁻¹²⁴ Therefore the post-annealing should be a controlled process in order to make desirable properties of a TiO₂ film for various applications. We have taken a new approach to synthesize rutile nanoparticles. Here, we report the phase transition of an anatase TiO₂ nanotube into nanometer size rutile particles via *in situ* Joule heating inside a high resolution transmission electron microscope (HRTEM).

5.2. Experimental Procedure

The *in situ* Joule heating experiment was conducted in a high resolution transmission electron microscope (TEM, JEM 4000FX, operated at 200 kV) using a special scanning tunneling microscopy (STM)–TEM holder system from “Nanofactory Instruments.” The STM–TEM system provides a unique combination of transmission electron microscopy and scanning tunneling microscopy techniques, which are used simultaneously in one instrument for full sample characterization. It consists of a STM equipped TEM sample holder, a controller and a PC with Nanofactory’s data acquisition software. All the measurements were carried out on a single tilt STM–TEM holder in a JEM 4000FX TEM, operated at 200 kV. The setup of the STM–TEM holder is shown in Figure 5.1. The electrochemically etched gold wire with TiO₂ nanotubes was attached to the piezo-driven movable part of the holder facing the fixed and sharp tungsten STM tip as its counter electrode, and oriented perpendicular to the electron beam in the TEM. In

such an arrangement, atomic scale imaging and I - V measurements were carried out concurrently. The contact was made between the STM tip and the TiO₂ nanotube by the precision movement of the gold wire (with the sample) attached to the piezo-driven manipulator. Joule heating was conducted by applying different bias voltages to the gold electrode with the nanotube sample at its tip, while the tungsten STM tip was grounded. In the present investigations, TiO₂ nanotube samples were synthesized by anodization of TiO₂ foils for 8 hours at 60 V. The synthesis process is almost similar to that of reported by Schmuki et al. and Djenizian *et al.*^{125, 126} The anodization bath used is the solution of NH₄F (Ammonia Flouride) + Ethylene glycol + small amount of DI (deionized water). The electrochemical set up consists of a DC supplier and two electrodes. The anodic electrode is TiO₂ nanotube and the cathodic electrode is Pt mesh.

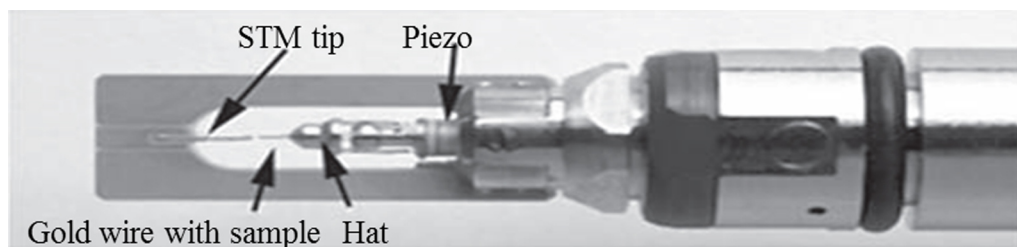


Figure 5.1 The image showing the experimental setup for STM-TEM holder.

5.3. Results Discussion

The structural investigations of TiO₂ nanotube samples were carried out during the *in situ* TEM experiment. Figure 5.2(a) is a low magnification bright field image of the as-synthesized (by anodization) TiO₂ nanotube. The general morphology shows that the as-synthesized TiO₂ nanotubes are hollow and closed ended. The nanotubes have average outer and inner diameters of 100 nm and 50 nm, and the wall thickness of the tubes is not

uniform. The corresponding diffraction pattern [inset in Figure 5.2(a)] and the high resolution transmission electron microscopy (HRTEM) image [Figure 5.2(b)] clearly show that the tubular structures are amorphous. The as-synthesized TiO_2 nanotube is transformed into the crystalline anatase phase via annealing it at 450°C for 3 h. Figure 5.3(a) shows an overall view of the anatase titania nanotube, depicting a number of tubular nanostructures with uniform size distribution. The tubes are hollow and open ended with an average inner and outer diameter of approximately 25 nm and 70 nm, respectively and the lengths range from several-tens to several-hundreds of nanometers. The corresponding diffraction pattern is shown in the inset [Figure 5.3(a)], depicting the anatase titania ($a=0.378$ nm, $c=0.9513$ nm, $I4_1/amd$). The HRTEM image [Figure 5.3(b)] taken from a single nanotube [inset of Figure 5.3(b)] shows that the nanotubes are well crystalline. The lattice fringe spacing of the walls of the nanotubes is estimated to be ~ 0.353 nm, corresponding to the interplanar distance of the (101) plane in the anatase phase.

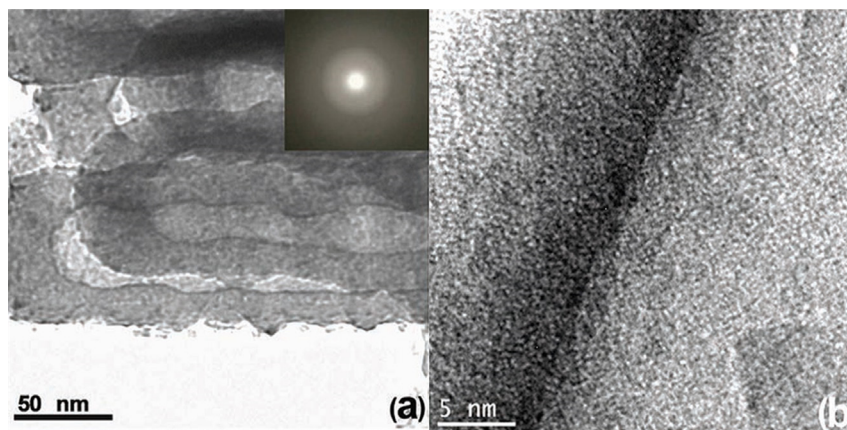


Figure 5.2 (a) TEM bright field (BF) image of the as-synthesized TiO₂ nanotubes and its corresponding electron diffraction pattern (inset) and (b) the high resolution image.

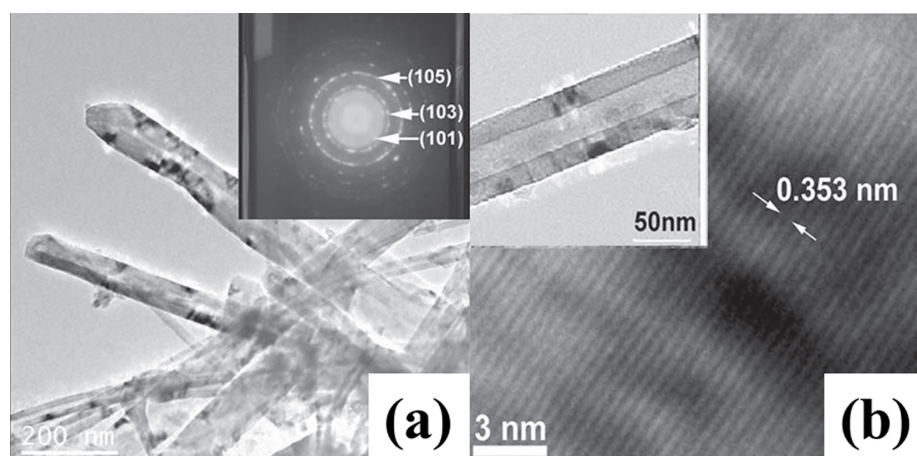


Figure 5.3 (a) An overall view of the anatase titania nanotube and the corresponding diffraction pattern (inset) and (b) the high resolution lattice image from a single anatase nanotube (inset).

To have good electrical contact between the sample and tungsten tip, for *in situ* electrical measurements, an individual TiO₂ nanotube was attached to an electromechanically etched gold tip by tungsten deposition using the focused ion beam

(FIB) technique. The different steps of the sample preparation are shown in Figures 5.4(a–c), in which a single nanotube is picked up by the FIB microprobe and attached to the tip of the tungsten wire. The gold tip with the attached TiO₂ nanotube was then loaded into the specimen holder and moved to the opposite conducting STM tip by a piezomanipulator. A schematic diagram of the experimental setup is shown in Figure 5.4(d). The Joule heating experiment was conducted by applying constant bias voltage, when the TiO₂ nanotube was in contact with the STM tip. Figure 5.5(a) shows a TiO₂ nanotube contacted on both ends and free standing in high vacuum (10^{–6} Torr), inside the TEM. Under 10 V bias, the current, I , starts to increase gradually with time, t , and reaches a maximum value of 12 μ A in a period of 180 sec, as shown by the I versus t plot (Figure 5.6).

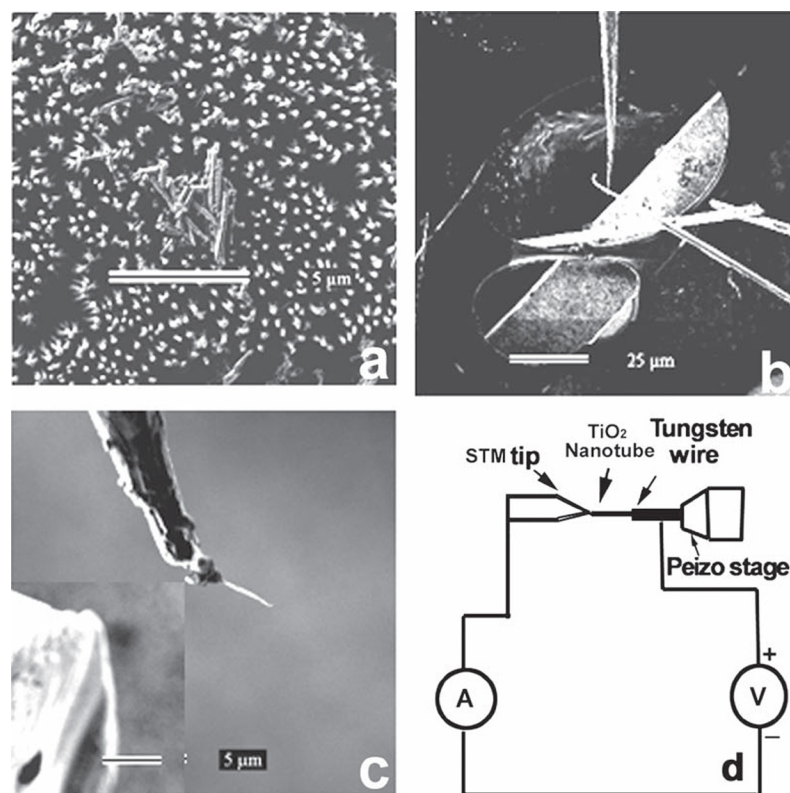


Figure 5.4 Images from the FIB system showing (a) the as grown TiO₂ nanotube sample; (b) FIB probe attached with a single nanotube dispersed on the Cu mesh (c) the FIB probe with a nanotube approaching the tip of the tungsten wire and (d) Schematic of the experimental setup for current–voltage measurement.

Figure 5.5(b) shows the image of the TiO₂ nanotube undergoing the heating at constant bias voltage of 10 V for 180 sec. The analysis of the image [Figure 5.5(b)] shows that the TiO₂ nanotube still maintains its morphological shape, but is broken into ultrafine particles. From previous reports,^{122, 127} it is known that the thermodynamic stability of TiO₂ particle is size dependent. Each phase has a particle size distribution and, at particle diameters less than 11 nm, the anatase is the most stable phase. The particle size in the anatase phase can range from 0.1 nm to 11 nm.¹²⁸ Therefore, from the

morphology of the particle size, it can be said that at this stage the nanotube is mainly comprised of ultrafine anatase particles. The diffraction pattern [inset, Figure 5.7(a)] and the lattice image taken from this stage of the heating also confirmed the presence of the anatase phase [Figure 5.7(a)]. The lattice fringe spacing is estimated to be ~ 0.357 nm, corresponding to the (101) plane of the anatase phase.

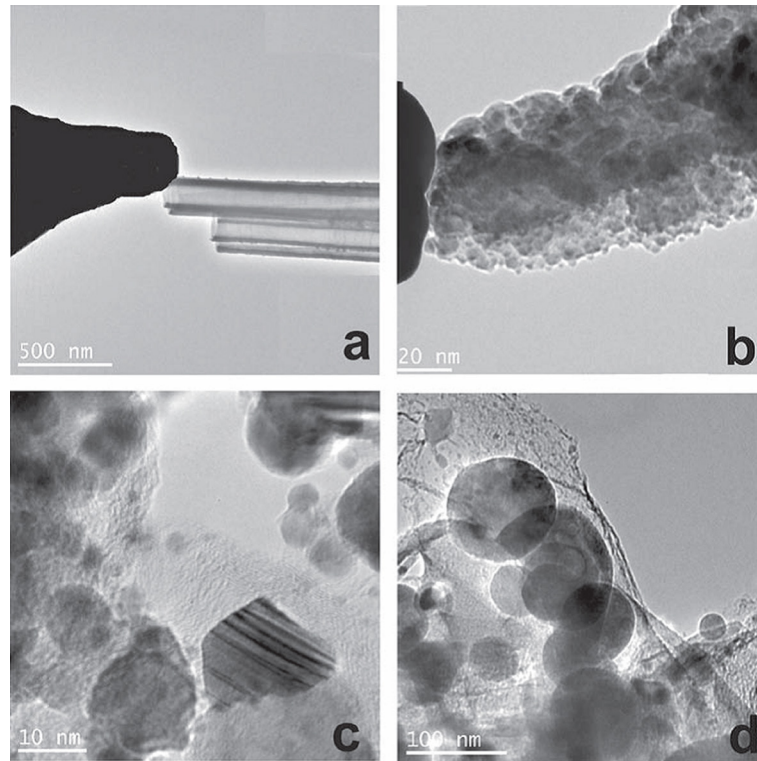


Figure 5.5 The BF image of the TiO₂ nanotube (a) in contact with the STM tip (b) undergone the heat treatment at constant bias voltage of 10 V for 180 seconds (c) the bias heated at 20 V for 130 seconds (d) undergone the bias heating at 30 V.

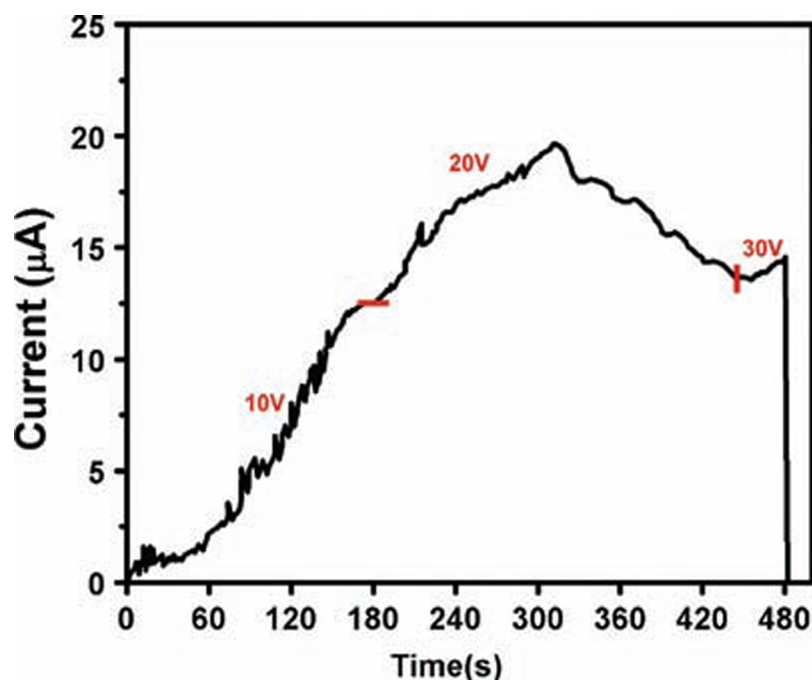


Figure 5.6 The current (I) versus time (t) plot for the TiO₂ nanotube under the different bias heating voltages, as marked in the plot.

On increasing the bias voltage to 20 V, it was observed that the current increased drastically to a maximum value of 20 μ A in a time period of 130 sec and then started to decrease gradually with the further breaking of the nanotube, while at the same time the nanometer diameter titania underwent a solid state reaction and grew into a bigger crystal of 20–25 nm [as shown in the image of Figure 5.5(c)], which is comparable to the particle size of around 30–35 nm for the rutile phase to become stable.¹²⁸ This leads to the alteration of phase stabilities and ultimately the anatase phase is converted into stable rutile phase. Furthermore, the presence of the rutile phase is also confirmed by the diffraction pattern and high resolution image taken from these particles, as shown in Figure 5.7(b), which corresponds to the tetragonal TiO₂ rutile phase ($a=4.59$ Å, $c=2.95$ Å, $P4_2/mnm$). The lattice fringe spacing is estimated to be ~ 0.321 nm, corresponding to the

interplanar distance of the (110) plane in the rutile phase. On increasing the bias heating voltage to 30 V, the current increased slightly from 13.75 μA to 15 μA in a time period of 30 seconds. Due to this increase in current at this stage, some of the rutile particles formed agglomerates of around 100–200 nm and finally the nanotube structure collapsed. The diffraction patterns of these agglomerations show that they are crystalline [Figure 5.7(c)].

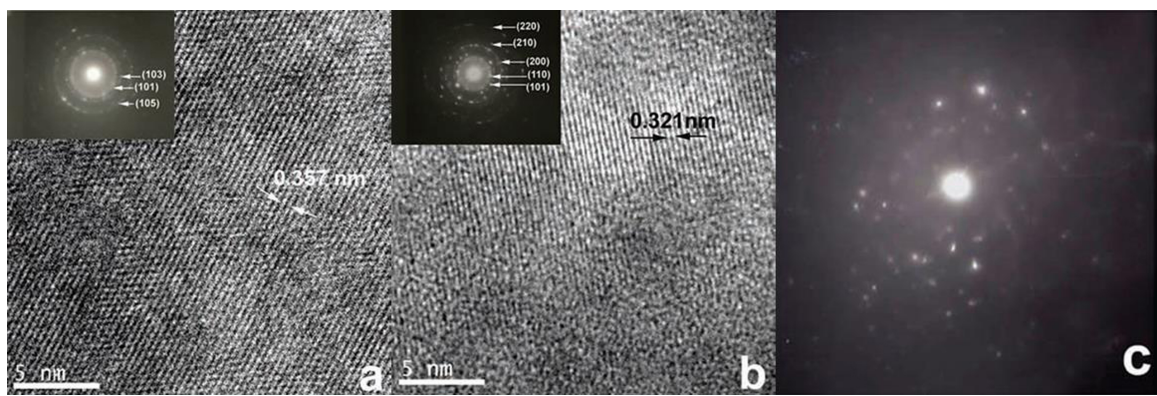


Figure 5.7 (a) The high resolution lattice image and the corresponding diffraction pattern (inset) taken from TiO_2 nanotube undergone a bias heating at 10 V (b) the high resolution lattice image of the nanotube bias heated at 20 V and the corresponding diffraction pattern (inset) (c) The diffraction pattern from the agglomeration formed at the bias heating of 30 V.

During the present investigations, it was observed that with bias heating in the STM–TEM system, the anatase TiO_2 nanotube was transformed into stable rutile particles. It can be concluded that when the TiO_2 nanotube was subjected to a bias voltage of 10 V for about 180 seconds, the nanotube resistively heated to elevated temperatures, which reduced the total resistance and a current of 12 μA could be detected. On further

increasing the bias voltage to 20 V, a high current of 20 μA flowed through the nanotube and the temperature was further increased. The nanometer sized anatase particles, having high surface area, became prone to solid state sintering, which led to grain growth and transformation to stable rutile particles with an average size between 20–25 nm. Eventually there is complete collapse of the structure, when the bias heating voltage is further increased to 30 V. At this stage, the rutile particles which are already under a heated condition form agglomerates of 100–200 nm with a slight increase of current of $\sim 2 \mu\text{A}$. Such processes are more pronounced during phase transformations, where bond breaking and enhanced mass transport take place, and this can lead to grain growth and densification.¹²⁹⁻¹³² Also in the case of anatase to rutile transformation, the mechanism responsible for the transformation are most likely a spatial disturbance of the oxygen ion framework and the shifting of the majority of Ti^{4+} ions by breaking two of the six Ti–O bonds to form new bonds.¹³³⁻¹³⁵ In the present case, a TiO_2 nanotube heated at a high bias voltage of 20 V, obtained sufficient energy to disturb the oxygen ion framework and form new bonds to form the rutile phase.

In the present investigations, the nanotube is resistively heated up and the temperature of the system is increased with the increase of current and the applied bias. It is difficult to estimate the temperature of the TiO_2 nanotubes undergoing the *in situ* Joule heating by any direct method. There are few reports on the Joule heating of multiwalled carbon nanotube, (MWCNT) and carbon onions by Huang *et al.*¹³⁶⁻¹³⁸ In these studies, the temperature of the different stages of heating of the carbon nanotube was estimated by matching the lattice images of graphite and diamond formed during the bias heating

and the known temperature at which these structures are generally formed. From the review report⁶² on the transformation of anatase nanotube to rutile particles, it was observed that when the anatase nanotube was annealed in the temperature range 500–600 °C (depending on the stability of the nanotube, hence the anodization condition), small protrusions come out through the porous structure. Above this temperature the tubule structure is completely collapsed, leaving dense rutile particles. The complete transformation to rutile occurs in the temperature range 620–680 °C. From the above observation, we can speculate that the temperature range for the transformation of anatase nanotube to rutile particles and then complete collapse of structure in the present study is between 600–800 °C.

5.4. Conclusion

In conclusion, we have shown that the anatase nanotube dissociation and their phase transformation to rutile in real time. The anatase nanotubes under Joule heating dissociate to small particles (~10–20 nm) of anatase at low bias voltage (≤ 10 V). At an intermediate bias range, between 10 V and 20 V, the anatase nanoparticles transformed to rutile phase. The size of the rutile nanoparticles can be controlled by the applied bias voltage. Under the bias heating condition with 30 V, the rutile particles agglomerate into large particles with sizes range up to 200 nm. It is known that thermodynamic stability of different phases of TiO₂ is size dependent and thus by controlling the size of the particles, we can control the properties of the TiO₂ used for various applications. By this synthesis method, we can easily have a rough estimation of the temperature at which the rutile particles can be formed by simply increasing or decreasing the bias voltage to heat the anatase

nanotube. Thus the present synthesis method of rutile particles by bias heating the anatase nanotube via STM–TEM system is a new, novel and fast method to get a clean (contamination free) and high quality rutile particles used for various photocatalytic applications.

Chapter 6 A Study on the Modulation of the Electrical Transport by Mechanical Straining of Individual Titanium Dioxide Nanotube⁴

6.1. Introduction

The semiconducting behavior of 1D titania (TiO_2) in various morphologies (tubes, wires, fibers, and rods) and large surface area have drawn considerable attention for potential applications in solar cells,¹³⁹ gas sensors, lithium ion batteries and biomedical systems.^{140, 141} However, the widespread technological use of titania is impaired by its wide band gap (3.2 eV), which requires ultraviolet (UV) irradiation for photocatalytic activation.^{140, 141} Traditionally, doping of the titania has been the approach taken for its band gap engineering.¹⁴²

Here, we propose an alternate way to enhance the electrical conductivity of TiO_2 nanotube using mechanical straining. A recent theoretical work on boron nitride

⁴The material contained in this chapter was previously published in the *Applied Physics Letters*. (Reprinted with permission from A. Ashtana, T. Shokuhfar, Q. Gao, P. Heiden, C. Friedrich, R. S. Yassar. *Applied Physics Letters*, 97, 072107 (2010). Copyright 2010, American Institute of Physics.)

nanotubes (BNNTs) under flattening deformation¹⁴³ has predicted the unique possibility of band gap tuning in a 2–5 eV range. This theoretical prediction on BNNTs has been experimentally verified by Bai *et al.*¹⁴⁴ by a series of *in situ* scanning tunneling microscopy (STM) experiments in a transmission electron microscop (TEM).

The crystal structure of the TiO₂ phase affects the photoelectrical current in solar cells and anatase based solar cells are expected to have the highest conversion efficiency. This effect has been attributed to the higher Fermi level in anatase in comparison to that of rutile by about 0.1 eV.¹⁴⁵ In view of this, we report here, the effect of mechanical deformation on an electrical response of an individual anatase TiO₂ nanotube. There are few reports on the electrical transport properties of an array of TiO₂ nanotubes and thin films.^{48, 146}

6.2. Experimental Procedure

All the electrical measurements were carried out on a single tilt STM-TEM holder in a JEM 4000FX TEM system that operated at 200 keV. In the present investigations, TiO₂ nanotube samples were synthesized by anodization of TiO₂ foils for 8 h at 60 V. The synthesis process is almost similar to that of reported by Schmuki and co-workers¹²⁵ and Djenizian and co-workers.¹²⁶

6.3. Results Discussion

The structural investigations of TiO₂ nanotube samples were carried out during the *in situ* TEM experiment. Figure 6.1(a) shows an overall view of the anatase titania nanotube, depicting a number of tubular nanostructures with uniform size distribution.

The tubes are hollow and open ended with an average inner and outer diameter of approximately 25 and 70 nm and the lengths range to several hundreds of nanometers. The corresponding diffraction pattern is shown in the inset [Figure 6.1(a)], depicting the anatase titania ($a=0.378$ nm, $c=0.9513$ nm, $I41/amd$). The HRTEM image [Figure 6.1(b)] taken from a single nanotube [inset of Figure 6.1(b)] shows that the nanotubes are well crystalline. The lattice fringe spacing of the walls of the nanotubes is estimated to be ~ 0.353 nm, corresponding to the interplanar distance of the (101) plane in the anatase phase.

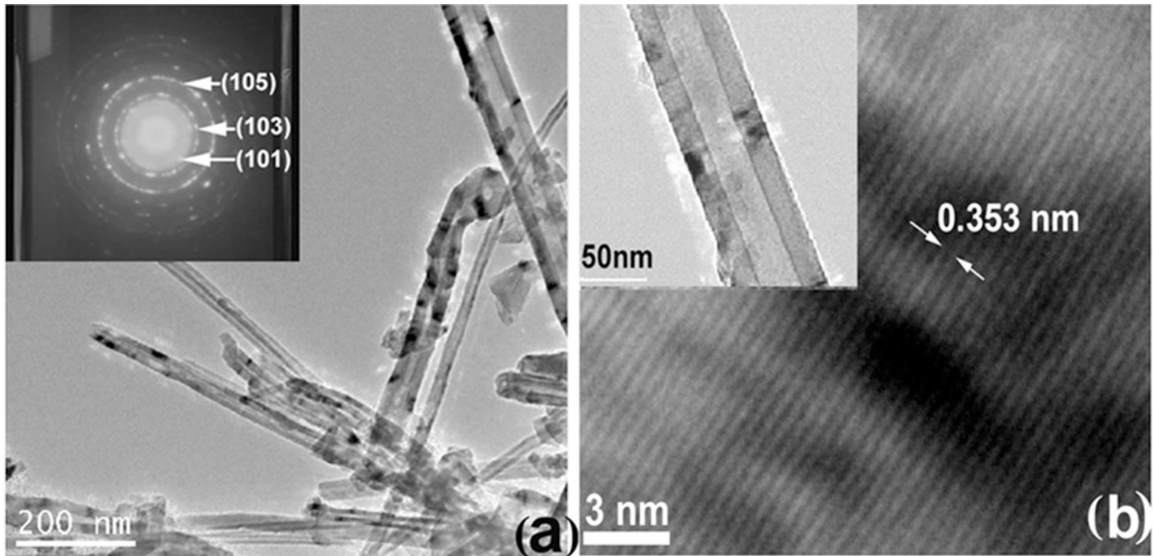


Figure 6.1 (Color online) (a) An overall view of the anatase titania nanotube and the corresponding diffraction pattern (inset) and (b) the high resolution lattice image from a single anatase nanotube (inset).

To ensure good electrical contact between the tip and the nanotube for *in situ* electrical measurement, an individual TiO_2 nanotube was attached to the electromechanically etched gold tip by tungsten deposition using the focused ion beam

(FIB) technique. The different steps of the sample preparation are shown in Figures 6.2(a)-6.2(c). In short, a nanotube was picked up using the FIB probe [Figures 6.2(a) and 6.2(b)] and attached on the gold tip [Figure 6.2(c)] by the tungsten deposition. The gold tip with TiO_2 nanotube was then transferred to the STM-TEM specimen holder and approached to its opposite conducting STM tip by the piezomanipulator. A schematic diagram of the experimental setup is shown in Figure 6.2(d).

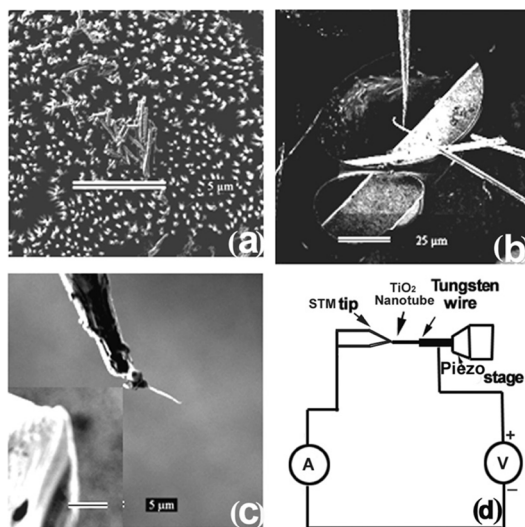


Figure 6.2 Images from the FIB system show (a) the as grown TiO_2 nanotube sample; (b) FIB probe attached with a single nanotube, dispersed on the Cu mesh; (c) the FIB probe with a nanotube approaching the tip of the tungsten wire and; (d) schematic of the experimental setup for current–voltage measurement.

Figures 6.3(a)-6.3(e) display the sequential images of a typical TiO_2 nanotube approaching the STM tip and undergoing a gradual increase in its bending curvature by incremental movement of the piezodriven gold tip toward the STM tip. A series of measured I - V curves at various stages of bending deformation are, respectively, shown in

Figure 6.3(f). The TiO₂ nanotube in contact with the STM tip [Figure 6.3(c)] shows a semiconducting behavior where electrical currents up to 10 nA can be detected under bias voltages up to 25 V [curve “c” in Figure 6.3(f) corresponding to Figure 6.3(c)]. The similar semiconducting electrical transport behavior was also observed for an array of anatase TiO₂ nanotube and thin films.^{48, 146} This is due to the intrinsic semiconducting behavior of the TiO₂ nanotube under the applied voltage. As we deform the nanotube, attached with the tungsten wire against the STM tip, current up to 18 nA can be observed (curve “d”) for the deformed state corresponding to Figure 6.3(d). With the increase in deformation [Figure 6.3(e)], the current is dramatically increased to 25 nA with start off voltage of 7.5 V bias as is evident from curve “e” [Figure 6.3(f)]. Figure 6.3(e) displays the TiO₂ nanotube in the highest deformed state under the present study, making a large bending curvature and corresponds to the state of the I - V curve “e.” In a large bias regime, the I - V curve can be differentiated to obtain a resistance R of the nanowire ($R \sim dV/dI$). We found that for this deformed state, the resistance of the nanotube was decreased to 0.34 G Ω from ~ 0.86 G Ω in the state corresponding to Figure 6.3(c).

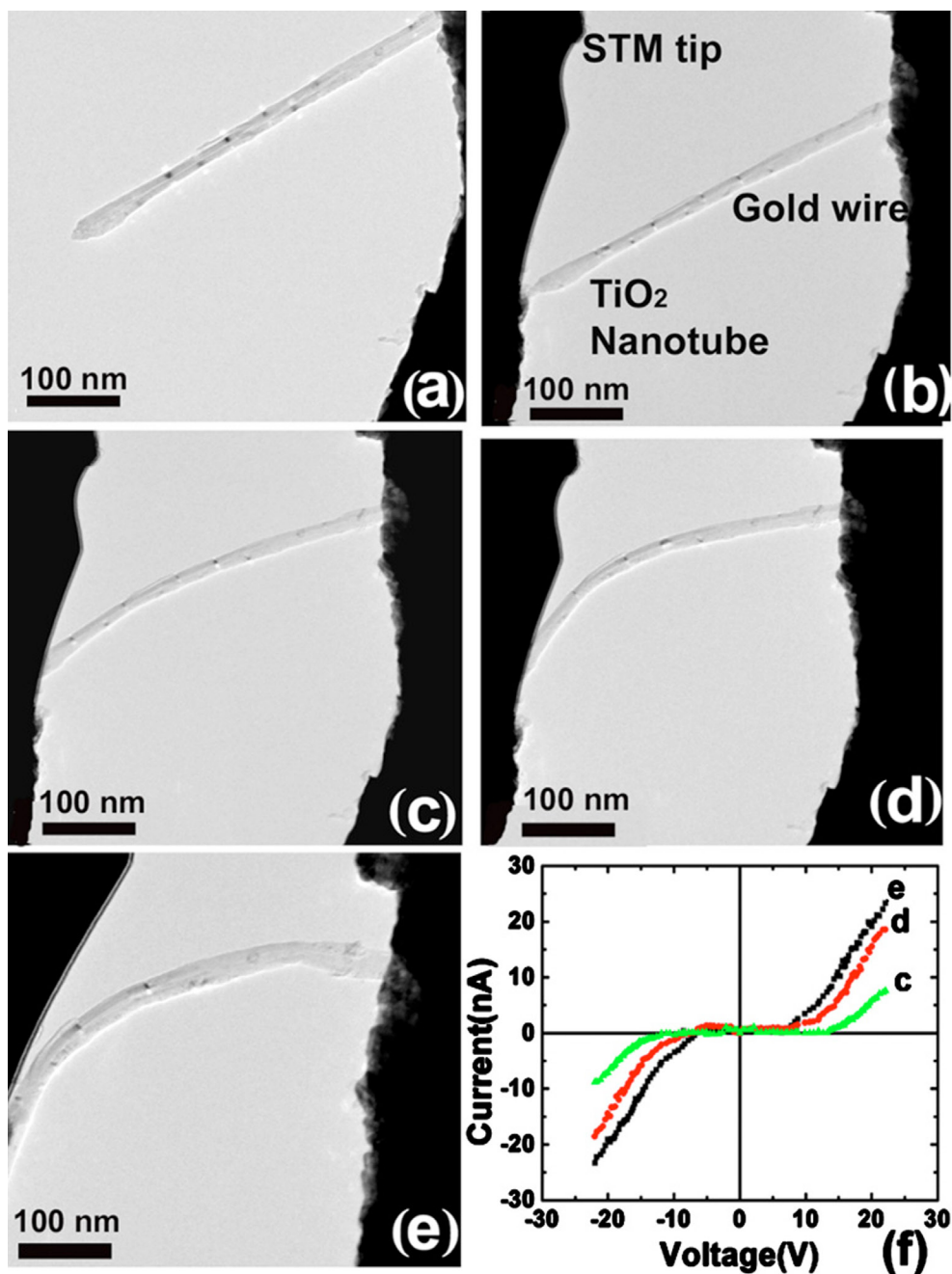


Figure 6.3 (Color online) The bight field image of the TiO₂ nanotube (a) approaching the STM tip; (b) in contact with the STM tip; [(c)–(e)] undergoing a gradual increase in its bending curvature; (f) a series of the representable I - V curves measured during the deformation of the TiO₂ nanotubes

The nonlinear and symmetrical I - V characteristics of these deformed states suggest a semiconducting behavior. Thus our measurement system can be regarded as a metal-semiconductor-metal (M-S-M) circuit.¹⁴⁷ The related semiconducting parameters can be retrieved from the experimental I - V data in the bias regime >5 V, by the following relation.^{144, 148}

$$\ln I = \ln S + V\left(\frac{q}{k_B T} - \frac{1}{E_0}\right) + \ln J_s. \quad (6.1)$$

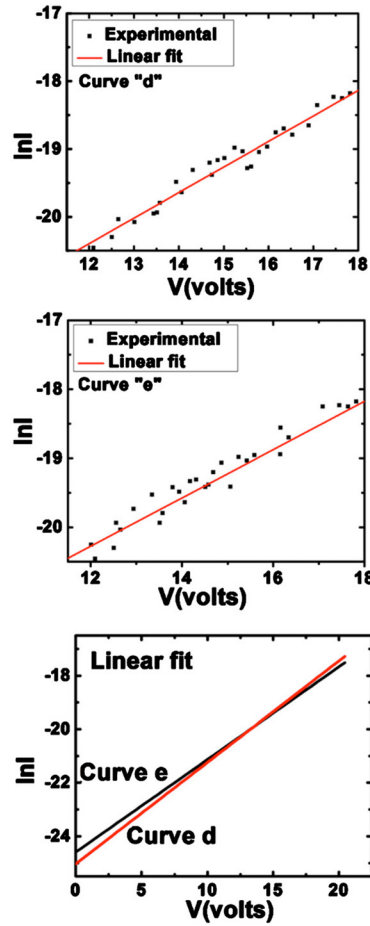


Figure 6.4 (Color online) The $\ln I$ - V curves corresponding to (a) curve d and (b) curve e in Figure 6.3(f), respectively. (c) The linear fits of the curves in [(a) and (b)].

Here S is the contact area associated with a bias, J_s is the saturation current density, and V is the slowly varying function of the applied bias. The $\ln I$ versus V plot gives an approximately straight line with a slope of $(q/k_B T) - 1/E_0$, and an intercept of $\ln S$. The representative $(\ln I)$ - V curves are depicted in Figures 6.4(a) and 6.4(b) corresponding to curve d and curve e in Figure 6.3(f), respectively. Figure 6.4(c) shows the linear fits of curve d and e extrapolated to the $\ln I$ axis, showing nearly identical values of intercept. This means, $\ln S$ and the contact area (S) is nearly identical for both of these stressed states. In the expression of $\ln I$, $E_0 = E_{00} \coth(E_{00}/k_B T)$, where $E_{00} = (hq/2)[n/(m^* \epsilon)]^{1/2}$. Here, q is the elemental charge, k_B is the Boltzmann constant, m^* is an effective electron mass of TiO_2 nanotube, and ϵ is the permittivity. We have estimated the specific sizes of the nanotube from the bright field TEM image and thus the resistivity ρ is obtained. The electron mobility, μ is then calculated by using the relationship $\mu = 1/(nq\rho)$. For anatase TiO_2 thin films, the dielectric constant, k is close to the value between 25–30, therefore, the value of permittivity, ϵ is taken as $\epsilon = 26\epsilon_0$,¹⁴⁹ ϵ_0 is the dielectric constant of a vacuum and $m^* = 1.26m_0$.²¹ Based on this procedure, the resistance, resistivity, carrier concentration and carrier mobility were extracted as summarized in Table 6.1. These values are in conformity with those obtained for the anatase TiO_2 thin films and single crystal of TiO_2 .¹⁵⁰⁻¹⁵³ The I - V measurements with bending deformation were repeated for several times to ensure the reproducibility of the data.

Table 6.1 Electrical Parameters of TiO₂ nanotube

Parameters	Curve c	Curve d	Curve e
Resistance (GΩ)	0.86	0.66	0.34
Resistivity (Ωcm)	43.5	36.4	13.36
E ₀ (meV)	23.98	24.9	27.0
Carrier concentration (cm ⁻³)	0.78X10 ¹⁷	1.58X10 ¹⁷	3.5X10 ¹⁷
Mobility (cm ² /Vs)	2.05	1.08	1.05

Under the present study, it was interesting to note that the electrical conductivity of TiO₂ nanotubes can be modulated by the mechanical deformation. Such phenomena can be related to the strain engineering of the electronic band gap structure in nanotubes.^{154, 155} It can be said that in the present study, when the anatase TiO₂ nanotubes are brought into deformed state, in-shell defects are produced at the walls of the nanotube. The possible defects can be voids, vacancies, and antisite atoms, which modify the band structure.¹⁵⁶ The carriers of current, i.e., electrons in this case (as TiO₂ is considered as *n* type semiconductor) are scattered strongly by the disordered structure, so that the mean free path of electrons may sometime be the order of the scale of the disorder. The pinning of the Fermi level is known to arise from the presence of defects,¹⁵⁷ such as dangling bonds and other misfits in the structure, which produce localized state in the gap. Hence, the TiO₂ nanotube in a higher deformed state will produce more defects, so a large number of electrons are scattered by the formation of a large number of defects. The

production of defects will also help in the pinning of the Fermi level, which will produce a localized state in the gap and hence help in the transport of the electrical current through the TiO₂ nanotube.

Another possibility for the increase in current by deformation can be due to the presence of dangling bonds at the surface of the TiO₂ nanotube. These defects can have a dominant role in modulating its electrical conductivity.^{158, 159} Surface defects can produce surface states within the band gap making the TiO₂ nanotube behaves like a weakly conductive metal. This allows the flow of conduction electrons near the surface region of the TiO₂ nanotube as also reported by Lin *et al.*¹⁶⁰

6.4. Conclusion

In conclusion, it was shown that the electrical transport properties of the TiO₂ nanotube could be enhanced by inducing deformation into the nanotube using an *in situ* STM-TEM stage. The semiconducting parameters were retrieved from the experimental *I-V* curves using the M-S-M model. Here, it can be emphasized that, considering the deformation driven electrical property modulation of the TiO₂ nanotube as observed in the present investigations, the TiO₂ nanotube holds a promising future and perspective candidate for constructing nanoscale electronic and optoelectronic devices and more importantly for its usage in solar cell applications.

Chapter 7 Deformation-Driven Electrical Transport in Amorphous TiO₂ Nanotubes⁵

7.1. Introduction

The fabrication of titanium dioxide (TiO₂) nanotubes has opened up new perspectives for applications in environmental purification,^{140, 161, 162} solar cells,^{90, 163} gas sensors,¹⁴⁰ lithium ion batteries,¹³⁹ and biomedical systems.¹⁴¹ In solar applications, one disadvantage is the high band-gap energy (~3.2 eV) of TiO₂, which means that the nanotube can be excited only by UV light ($\lambda < 380$ nm). In the last few decades, essentially two approaches were intensively investigated in order to make the material more responsive to the natural solar spectrum. One approach is to sensitize TiO₂ with a suitable dye to construct an efficient solar cell.^{164, 165} The other approach is by doping TiO₂ with impurities, e.g. transition metals or other elements,^{92, 142, 166-170} to obtain a good photocatalytic performance. When employing dopants to change the electrical response

⁵The material contained in this chapter was previously published in the *Applied Physics A: Materials Science & Processing*. (Reprinted with permission from A. Ashtana, T. Shokuhfar, Q. Gao, P. Heiden, R. S. Yassar. *Applied Physics A: Materials Science & Processing*, 109, 127 (2012). Copyright 2012, Springer.)

of a material, the concern is to maintain the integrity of the host material crystal structure while changing its band-gap structure.

Here, we investigate the role of mechanical straining in tuning the electrical transport of TiO_2 nanotubes. A recent theoretical work on boron nitride nanotubes (BNNTs) under flattening deformation¹⁷¹ has predicted the unique possibility of band-gap modification in the 2–5 eV range. The density function calculations show that mechanical deformation affects the conduction energy bands more effectively than energy levels in valence bands. The overall outcome was the reduction of the gap between valence and conduction bands. This theoretical prediction has been experimentally verified by a series of in situ transmission electron microscopy (TEM) experiments.¹⁴⁴

The crystalline, or amorphous, nature of the titania nanotubes varies with processing techniques and parameters.⁹⁰ The anatase-based solar cells have shown the highest conversion efficiency,⁶² and therefore their electrical properties have been investigated in more detail.^{48, 172, 173} Our study of the deformation-driven electrical transport measurement of anatase nanotubes has also shown a higher value of electrical current compared with that of amorphous nanotubes.¹⁷⁴

The as-synthesized TiO_2 nanotubes are an amorphous material and hence electrically not very conductive. In the present study, we are trying to investigate the electrical property of an amorphous TiO_2 nanotube by mechanically deforming it and expect to change its band structure by mechanical straining. Interestingly, there are no studies of the electrical transport phenomenon aspect of individual amorphous TiO_2 nanotubes. This

research aims to fulfill this gap and to determine the role of mechanical deformation on electrical transport of amorphous titania nanotubes.

7.2. Experimental section

The *in situ* electrical transport measurement was conducted in a high-resolution transmission electron microscope (TEM) using a STM–TEM system from Nanofactory Instruments. The STM–TEM system provides a unique combination of transmission electron microscopy and scanning tunneling microscopy techniques, which are used simultaneously in one instrument for full sample characterization. It consists of a STM-equipped TEM sample holder, a controller, and a PC with Nanofactory's data acquisition software. All the measurements were carried out on a single tilt STM–TEM holder in a JEM 4000FX TEM, operated at 200 kV. The setup of the STM–TEM holder is shown in Figure 7.1. The electrochemically etched gold wire with TiO₂ nanotubes was attached to the piezo-driven movable part of the holder facing the fixed and sharp tungsten STM tip as its counter electrode, and oriented perpendicular to the electron beam in the TEM. In such an arrangement, atomic scale imaging and $I-V$ measurements were carried out concurrently. The contact was made between the STM tip and the TiO₂ nanotube by the precision movement of the gold wire (with the sample) attached to the piezo-driven manipulator. Joule heating was conducted by applying different bias voltages to the gold electrode with the nanotube sample at its tip, while the tungsten STM tip was grounded. In the present investigation, TiO₂ nanotube samples were synthesized by anodization treatment in a two-electrode electrochemical cell in an electrolyte containing dimethyl sulfoxide (DMSO) and hydrofluoric acid. The anodization voltage, HF concentration in

DMSO, and duration of anodization were 60 V, 2 wt%, and 40 h, respectively. Details of the synthesis process are published elsewhere.¹⁷⁵ There are several reports on the synthesis of TiO₂ nanotubes by the anodization method.^{81, 176-181} In contrast to other methods of producing the TiO₂ nanotubes,^{46, 182-185} the electrochemical anodization approach is self-organizing and it leads to an array of oxide nanotubes aligned perpendicular to the substrate surface and to a well-defined and controllable tube length. The tubes remain attached to the metal surface and are electrically connected and easy to handle.

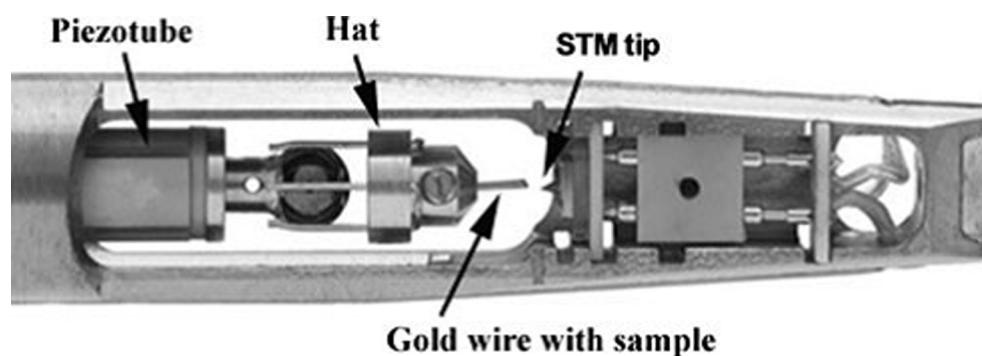


Figure 7.1 The image shows the experimental configuration for the STM–TEM holder

7.3. Results and discussion

The structural investigations of TiO₂ nanotube samples were carried out during the *in situ* TEM experiment. Figure 7.2 is a low-magnification bright field image of the as-synthesized amorphous TiO₂ nanotubes. The general morphology shows that the amorphous TiO₂ nanotubes are hollow and closed ended. The nanotubes have average outer and inner diameters of 100 nm and 50 nm, and the wall thickness of the tubes is not

uniform. The corresponding diffraction pattern (inset in Figure 7.2) clearly shows that the tubular structures are amorphous.

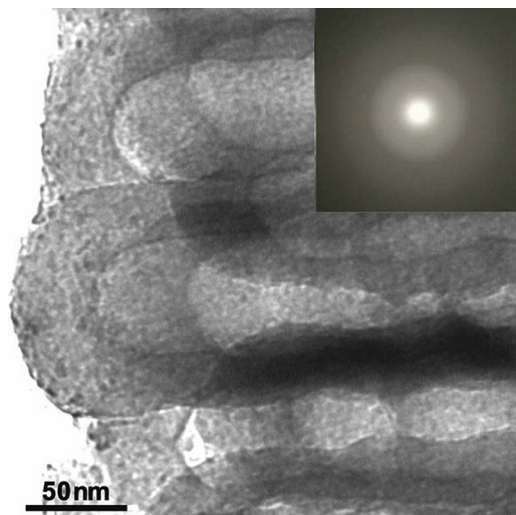


Figure 7.2 TEM bright field (BF) image of the amorphous TiO₂ nanotubes and its corresponding electron diffraction pattern (inset).

For in situ electrical measurement, individual TiO₂ nanotubes were attached to the electromechanically etched tungsten tip by tungsten deposition using the focused ion beam (FIB) technique to ensure good electrical contact between the tip and the nanotubes. The different steps of the sample preparation are shown in Figures 7.3(a)–7.3(c). In short, a nanotube was picked up using the FIB probe (Figures 7.3(a) and 7.3(b)) and attached on the tungsten tip (Figure 7.3(c)) by the tungsten deposition. The tungsten tip with the TiO₂ nanotube was then transferred to the STM–TEM specimen holder and directed to its opposite conducting STM tip by the piezo manipulator. A schematic diagram of the experimental setup is shown in Figure 7.3(d).

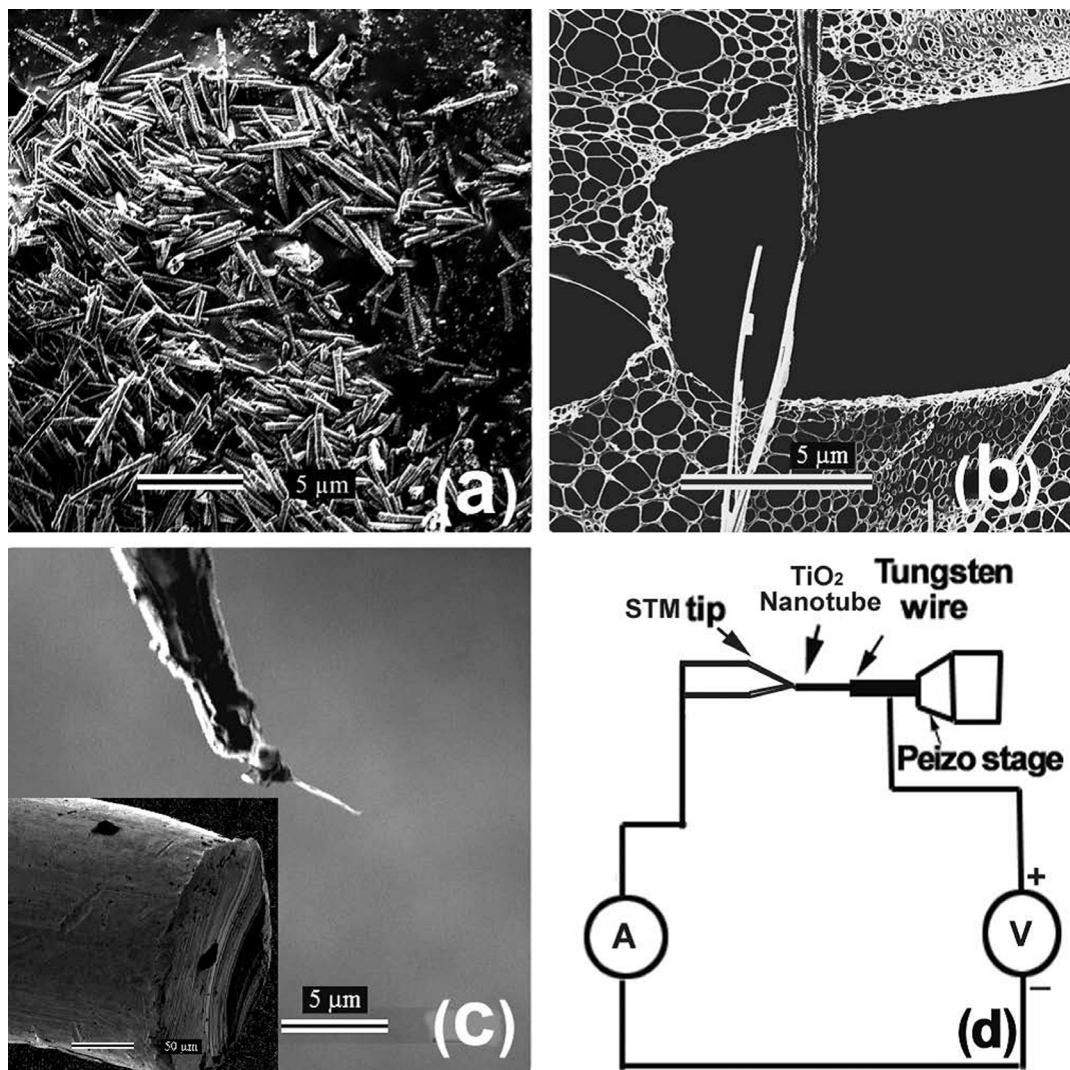


Figure 7.3 Images from the FIB system showing (a) the as-grown TiO₂ nanotube sample, (b) the FIB probe attached with a single nanotube, dispersed on the Cu mesh, (c) the FIB probe with a nanotube approaching the tip of the tungsten wire, (d) schematic of the experimental setup for current–voltage measurement.

For electrical measurement, it is important to have good physical contact between the nanotube and the two opposite electrodes. In this investigation, when the nanotube was brought in contact with the STM tip by the nanomanipulator, a current of several nA

was allowed to pass through the electrode–nanotube circuit. Due to the passage of this current for a very short time (less than 2 s), the temperature of the contact point between the nanotube and the STM tip will increase and the nanotube is welded to the STM tip. This will help in making a good physical contact between the nanotube and the STM tip. Figure 7.4(a) shows a TiO₂ nanotube attached on the gold electrode as it approaches the opposite electrode, i.e. the STM tip, by the nanomanipulator. In Figure 7.4(b), the TiO₂ nanotube is shown in contact with the STM tip and gold electrode. Figures 7.4(c)–7.4(e) display the sequential images of a typical TiO₂ nanotube undergoing a gradual increase in its bending curvature by incremental movement of the piezo-driven gold tip toward the STM tip.

A series of measured $I - V$ curves at various stages of bending deformation are respectively shown in Figure 7.4(f). For the TiO₂ nanotube that is just in contact with the STM tip and the nanotube that is in a slightly deformed state (curves ‘a’ and ‘b’ respectively in Figure 7.4(f)), the current is practically negligible, only a few nA is able to be detected. This result confirms the insulating behavior of undeformed or just slightly deformed nanotubes, and can be attributed to less contact area, high contact resistance, and the intrinsic amorphous nature of the material.

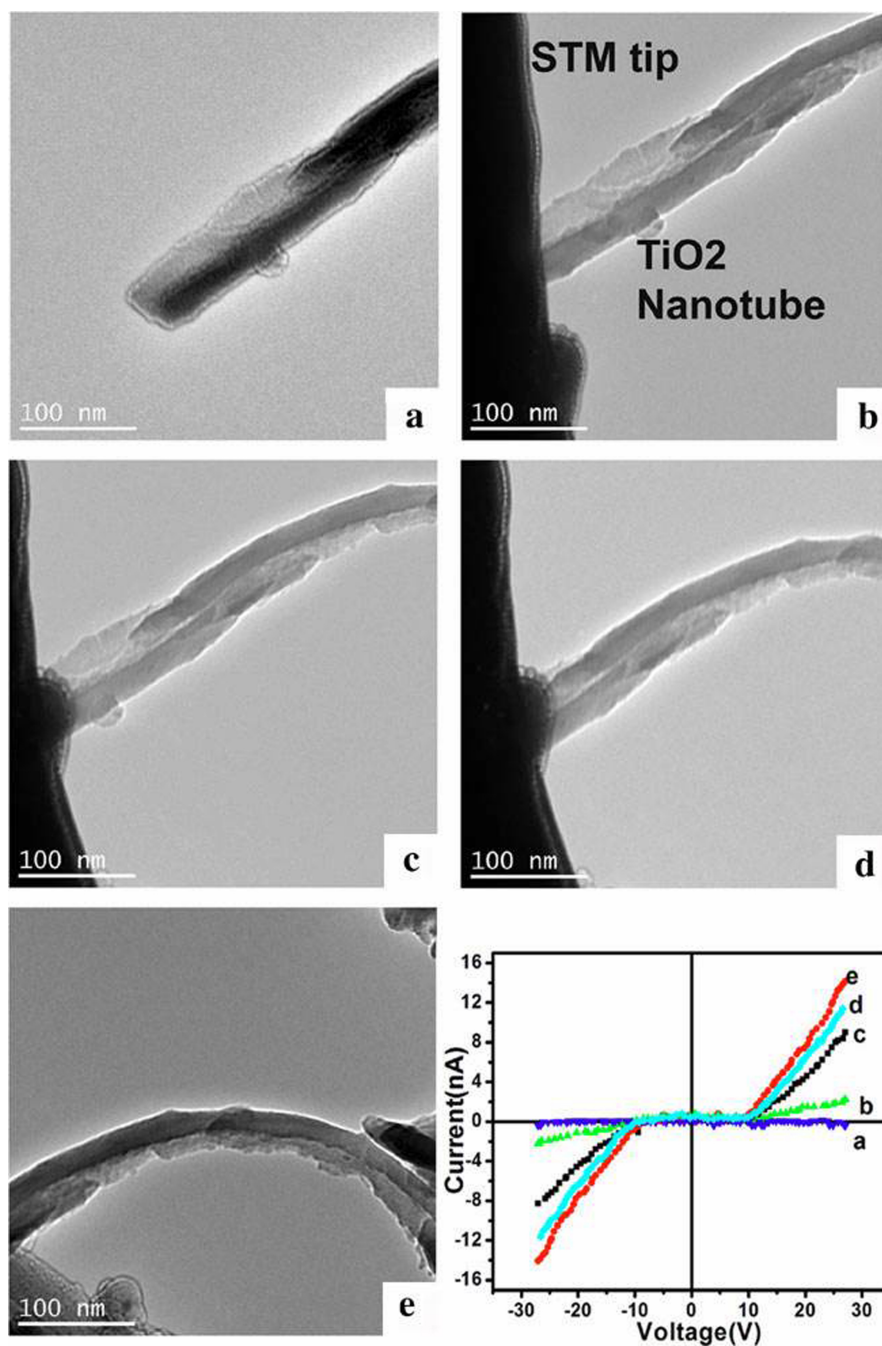


Figure 7.4 The bright field image of a TiO₂ nanotube (a) approaching the STM tip, (b) in contact with the STM tip, (c), (d), and (e) undergoing a gradual increase in the bending curvature, (f) a series of the representative $I-V$ curves measured during the deformation of the TiO₂ nanotubes.

Amorphous materials possess high resistance due to their internal structural disorder, as compared to the more orderly crystal structure of crystalline materials.^{186, 187} Figure 7.4(c) shows the TiO₂ nanotube in a slightly deformed state during the compression process. As we deform the nanotube by delicate driving of the tungsten tip with the nanotube against the STM tip, currents up to 8.23 and 14.58 nA can be observed at the same bias voltage range (curves 'c' and 'e'). The I - V curve of the TiO₂ nanotube in the highly bent state was also examined during the unloading and an almost similar trend in the I - V curve was obtained with maximum value of the current (~ 11.37 nA, curve 'd'), which is smaller compared to ~ 14.58 nA obtained for the highly bent state as shown (curve 'e'). However, the value of the current is much higher than that obtained in the state of the nanotube (Figure 7.4(b)) before any deformation, which indicates that defects introduced during bending of the nanotube remain in the nanotube in the relaxed state. In a large-bias regime, the I - V curve can be differentiated to obtain a resistance R of the nanotube ($R \sim dV/dI$). The nanotube's resistance, R , for this state (Figure 7.4(d)) was calculated to be ~ 2.0 G Ω (curve 'c'). With the increase in deformation, the current is dramatically increased at the starting bias voltage of 7.5 V as is evident from curve 'e' (Figure 7.4(f)). Figure 7.4(e) displays the TiO₂ nanotube in the highest deformed state under the present study, and the corresponding I - V curve is marked as 'e'. We found that for this highly deformed state, the resistance of the nanotube was decreased to 0.98 G Ω . The comparison of these values indicates that the resistance of TiO₂ nanotubes decreases as mechanical straining increases.

The nonlinear and symmetrical I - V characteristics of these deformed states suggest a semiconducting behavior. Thus, our measurement system can be regarded as a metal–semiconductor–metal (M–S–M) circuit.¹⁴⁷ The related semiconducting parameters can be retrieved from the experimental I - V data in the bias regime >5 V, by the following relation:^{144, 188} $\ln I = \ln S + V \left(\frac{q}{k_B T} - \frac{1}{E_0} \right) + \ln J_s$. Here S is the contact area associated with a bias and J_s is a slowly varying function of the applied bias. The $\ln I$ versus V plot gives an approximately straight line with a slope of $\left(\frac{q}{k_B T} \right) - \frac{1}{E_0}$ and an intercept of $\ln S$. The representative $\ln I$ - V curves are depicted in Figures 7.5(a) and 7.5(b), corresponding to curves c and e in Figure 7.3(f), respectively. Figure 7.5(c) shows the linear fits of curves c and e extrapolated to the $\ln I$ axis, and shows that they have nearly identical intercept values. This means that $\ln S$ and the contact area (S) are nearly identical for both of these stressed states. In the expression of $\ln I$, $E_0 = E_{00} \coth\left(\frac{E_{00}}{k_B T}\right)$, where $E_{00} = \left(\frac{\hbar q}{2}\right)\left(\frac{n}{m^* \varepsilon}\right)^{1/2}$. Here, q is the elemental charge, k_B is the Boltzmann constant, m^* is an effective electron mass of the TiO₂ nanotube, and ε is the permittivity of the material. We estimated the specific sizes of the nanotubes from the bright field TEM images and thus the resistivity, ρ , was obtained. The electron mobility, μ , was then calculated by using the relationship $\mu = \frac{1}{nq\rho}$. For TiO₂ thin films, $\varepsilon^* = 7\varepsilon_0$,^{189, 190} ε_0 is the permittivity of the vacuum and $m^* = 0.71m_0$.^{191, 192} Using this procedure, the resistance, resistivity, carrier concentration, and carrier mobility were extracted, and are summarized in Table 7.1. We did not estimate the carrier density of the nanotube from the I - V curve corresponding to

curve c (Figure 7.4(f)) as the resistance is very high ($\sim 2 \text{ G}\Omega$). An amorphous material has high resistance due to the disordered atomic-scale structure.^{186, 187}

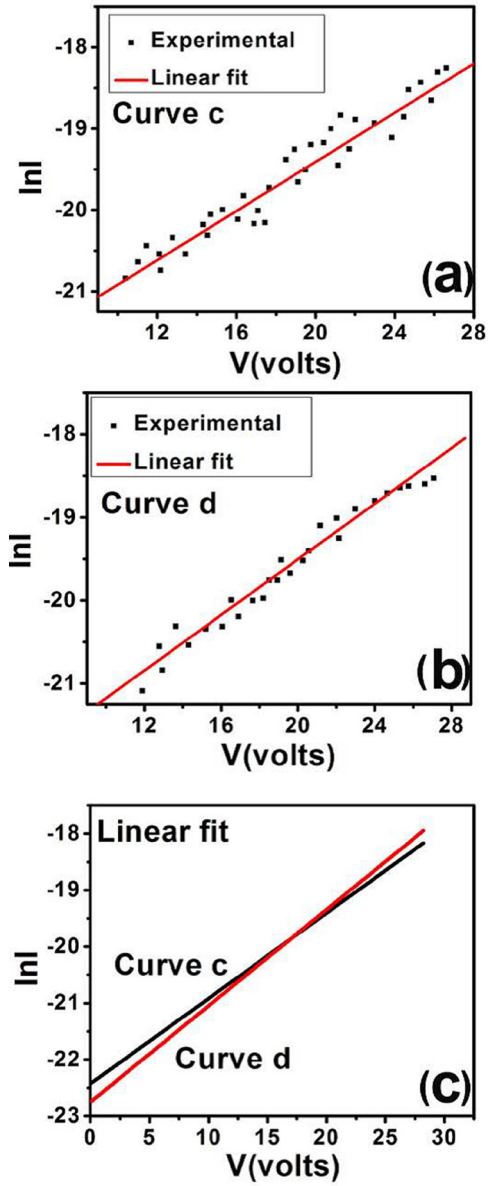


Figure 7.5 The $\ln I$ - V curves corresponding to (a) curve c and (b) curve e in Figure 7.4(f), respectively. (c) The linear fits of the curves in (a) and (b).

In the present study, the electrical conductivity of the amorphous TiO₂ nanotube is tuned from that of an insulator to a semiconductor under the deformed state. This effect can be related to the modification of the band structure of the nanotube under strain.¹⁹³⁻¹⁹⁶ An amorphous TiO₂ nanotube can be considered as an amorphous semiconductor. One possibility is that when the amorphous TiO₂ nanotubes are subjected to mechanical straining, structural defects like voids, vacancies, and antisite atoms are produced inside the nanotubes, which can alter the band-gap properties.¹⁹⁷ It is changes in the short-range order (on the scale of a localized electron) that have a profound effect on the properties of amorphous semiconductors. The carriers of current, i.e. electrons in this case (as TiO₂ is considered as an n-type semiconductor), are scattered strongly by the disordered structure, so that the mean free path of electrons may sometimes be on the order of the scale of the disorder and the current flows through the amorphous TiO₂ nanotube. Also, amorphous materials appear to behave almost like intrinsic semiconductors with the Fermi level lying near the center of the gap. However the pinning of the Fermi level is known to arise from the presence of defects,¹⁵⁷ such as dangling bonds and other flaws in the structure, which produce localized states in the gap. Hence, the amorphous TiO₂ nanotube in a higher deformed state will produce more defects, so a large number of electrons are scattered by the formation of a large number of defects. The production of defects will also help in the pinning of the Fermi level and produce a localized state in the gap.

Table 7.1 Electrical parameters of TiO₂ nanotube

Parameter	Curve c	Curve d
Resistance (G Ω)	2.0	0.98
Resistivity (Ω cm)	50.28	19.23
Carrier concentration (cm ³)	–	1.15 x 10 ¹⁷
Mobility (cm ² /V s)	–	2.59

TiO₂, being an ionic transition-metal oxide, exhibits strong electron–phonon coupling, resulting in low room temperature electron mobilities in the material.¹⁹⁸⁻²⁰⁰ We, therefore, believe that an alternative possibility to increase electrical conductivity is the electron–phonon coupling effect. This electron–phonon coupling effect causes the formation of a polaron,²⁰¹ a quasi-particle consisting of an electron and the accompanying lattice deformation. These polarons display self-trapping of the electron and localized wave functions, with charge transport typically occurring through tunneling or thermally activated hopping. During the whole process of I – V measurement, i.e. bringing the nanotube towards the STM tip and carrying out I – V measurement, we tried to minimize the electron beam effects by decreasing the beam current density as low as possible, just required for the imaging. Finally, during the sweeping of the bias voltage for the I – V curve, we shut off the electron beam. So, there are fewer chances that interaction of high-energy electrons with a semiconductor material will induce the formation of electron–hole pairs (e^-/h^+) in the TiO₂ nanotube. It is speculated that in the present case, the

deformation-driven electrical conduction is dominating over the electron–phonon coupling effect induced conduction.

From the bright field image (Figure 7.(4)), it is apparent that the nanotube was slightly ruptured from the upper part; however, it should be mentioned that the TiO_2 nanotube shown in Figure 7.4 is not broken, otherwise it would not be possible to measure the electrical conductivity. It was difficult to get a clean nanotube for this experiment. Since for measuring the electrical conductivity, the nanotubes have to be glued at the tip of the gold wire, and the nanotube samples are scratched from the substrate (on which they are grown) by the gold wire, and some time during the scratching, a part of the nanotube is ruptured, probably due to the amorphous nature of the sample.

7.4. Conclusion

In conclusion, we have successfully carried out in situ electrical transport measurements on an individual amorphous TiO_2 nanotube inside a high-resolution transmission electron microscope equipped with a STM probe. It was shown for the first time that the electrical transport properties of the amorphous TiO_2 nanotube could be tuned from insulating to semiconducting by inducing deformation. The semiconducting parameters were retrieved from the experimental I – V curves using the M–S–M model. The considerable enhancement in electrical transport of amorphous TiO_2 nanotubes offers new opportunities to build flexible or stretchable solar cells based on amorphous titania, where the conversion efficiency is comparable to anatase-based solar cells. If this can be

integrated successfully, the annealing process of amorphous nanotubes can be eliminated from the solar cell manufacturing process, which can result in lower consumption of energy resources and saving costs.

Chapter 8 Evidence of Lithium-induced Atomic Ordering in Amorphous TiO₂ Nanotubes⁶

8.1. Introduction

The next generation of Li ion batteries (LIB) has drawn much interest because of their applications in hybrid electric vehicles (HEVs),²⁰² plug-in hybrid electric vehicles (PHEVs),²⁰³ and other electric utilities. Graphite is a widely used anode material in commercial LIB. However, graphite has several drawbacks such as low theoretical capacity and capacity fading.²⁰⁴ To circumvent these problems, several new materials have been developed to replace the graphite, including Si,²⁰⁵ Sn,²⁰⁶ Co₃O₄,²⁰⁷ and Ge.²⁰⁸ However, a major limitation of these alternatives is that they experience large volume changes in the first cycle, leading to cracking, fracture, and in turn, capacity fading and failure of batteries.

In recent years, TiO₂-based materials have been considered to be a viable alternative to graphite electrodes due to the stable capacity retention and safe operation in intercalation.^{204, 209, 210} TiO₂ has almost the same theoretical capacity (~336 mAh/g) as

⁶The material contained in this chapter has been submitted to the *Advanced Functional Materials*. Copyright transfer agreement will become effective only after being accepted.

that of commercial-grade graphite (~ 372 mAh/g), but the volume expansion is less than 3%.¹² In addition, the operation voltage of graphite is 0.1 V (Li^+/Li redox couple), which may cause an explosion during charging. But for TiO_2 , it is as high as 1.7 V (Li/Li^+ redox couple). The higher operation voltage results in safer battery operation with lower self-discharge and good capacity retention during cycling.⁴ In addition, this property will make TiO_2 to be compatible with several novel cathode materials (LiCoPO_4 ¹⁴ and $\text{LiCo}_{0.5}\text{Mn}_{1.5}\text{O}_4$ ¹⁵) to achieve Li-ion batteries with high voltage (~ 5 V).

Nanotubular structures of TiO_2 can be a better choice for TiO_2 -based anodes due to their larger specific surface area, shorter diffusion length, and faster kinetics of electrochemical reactions. TiO_2 nanotubes can be produced by a simple anodization method, eliminating the need for costly or sophisticated fabrication processes.¹⁷⁶ Additionally, the Pt counter electrode can be replaced by copper, which makes it more economically feasible for mass production.²¹¹

The *in situ* electrochemical lithiation study in TEM allows direct observation of morphological and chemical evolution in real time. The authors²¹² and Huang *et al.*²¹³ pioneered the concept of an “open-cell” design to study the electrochemical behavior of battery electrode materials. This cell is made of a single nanowire as anode, ionic liquid or solid Li_2O as electrolyte, and LiCoO_2 or lithium metal as cathode. This method of observation can provide atomic-level spatial resolution and analytical capability to study Li ions insertion mechanisms into electrode materials during the charge/discharge cycle.^{212, 214-217} Since its invention, this technique has revealed many details about the

lithiation mechanisms in Si,^{214, 215, 218-223} Ge,²²⁴ Al₂O₃,²²⁵ SnO₂,^{213, 217, 226-228} ZnO,²²⁹ graphene,²³⁰ and carbon nanotubes²³¹ that were unknown to the Li-ion battery community.

Interestingly, in spite of extensive *ex-situ* electrochemical testing on TiO₂ nanotubes, no direct TEM evidence on their lithiation behavior has been reported. In the present work, for the first time, *in situ* studies of electrochemical lithiation of amorphous TiO₂ nanotubes (a-TNTs) inside high-resolution TEM will be reported. Electron energy loss spectroscopy (EELS) was also conducted to better understand the changes in chemical and electronic properties. The finding of this study provides the first direct insight into the details of lithiation mechanism, chemical, structural, and electronic evolution for a-TNTs as anode materials. High resolution TEM (HRTEM) analysis revealed the formation of crystalline islands of Li₂Ti₂O₄ in the lithiated amorphous matrix.

8.2. EXPERIMENTAL METHODS

8.2.1. TiO₂ Nanotube Synthesis

The TiO₂ nanotubes were grown by the anodization setup. Titanium foil (Sigma-Aldrich, 0.25 mm thick, 99.99%) was used as the substrate for growth of the oxide nanotube arrays. The foils were sonicated in the sequence of ethanol, deionized water, and acetone for 10 minutes each. Titanium foils served as the anodic electrode while platinum was used as the cathodic electrode. Electrolyte used in the experiment was 0.2 wt% NH₄F solution in a plastic beaker, which was prepared by NH₄F crystals, ethylene glycol, and deionized water with the ratio of 49:1 that helped dissolve the NH₄F crystals. The anodization process was conducted at the voltage of 40 V for the processing time of

8 hours at room temperature. Upon completion of the anodization, the titanium foils were rinsed with deionized water and dried in the atmosphere. The products were characterized by a field emission scanning electron microscopy (FE-SEM) (Hitachi S-4700, Japan) under the operating voltage of 10 kV.

8.2.2. *In Situ* TEM Setup

The TiO₂ nanotubes with the substrate of titanium foil were treated with ethanol for one day and air-dried for two days. The nanotubes were scratched off from the film and then glued to a tungsten (W) tip with conductive epoxy. Lithium metal was scratched by a gold (Au) wire inside the glove box, and transferred by a sealed container with Ar gas. The W and Au wires were mounted on the stationary and piezo-movable sides of an *in situ* scanning tunneling microscope (STM) that operated inside a TEM, respectively. The naturally grown Li₂O layer on the Li metal worked as a solid electrolyte. The Li₂O/Li electrode side was moved forward to contact one of the TiO₂ nanotubes. Once a reliable electrical contact was built, a potential ranging from -2 to -4 V was applied to the TiO₂ nanotubes to initiate the lithiation. The in situ TEM experiments were performed using an aberration-corrected scanning transmission electron microscope (ARM 200CF, JEOL, Japan) as well as a high resolution TEM (JEOL4000FX) operated at 200 keV.

The EELS signals were acquired using a Gatan Image Filter (Quantum 965, GATAN, USA) with a 2k×2k pixels CCD camera, which allows simultaneous acquisition of the low loss and high loss region. The EELS studies were conducted in the scanning transmission electron microscopy (STEM) mode on a Titan 80-300 (FEI, USA) operated

at 300 keV with an energy dispersion of 0.25eV/channel and an energy resolution of ~ 0.9 eV.

8.3. RESULTS AND DISCUSSION

The *in situ* lithiation setup where Li metal with Li₂O is placed on the gold wire and a-TNTs are attached to the STM tip is shown in Figure 2.3. Using piezo-driven stage with nm precision, the Li/Li₂O was moved toward individual nanotubes. Once a reliable contact was made, the bias voltage of -3 V was applied to the nanotubes to trigger the lithiation process. The details about experimental method are discussed in the supporting information.

Figure 8.1(a-f) illustrates the lithiation process of an a-TNT in real time. When the free-end of the a-TNT contacted with Li₂O, the lithiation process started (under the applied voltage of -3 V) with the formation of a layer on the surface of the a-TNT. The progress of this surface layer as a function of time is marked by a blue dot square.

In order to better understand the structure of this surface layer, HRTEM images of nanotubes before and after lithiation were compared. Figure 8.1(g) shows a pristine a-TNT with the diameter of 107 nm. After lithiation, a layer was formed on the surface of the nanotube. The thickness of this layer was estimated to be 11 ± 2 nm as marked by the white arrows in Figure 8.1(h). A selected area electron diffraction (SAED) pattern was recorded on the layer as shown in Figure 8.1(i). The indexed (111), (220) and (311) planes correspond to Li₂O phase indicating that the surface layer is made of polycrystalline Li₂O.

The formation of Li_2O layer observed on the surface of TiO_2 nanotubes during lithiation can be explained knowing that Li ions can react with the residual oxygen in the TEM chamber to form Li_2O . This situation is more likely to happen during the lithiation of intercalation materials since the rate of Li ions intercalation is limited due to the restriction in available interatomic spaces and diffusion channels. This scenario is in synergy with the observation of Liu *et al.*,²³¹ who reported a similar surface Li_2O layer on the multiwall carbon nanotubes (MWCNTs), which is an intercalation material. The formation of this Li_2O layer can also be attributed to reaction of Li with residual oxidic groups including carboxylic acid, epoxy, or hydroxyl groups.²³² These groups can form on the surface of TiO_2 nanotubes during the electrochemical anodization process.²³³

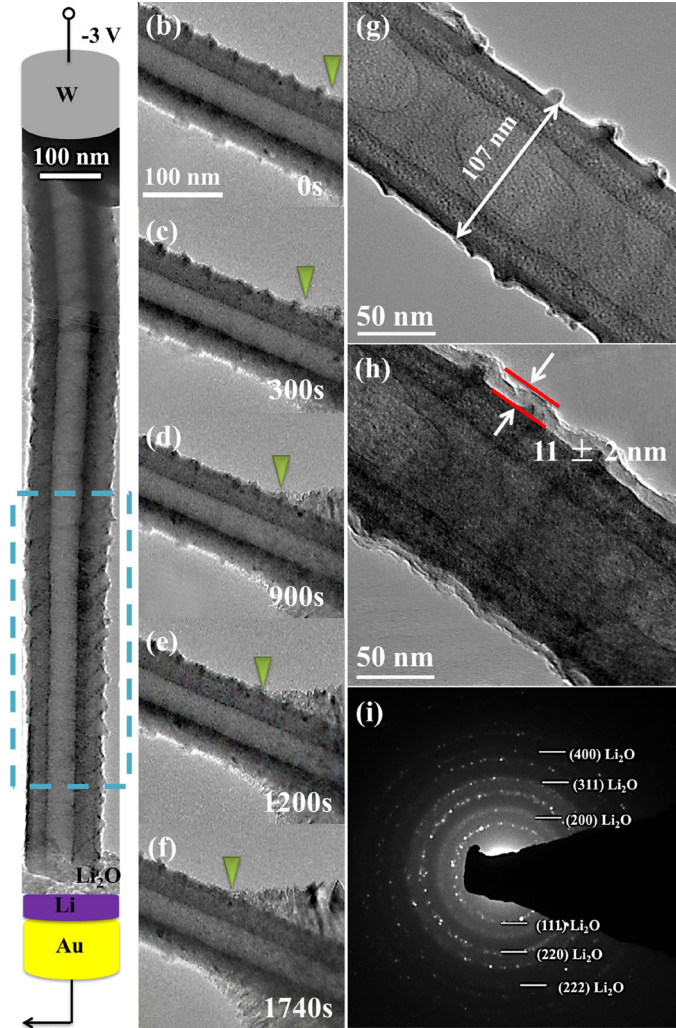


Figure 8.1 Serial snapshot images of lithiation process for an individual a-TNT. (a) The whole structural view of a selected a-TNT with diameter of around 130 nm. (b-f) A selected area of lithiation process monitored from the reference 0s (b) to 1740s (f). The evolution of Li₂O layer formation is observed on the surface of the nanotube as marked by green arrow. The HRTEM images of Li₂O layer formation on the surface of an individual a-TNT are shown as (g-i). (g) A pristine TiO₂ nanotube with diameter of 107 nm. (h) A thickness of 11±2 nm layer formation on the lithiated nanotube. (i) Corresponding diffraction pattern of the Li₂O layer.

In order to investigate the chemical signature change during lithiation, EELS was conducted on individual nanotubes. Figure 8.2(a) is a comparison of the EELS between the pristine and lithiated a-TNT. The Li *K* edge located at the energy loss position of 63.4 eV is similar to the ones in TiO₂ (rutile)²³⁴ and LiNiO₂²³⁵ via the same intercalation mechanism. Another rise of the Li *K* edge at 58.9 eV and 63.4 eV closely matches that of pure Li₂O, consistently supporting the observation of Li₂O formation on the surface of the nanotube upon lithiation.

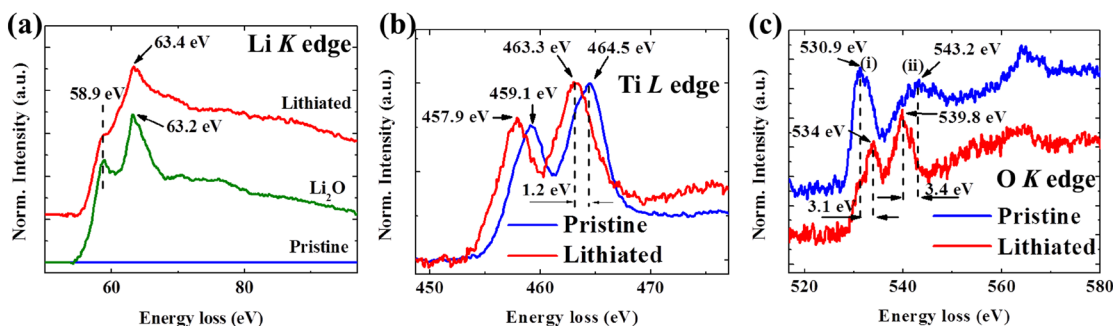
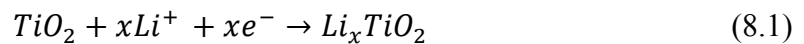


Figure 8.2 EELS spectra of Li *K* edge, Ti *L* edge and O *K* edge taken from the selected area of the nanotube before and after lithiation. (a) The EELS spectrums show Li *K* edge of pristine, lithiated TiO₂ nanotube, and Li₂O as a reference. (b) A comparison between Ti *L* edge in pristine and lithiated TiO₂ nanotubes is shown. (c) Showing O *K* edge in pristine and lithiated TiO₂ nanotubes.

Figure 8.2(b) shows the EELS of Ti *L* edge in a-TNTs before and after lithiation. In the pristine nanotube, the main feature is the 2*p* spin-orbit interaction splitting into the 2*p*_{3/2} (459.1 eV) and 2*p*_{1/2} (464.5 eV) levels with a separation of 5.4 eV.^{236, 237} The energy loss position of the peak is sensitive to the valence of Ti. After lithiation, these two

positions of energy loss shifted toward a low energy region, indicating the valence of Ti^{4+} reduce to Ti^{3+} to accommodate Li^+ intercalation, which is consistent with the observation from previous reports.^{238, 239} More evidence is provided by the O K edges between the pristine and lithiated nanotube in Figure 8.2(c). Prior to lithiation, the pre-edge peak **(i)** and main peak **(ii)** located on the energy loss position of 530.9 eV and 543.2 eV, respectively, corresponds to electron transition from $1s$ to oxygen $2p$ states hybridized with titanium $4s$ and $4p$ states.²³⁴ After lithiation, the energy loss position of pre-edge peak shifted 3.1 eV to high energy loss direction as compared with the pristine nanotube. The observed shifting in the O K edges towards the high energy is related to the reduction of the Ti ions following the insertion of Li into the lattice, indicating charge transfer from Li to Ti ions.²⁴⁰ Another significant feature in the lithiated nanotube was the decreasing of separation between the peaks **(i)** and **(ii)**. Yoshiya *et al.*²⁴⁰ had systematically studied the structure of TiO_x ($x < 2$). They noticed that with the decrease of the x value, the separation between peaks **(i)** and **(ii)** on the O K edges decreased, indicating the valence reduction of Ti upon Li ions intercalation. This conclusion is closely consistent with our experimental EELS results. In addition, one can notice that, after lithiation, the intensity of peak **(i)** became smaller than that of peak **(ii)**, which is due to Li_2O formation on the surface.²⁴¹

Our EELS observation is in a good agreement with the intercalation mechanism of Li ions into TiO_2 , which can be expressed as:²³



In the reaction, the insertion of positively charged Li^+ is balanced with an uptake of electrons to compensate Ti^{3+} cations in the Ti^{4+} sublattice. The maximum x after charging depends on the phase structure of TiO_2 (e.g. amorphous, anatase or rutile). The variation of x is also predicted by theoretical calculations,^{20, 24-29} and has been observed in X-ray photoelectron spectroscopy (XPS) experiments.^{30, 31} Recent studies²⁴²⁻²⁴⁴ on the use of TiO_2 (anatase and brookite- TiO_2) nanotube anodes in a lithium battery demonstrate an initial discharge capacity of 282 mAh/g at a specific current density of 0.24 mA/g in brookite, which corresponds to $x=0.98$ in Equation (8.1). For amorphous TiO_2 , associated with the disordered structures, no theoretical simulations and structural variation analysis by XRD have been conducted to calculate the x . However, the experimental results^{4, 245} show that the capacity performance of amorphous TiO_2 is better than that of anatase due to more sites and defects available for Li ions insertion in amorphous TiO_2 .

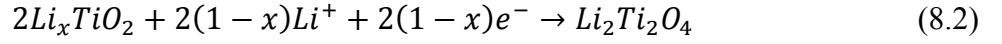
A close examination of the lithiated a-TNT walls indicated that the thickness of the wall increased from ~24 to ~26 nm, which corresponded to ~ 3.7% expansion in the radial direction of the nanotube as indicated in Figure 8.3(a & b). In fact, recent *ex situ* studies^{4, 245, 246} on a-TNTs reported a volume increase of less than 3% in fully charged TNTs compared with the non-charged ones. Due to the geometrical limitation of the *in situ* setup, it is very hard to directly measure the longitudinal elongation of the nanotube. However, based on the overall volume expansion calculation ($\frac{V_e}{V} = \frac{S_e}{S} \times \frac{l_e}{l} = \frac{d_e^2}{d^2} \times \frac{l_e}{l}$), one can notice that the volume expansion depends on the ratios of S_e/S and l_e/l . In our study, the ratio of S_e/S is only 0.0013, which indicates that the overall volume expansion for the TiO_2 nanotube can be within 3%.

expansion discussed earlier is mainly due to surface lithiation while no or little lithiation has happened in depth of the nanotube. This explanation is plausible considering the poor electrical conductivity of amorphous TiO_2 . Due to this limiting factor, Li ions cannot intercalate deep into the interior structure of the nanotube. Therefore, it is expected that the lithiation to be limited to the nanotube surface. This is mediated by the presence of Li_2O layer on the surface of TiO_2 nanotubes, which provides a convenient path for diffusion of Li ions.

The SAED pattern of the pristine nanotube shown in Figure 8.3(c) indicates an amorphous structure, as it would be expected. After lithiation, some particles with dark contrast appeared in the amorphous Li_xTiO_2 matrix as marked by white dotted circles in Figure 8.3(b). The corresponding SAED pattern shown in Figure 8.3(d) indicates that the lithiated a-TNT is dominated by crystalline $\text{Li}_2\text{Ti}_2\text{O}_4$ and Li_2O phases as evidenced by matching the experimental electron diffraction rings with the calculated pattern based on the $\text{Li}_2\text{Ti}_2\text{O}_4$ (Space group: $F\bar{m}3m$, Lattice constants: $a = b = c = 8.375 \text{ \AA}$)²⁴⁷ and Li_2O structure, respectively.

To better understand the nature of the dark contrast particles, HRTEM imaging was performed on the lithiated nanotube. Figure 8.4 shows HRTEM analysis of the particles at two different locations of the same lithiated nanotube. Figure 8.4(a) shows that some crystalline particles (marked by white arrows) are distributed almost randomly within the amorphous matrix. A closer view enables one to observe the lattice fringes in the particles, indicating the presence of atomic ordering in the amorphous matrix. The HRTEM image of one of the particles with the [001] zone axis is shown in Figure 8.4(c).

The HRTEM image shows the well-defined (400) crystal planes with the spacing of 2.09 Å, confirming the formation of crystalline $\text{Li}_2\text{Ti}_2\text{O}_4$ phase. Figure 8.4(d & e) confirms the presence of similar crystals at other locations in the amorphous matrix. Therefore, the Reaction (8.1) can be modified to include the new crystalline phase according to:



It is expected that the continuous lithiation of Li_xTiO_2 will lead to an atomic rearrangement in the amorphous Li_xTiO_2 matrix to form crystals of $\text{Li}_2\text{Ti}_2\text{O}_4$ with the $\text{Li}:\text{TiO}_2$ stoichiometry of 1. This is in agreement with the results of molecular dynamics simulations of Xiong *et al.*,²⁴⁸ where the formation of $\text{Li}_2\text{Ti}_2\text{O}_4$ in a-TNTs after lithiation was predicted. Their simulation results revealed that at high lithiation levels (>75%), the atomic diffusion of Ti and O became significant, suggesting facile rearrangement of atoms in the structure and leading to crystalline phase formation. They further reported that with increasing simulation time, the Ti, O, and Li atoms would present long-range order throughout the cubic structure.²⁴⁹

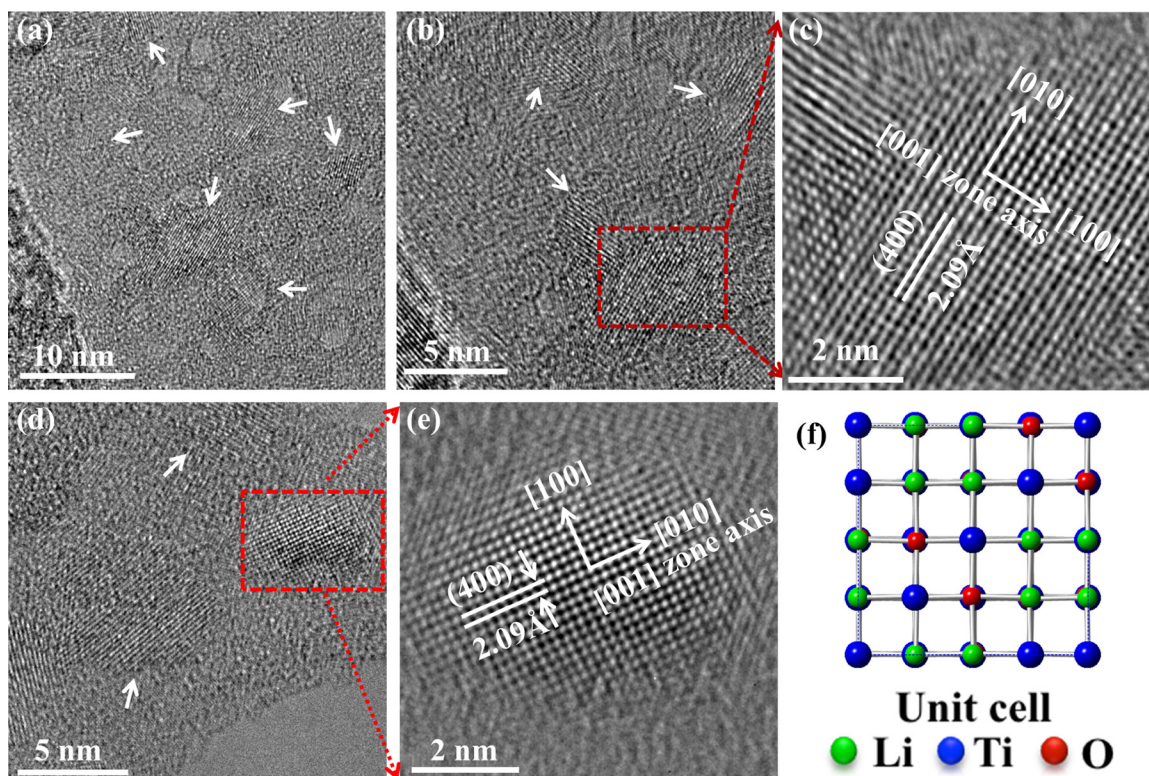


Figure 8.4 TEM images reveal the formation of $\text{Li}_2\text{Ti}_2\text{O}_4$ crystals within the amorphous matrix. (a) A zoom-out image of an area within lithiated amorphous TiO_2 where the presence of several crystalline particles are marked by white arrows. (b) A closer view of the crystalline particles shows the lattice fringes of crystalline particles. (c) High resolution TEM image of the particle marked by the red dotted box in (b) shows the atomic ordering within the crystalline particles. The particles are viewed along $[001]$ zone axis and the interatomic distance of 2.09 \AA was correlated to (400) planes in $\text{Li}_2\text{Ti}_2\text{O}_4$ crystals. (d-e) The existence of the crystalline particles within the lithiated amorphous matrix was also confirmed in other locations. (f) A unit cell of the $\text{Li}_2\text{Ti}_2\text{O}_4$ crystals viewed along $[001]$ zone axis.

The size of the crystalline islands shown in Figure 8.4(c & e) provides a characteristic length scale (~ 5 nm) at which the atomic bonding configuration has been changed within a short time period. One also could note that the crystalline particles are embedded within the amorphous matrix. This can be an indicative of inhomogeneous chemical changes in the amorphous matrix. More spectroscopy was conducted to capture the local chemical distributions before and after the amorphous to crystalline phase transition. Figure 8.5 compares the chemical distribution of a nanotube before and after lithiation by STEM-EELS elemental mapping. The EELS mapping was conducted on the same area as shown in Figure 8.5(a) and (e). The elemental mapping in Figure 8.5(b-d) and (f-h) indicates the chemical distribution of Ti and O elements is uniform before and after lithiation. However, the Li element mapping shown in Figure 8.5(i) demonstrates that the Li elements are distributed non-uniformly in the nanotube. For better clarity, all the maps related to Li, O, and Ti atoms are superimposed in Figure 8.5(j), which further indicates the local changes in the chemical composition. This is agreement with the simulation results¹⁶ that the Li would prefer the low energy locations as initial states in amorphous nanotubes, resulting in the high concentration of Li ions in some areas [Figure 8.5(j)]. The fluctuation of Li ions can promote the heterogeneous nucleation of $\text{Li}_2\text{Ti}_2\text{O}_4$ crystalline phase in the amorphous matrix, which is consistent with our HRTEM observation.

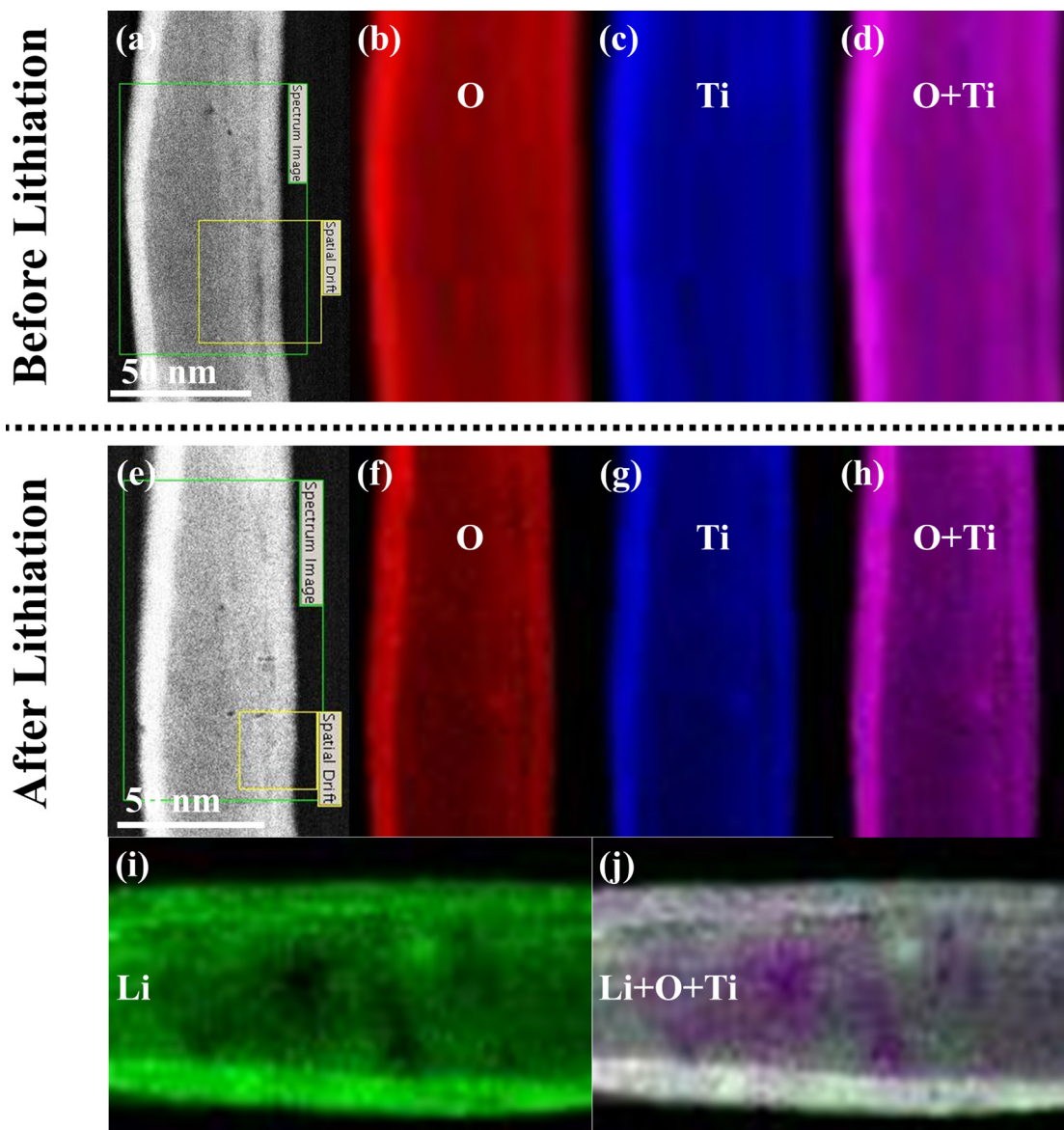


Figure 8.5 The STEM-EELS mapping of an individual a-TNT before and after lithiation shows the chemical distribution of Ti, O and Li in the nanotube. A selected area of EELS mapping shows the uniform distribution of O and Ti before lithiation (a-d) and after lithiation (e-h). (i) Li distribution by EELS mapping indicating the successful lithiation in the nanotube. (j) EELS mapping of Li, O, and Ti in the lithiated nanotube, showing the Li ions distributing randomly in the matrix.

The overall lithiation mechanism of the a-TNTs was captured in Figure 8.6(a) and schematically represented in Figure 8.6(b). Fully lithiated, partially lithiated, and unlithiated regions of the a-TNT are marked in Figure 8.6(a). In the fully lithiated region (Region I), a thick polycrystalline Li_2O layer (marked by white arrows) is formed on the surface of the nanotube and crystalline $\text{Li}_2\text{Ti}_2\text{O}_4$ islands are formed in the amorphous Li_xTiO_2 matrix (marked by yellow dotted circles). In Region II, only evidence of Li_2O layer can be found which indicates some lithiation of the matrix in the form of Li_xTiO_2 could have happened. The Li_2O layer on the surface (marked by black arrows) becomes thinner as it progresses toward the unlithiated region (Region III), which means that the lithiation proceeds through the Li_2O layer. No obvious crystalline islands were detected in Region II. In the unlithiated region (Region III), the nanotube is in amorphous state with no indication of lithiation.

On the basis of the results discussed above, a schematic design is proposed to illustrate the overall lithiation process of a-TNTs as shown in Figure 8.6(b). The Li ions will intercalate into the nanotube by donating electrons to Ti to form Li_xTiO_2 , associating a Li_2O layer formation on the surface of the nanotube. With increasing the concentration of Li ions in the nanotube, the diffusion of O and Ti atoms will also increase²⁴⁹ enabling the facile rearrangement of disordered atoms to $\text{Li}_2\text{Ti}_2\text{O}_4$ islands with crystalline structures.

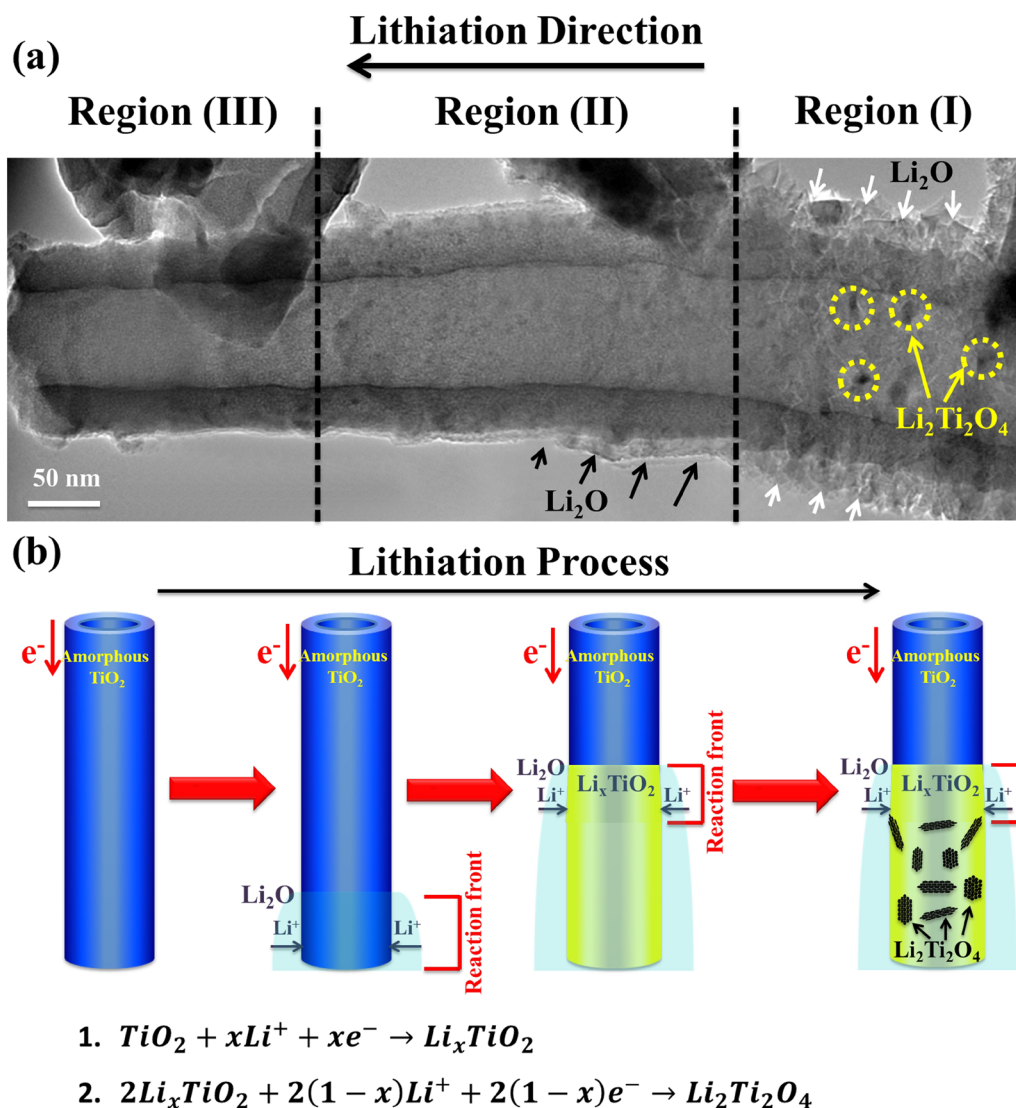


Figure 8.6 (a) Three distinctive regions are captured during lithiation of a single a-TNT. In region (I), the nanotube is fully lithiated as evident by the formation of polycrystalline Li_2O layer and crystalline $\text{Li}_2\text{Ti}_2\text{O}_4$ islands. In region (II), the nanotube is partially lithiated as evident by the progressive formation of Li_2O layer. No crystalline $\text{Li}_2\text{Ti}_2\text{O}_4$ islands could be detected. In region (III), the very end of the nanotube is still in pristine state (unlithiated). (b) The schematic graph shows various stages of lithiation process in a-TNTs.

8.4. Conclusion

In summary, the electrochemical lithiation mechanism of amorphous TiO_2 nanotubes was modified based on our *in situ* TEM observation. Initially, Li ions movements are facilitated by the surface diffusion through Li_2O layer at the surface of TiO_2 nanotubes. Through surface, Li ions intercalate into the nanotubes to form amorphous Li_xTiO_2 matrix. With the increase of Li ions concentration in the lithiated nanotube, the phase transformation from amorphous to crystalline by atomic rearrangement will happen. This leads to the formation of crystalline islands of $\text{Li}_2\text{Ti}_2\text{O}_4$ with cubic structure in the amorphous Li_xTiO_2 matrix. This phase transformation is associated with local inhomogeneities in Li distribution. In addition to the evidence of lithium-induced atomic ordering in amorphous TiO_2 materials, the present work provides a new reaction mechanism, supported by direct chemical and structural analyses, for the lithiation behavior of amorphous TiO_2 nanotubes.

Chapter 9 Conclusion

In the research project, morphological, mechanical, and electrical properties of TiO_2 nanotubes were studied. The collected results can be summarized as two parts. The first part relates to nanotubes synthesis and their morphological characterization. The second part focuses on the *in situ* TEM studies of mechanical, electrical and electrochemical testing.

The TiO_2 nanotubes were grown in NH_4F solution by electrochemical method. The anodization time and voltage were controlled to obtain desired aspect ratio of nanotubes. The relationship between anodization processing parameters with diameter and length of nanotubes was discussed in Chapter 3. The average diameter of nanotubes increased when the voltage increased. However, the anodization time did not have a substantial effect on the diameter of nanotubes. On the other hand, both anodization time and voltage could increase the length of nanotubes.

In further investigation, the structural instability of TiO_2 nanotubes was studied. TiO_2 nanotubes treated by Ammonium hydroxide (NH_4OH) solution exhibited abundant surface defects. By annealing at 500 °C, the nanotubes collapsed into nanoparticles, which demonstrated the instability of nanotubes. As opposed to the common belief that the transformation to rutile is the major reason for the collapse of the anatase nanotubes, it was determined that volumetric change due to phase transformation (amorphous→anatase) and surface roughness weakening due to chemical etching had the key role during the collapse of NH_4OH -treated TiO_2 nanotubes.

A new method was developed to transform anatase TiO_2 to rutile phase by *in situ* Joule heating in TEM. The results revealed that anatase nanotubes under Joule heating dissociated to small particles ($\sim 10\text{--}20$ nm) of anatase at low bias voltage (≤ 10 V). At an intermediate bias range, between 10 and 20 V, the anatase nanoparticles transformed to rutile phase. Under the bias heating condition with 30 V, the rutile particles agglomerate into large particles with sizes ranging up to 200 nm.

In situ electrical transport measurements on both amorphous and anatase TiO_2 nanotubes were successfully carried out inside a high-resolution TEM equipped with a STM probe. The results revealed that the electrical properties of TiO_2 nanotubes (either amorphous or anatase) could be enhanced by mechanical bending deformation. The semiconducting parameters were retrieved from the experimental I - V curves using the M - S - M model. The I - V curves shown, in Chapter 6 and 7, demonstrated that with increasing bending angle, the conductivity would increase.

Electrochemical lithiation measurement of individual TiO_2 nanotubes was conducted in TEM. Pure Li metal was used as cathode, Li_2O functioned as solid electrolyte, and TiO_2 nanotubes were used as anode material. The results show that, initially, Li ions movements are facilitated by the surface diffusion through Li_2O layer at the surface of TiO_2 nanotubes. Through surface, Li ions intercalate into the nanotubes to form amorphous Li_xTiO_2 matrix. With the increase of Li ions concentration in the lithiated nanotube, the phase transformation from amorphous to crystalline by atomic rearrangement will happen. This leads to the formation of crystalline islands of $\text{Li}_2\text{Ti}_2\text{O}_4$ with cubic structure in the amorphous Li_xTiO_2 matrix. This phase transformation is

associated with local inhomogeneities in Li distribution. In addition to the evidence of lithium-induced atomic ordering in amorphous TiO_2 materials, the present work provides a new reaction mechanism, supported by direct chemical and structural analyses, for the lithiation behavior of amorphous TiO_2 nanotubes.

Chapter 10 Future Work

This PhD project mainly focused on the electrochemical characterization for TiO₂ nanotubes as well as the mechanical and electrical properties investigation by *in situ* TEM. However, the study was not fully researched in every aspect and still left a lot to be explored. In further research, there are three major projects for extensive study and investigation.

10.1. *In Situ* Electrochemistry of Anatase TiO₂ Nanotubes

The crystalline anatase [Figure 10.1(a)], one of the natural TiO₂ polymorphs, has been studied a lot for the application of optical devices,²⁵⁰ solar industry^{90, 251} and Li ion batteries²⁵² due to the properties of readily available, chemically stable, inexpensive, and nontoxic.²⁵³ The anatase TiO₂ especially attracts interest for Li-rechargeable batteries because of the ability to store significant amounts of Li. The overall lithium intercalation mechanism can be expressed in Equation (10.1):²⁵⁴



The x varies from 0 to 0.7, and the most stable phase is $x = 0.5$, which has been shown in the phase diagram. In the insertion process, the Li atoms occupy the octahedral sites in the anatase lattice.²⁵⁵⁻²⁵⁷ At low concentration ($x < 0.05$), the Li atoms randomly distribute in the octahedral sites and the anatase still holds the tetragonal structures, known as Li-poor phase.²⁵⁸ With the further Li insertion of $0.05 < x < 0.5$, the tetragonal structure will distort to orthorhombic to create more octahedral sites to hold Li atoms,

known as Li-rich phase.^{255, 258} Coexistence of these of phase has been observed in the electrochemical cycling²⁵⁹ shown in Figure 10.1(b) and 1(c). The plateaus in the charge/discharge indicate the equilibrium transformation between Li-poor and Li-rich. The capacity decreases from 290 mAh·g⁻¹ to 229 mAh·g⁻¹ after three cycles due to the irreversible capacity loss. The coulomb efficiency is 0.8 initially and increases to 1 after several cycles, indicating the excellent reversibility during electrochemical cycling.

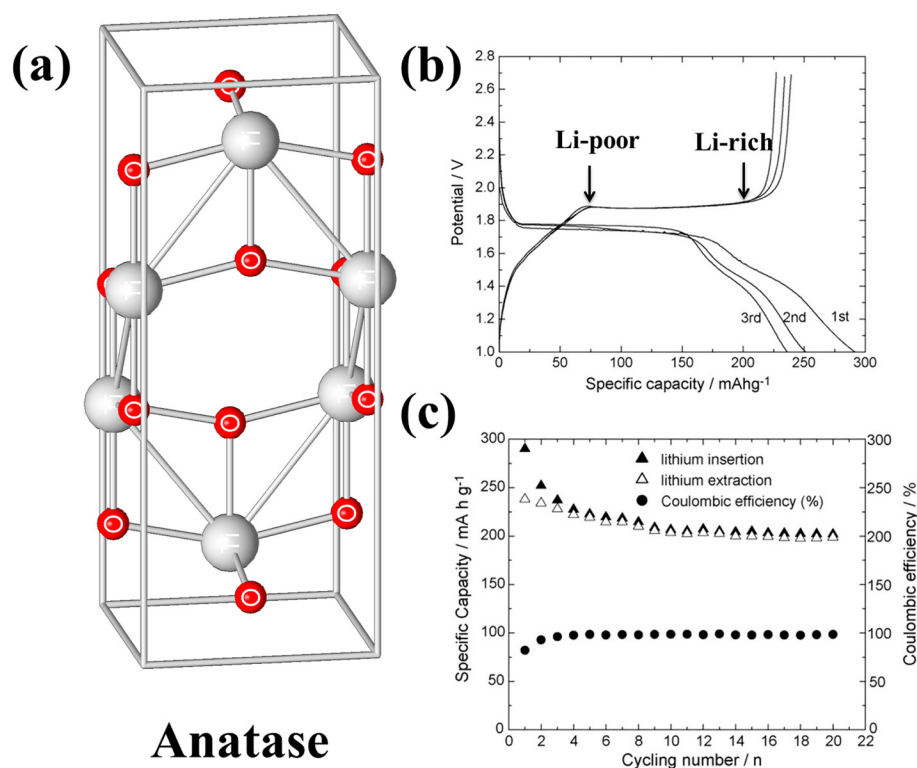


Figure 10.1 (a) unit cell of anatase, (b) initial three charge/discharge curves of anatase TiO₂ nanotubes,²⁵⁹ (c) capacity and coulomb efficiency of anatase TiO₂ nanotubes versus cycling numbers.²⁵⁹ (Reprint with the permission from *Electrochimica Acta*, 2007, 52, 8044-8047. Copyright, 2007, Elsevier)

The anatase TiO₂ nanotubes can be obtained by heating the amorphous nanotubes in the atmosphere under the temperature of 400 °C as discussed in the Chapter 4. The *in situ* electrochemical testing of anatase TiO₂ nanotubes can be exactly the same as amorphous nanotubes since the morphology of nanotubes after heating does not change. The anatase TiO₂ has low band gap of 3.2 eV,¹⁷ which is smaller than that of amorphous, exhibiting better electrical behavior in the test. Due to this behavior, one can expect fast lithiation process and good electrical conductivity in the lithiation process. The lithium ions will be inserted into the octahedral sites of the anatase structures and cause uniform and small volume expansion since the insertion ratio x is around 0.5. This will still hold the tetragonal structure. Comparing with amorphous structures that form crystalline Li₂Ti₂O₄, the anatase will be expected to still maintain its tetragonal structure and no new/intermediate phase forms during lithiation. Because when the insertion ratio $x > 0.5$, there are not available octahedral sites to accommodate Li ions and the Li ions will repulse each other. Therefore, it is difficult to obtain Li:TiO₂ of stoichiometry 1.

10.2. *In Situ* Electrochemistry of TiO₂ (B) Nanostructures

TiO₂ (B), a monoclinic structure, has recently attracted much interest as anode materials in Li ion batteries due to its unique crystal structures. Compared to other TiO₂ polymorphs (amorphous, anatase, and rutile), TiO₂ (B) exhibits a higher specific capacity due to the low density crystal structure and the perovskite-like layered structure.^{260, 261} The bulk TiO₂ (B) can store 240 mAh·g⁻¹, however, the nanostructured TiO₂ (B) can boost the capacity to 305 mAh·g⁻¹ in nanowire form and 330 mAh·g⁻¹ for nanotubes, corresponding to Li_{0.98}TiO₂.²⁶²⁻²⁶⁵

The lithium ions can sit in three available sites in the TiO_2 (B) crystals: A1 and A2 sites, which are near equatorial and axial oxygens in the octahedral, respectively and C sites, which are in the open channel along the b -axis²⁶¹ as shown in Figure 10.2. In low concentration ($x < 0.25$), the C sites are the most favorable ones for lithium insertion. When the concentration increases ($0.25 < x < 0.5$), the C sites become unfavorable and A1 sites are all occupied. At $x = 1$, both A1 and A2 sites are fully taken.²⁶⁶

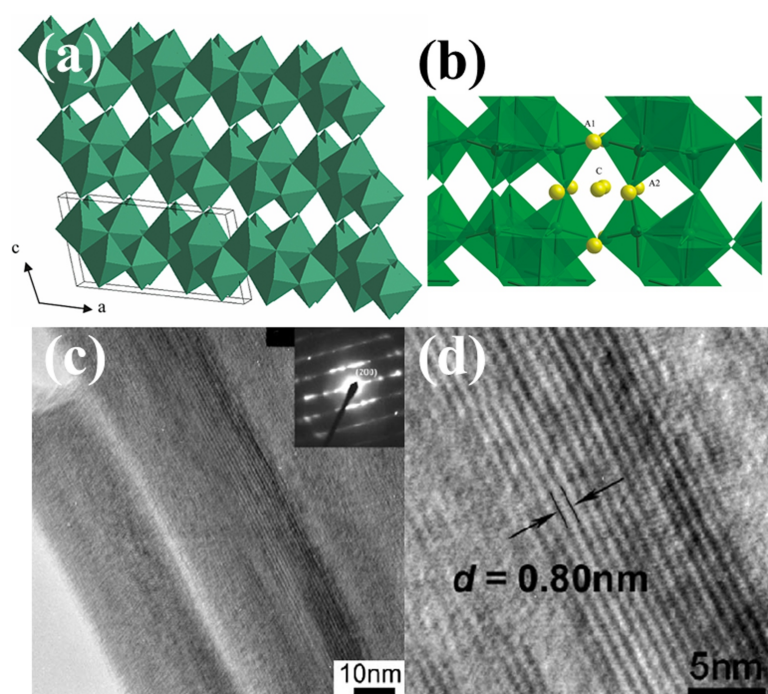


Figure 10.2 TiO_2 (B) crystal structure (a) TiO_6 octahedral unit cell, (b) lithium intercalation sites in the unit cell: A1, A2, and C,²⁶⁶ (c-d) HRTEM images with corresponding diffraction pattern of TiO_2 (B) nanofibers.²⁶⁷ (Reprint with the permission from Chemistry of Materials, 2010, 22, 6426-6432. Copyright, 2010, American Chemical Society; Journal of Solid State Chemistry, 2005, 178, 3110-3116. Copyright, 2005, Elsevier)

The *ex situ* electrochemical cycling performance of TiO_2 (B) nanosheets is illustrated in Figure 10.3. The charge/discharge curves under various rates are shown in Figure 10.3(a). One can notice that the capacity is controlled by charge/discharge rate. In addition, the cycling retention in Figure 10.3(b) shows the excellent cycling retention for TiO_2 (B). Aravindan *et al.* reported that the cycling number of TiO_2 (B) nanorods can be up to 500 cycles without or little capacity loss and the coulomb efficiency can maintain over 99.5%, demonstrating the excellent reversibility during electrochemical cycling.²⁶⁸ No study has been reported the electrochemical testing by *in situ* TEM and it is necessary to reveal the structural evolution of TiO_2 (B) in real time during lithiation process. The TiO_2 (B) can be synthesized in various nanostructures: nanowires, nanotubes, nanoparticles, and nanosheets.^{263, 269-271} The real time observation in TEM can help to study the structural changing in the lithiation process, especially for TiO_2 (B), which has an anisotropic volume expansion.²⁶⁶ The SAED can identify the monoclinic structures of TiO_2 (B) and the HRTEM images in the atomic-scale should be used to capture the positions of lithium ions.

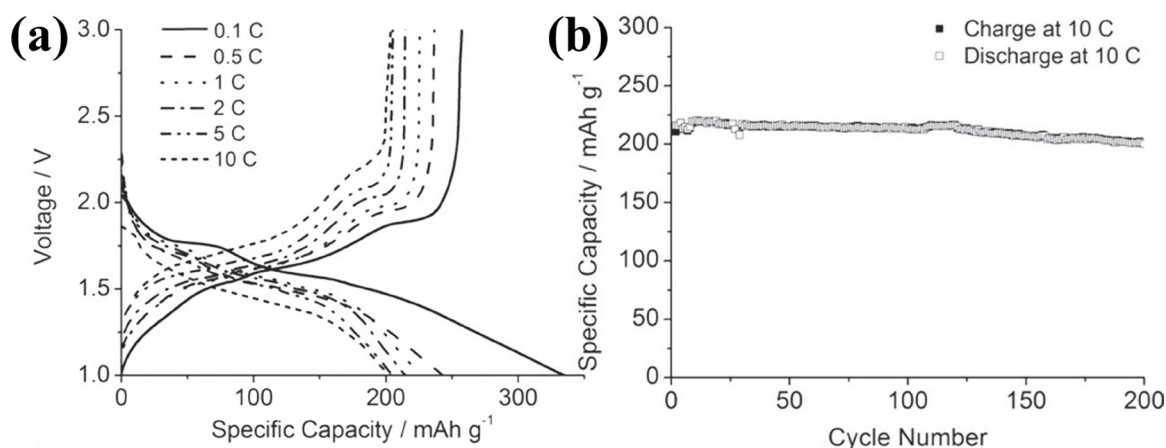


Figure 10.3 (a) charge/discharge curves of TiO₂ (B) nanosheets under various rates, (b) cycling performance of TiO₂ (B) nanosheets.²⁷⁰ (Reprint with the permission from Advanced Materials, 2012, 24, 3201-3204. Copyright, 2012, John Wiley and Sons)

10.3. *In situ* Electrochemistry of Rutile TiO₂ Nanostructures

Rutile, a tetragonal crystalline structure [Figure 10.4(a)], is also one of the favorable TiO₂ polymorphs as anode materials.^{272, 273} The rutile TiO₂ is the most thermal structure in room temperature and can be synthesized by simple sputtering and annealing methods.²⁷⁴ Nanostructured rutile TiO₂ shows high capacity and better lithium electrochemical activity.²⁷⁵

The lithium insertion into rutile TiO₂ is complicated, which involves several structural evolutions comparing with other polymorphs (amorphous, anatase, and B type). Baudrin *et al.*²⁷⁶ reported the formation of LiTiO₂ with rocksalt structure when lithium ions insert into nanostructured rutile. Another study by Koudriachova *et al.*²⁷⁷ revealed the formation of hexagonal structure upon the lithium insertion into rutile TiO₂ via first principles calculations. However, Borghols *et al.*²⁷⁸ reported that, for a lithium

concentration of $x = 0.85$, the rutile structure transforms to a monoclinic structure by resembling the hexagonal structure. Besides those final phases, intermediate phases are also expected to be observed during lithiation. Two possible structures have been studied for $\text{Li}_{0.5}\text{TiO}_2$: a distorted monoclinic structure²⁷⁸ and a cubic spinel structure.²⁴⁷

The electrochemical cycling performance of rutile TiO_2 is illustrated in Figure 10.4(e) and 4(f). Among various size of rutile TiO_2 during cycling, the nanosized rutile exhibits a much better reversible discharge capacity of $280 \text{ mAh} \cdot \text{g}^{-1}$, corresponding to the high insertion ratio $x = 0.8$ than other size TiO_2 . One significant feature in Figure 10.4(e) is the multiple plateaus in the discharge curve (marked by arrows), indicating various intermediate phases in the rutile during lithiation. The accurate results relating to the phases are still in discussion. The electrochemical cycling performance [Figure 10.4(f)] shows excellent cycling retention of nanosized rutile TiO_2 under various charge/discharge rates, illustrating the good reversibility for the lithium ions insertion and extraction. Pfanzelt *et al.* recently reported that the nanosized rutile TiO_2 can be cycled up to 1000 cycles without or little capacity loss and the coulomb efficiency is around 99.9%.²⁷⁹

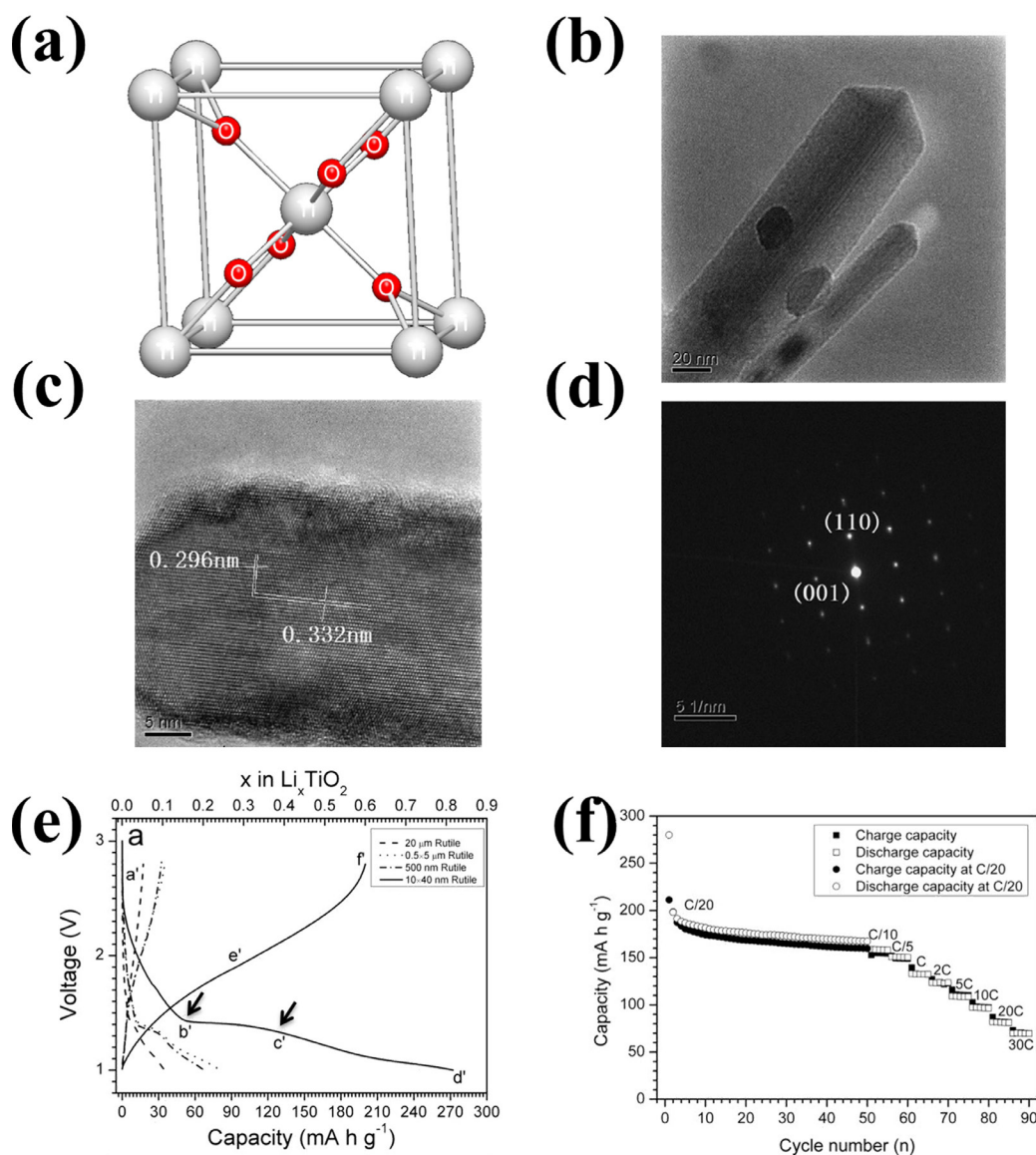


Figure 10.4 (a) The unit cell of rutile TiO_2 , (b-d) HRTEM image of rutile nanorods with corresponding diffraction pattern,²⁸⁰ (e) the charge/discharge curves of various sized rutile TiO_2 ,²⁷⁵ (f) electrochemical cycling of nanosized rutile TiO_2 under various rate.²⁷⁵ (Reprint with the permission from Journal of Crystal Growth, 2007, 306, 117-122. Copyright, 2007, Elsevier; Advanced Materials, 2006, 18, 1421-1426. Copyright, 2006, John Wiley and Sons)

It is necessary to use *in situ* TEM technique to observe and reveal the structural evolutions for the lithiation of rutile TiO₂. The most advantage of *in situ* TEM is to observe the structural evolution in atomic scale. Since many phases may appear in the lithiation process, it is recommended to monitor the structure and diffraction pattern every several minutes. The best way to reveal the systematical lithiation mechanism of rutile TiO₂ is to do *in situ* SAED lithiation, which could easily help to observe the crystalline structures in real time.

In summary, rutile has better electrochemical cycling performance than TiO₂ (B). Rutile has larger capacity ($x \approx 1$) because of the intermediate phases (tetragonal, spinel, and rock salt) in rutile upon lithium insertion. The lithium ions initially insert in the off-centered octahedral sites. With $x \sim 0.5$, the lithium ions reside the tetrahedral positions to form spinel structure (Li_{0.44}TiO₂). When $x > 0.9$, the lithium ions in tetrahedral holes of spinel structures are displaced to octahedral environments leading to rock salt structure. The phase transformation can help rutile to accommodate lithium ions insertion. Moreover, rutile has excellent cycling retention and can be cycled to 1000 cycles without or little capacity loss. In addition, rutile is the most thermal stable one among TiO₂ polymorphs, which is one of the most important features to be considered in lithium ion batteries for safety issues.

Compared to anatase, TiO₂ (B) shows better electrochemical behavior during cycling. Both anatase and TiO₂ (B) are thermally stable up to the temperatures of ~ 600 °C. However, the Li storage and cycling retention exhibit significant differences. The normal Li storage ratio in anatase is $x = 0.5$. When x increases, the Li ions will repulse each other

and no more octahedral sites are available for insertion. In TiO_2 (B), three available sites of A1, A2, and C can accommodate various concentration of Li ions to reside, which can help get a theoretical capacity of $\sim 420 \text{ mAh} \cdot \text{g}^{-1}$ ($x = 1.25$).²⁶⁰ Both anatase and TiO_2 (B) have good cycling retention. The anatase TiO_2 have been charged/discharged up to 200 cycles with negligible capacity loss. For TiO_2 (B), 500 cycles have been reported while retaining high coulomb efficiency. Overall, it is apparent that TiO_2 (B) is a better choice as anode in Li ion batteries in comparison to anatase phase.

References

1. Tarascon, J. M. and Armand, M., "Issues and challenges facing rechargeable lithium batteries", *Nature*, **2001**, 414, 359-367
2. Nagaura, T. and Tozawa, K., "Lithium ion rechargeable battery", *Prog. Batteries Solar Cells*, **1990**, 9, 209
3. Ballon, M. S., "Electrovaya,Tata Motors to make electric Indica", *Cleantech.com*, **2008**,
4. Ortiz, G. F.; Hanzu, I.; Djenizian, T.; Lavela, P.; Tirado, J. L. and Knauth, P., "Alternative Li-Ion Battery Electrode Based on Self-Organized Titania Nanotubes", *Chem. Mater.*, **2009**, 21, 63-67
5. Laïk, B.; Eude, L.; Pereira-Ramos, J.-P.; Cojocaru, C. S.; Pribat, D. and Rouvière, E., "Silicon nanowires as negative electrode for lithium-ion microbatteries", *Electrochim. Acta*, **2008**, 53, 5528-5532
6. Park, M.-H.; Cho, Y.; Kim, K.; Kim, J.; Liu, M. and Cho, J., "Germanium Nanotubes Prepared by Using the Kirkendall Effect as Anodes for High-Rate Lithium Batteries", *Angew. Chem. Int. Ed.*, **2011**, 50, 9647-9650
7. Hamon, Y.; Brousse, T.; Jousse, F.; Topart, P.; Buvat, P. and Schleich, D. M., "Aluminum negative electrode in lithium ion batteries", *J. Power Sources*, **2001**, 97–98, 185-187
8. Wang, C.; Appleby, A. J. and Little, F. E., "Electrochemical study of the SnO₂ lithium-insertion anode using microperturbation techniques", *Solid State Ionics*, **2002**, 147, 13-22

9. Song-Lin, S.; Yong-Gang, L.; Jing-Yuan, Z. and Tai-Hong, W., "Electrochemical properties of SnO₂ nanorods as anode materials in lithium-ion battery", *Chinese Physics B*, **2009**, 18, 4564
10. Ju, S.; Lee, K.; Janes, D. B.; Yoon, M.-H.; Facchetti, A. and Marks, T. J., "Low Operating Voltage Single ZnO Nanowire Field-Effect Transistors Enabled by Self-Assembled Organic Gate Nanodielectrics", *Nano Lett.*, **2005**, 5, 2281-2286
11. Yuan, Z. Y. and Su, B. L., "Titanium Oxide Nanotubes, Nanofibers and Nanowires", *Colloids Surf., A: Physicochem. Engi. Aspe.*, **2004**, 241, 173-183
12. Wagemaker, M.; Kearley, G. J.; van Well, A. A.; Mutka, H. and Mulder, F. M., "Multiple Li positions inside oxygen octahedra in lithiated TiO₂ anatase", *J. Am. Chem. Soc.*, **2003**, 125, 840-848
13. Armstrong, A. R.; Armstrong, G.; Canales, J. and Bruce, P. G., "TiO₂-B nanowires as negative electrodes for rechargeable lithium batteries", *J. Power Sources*, **2005**, 146, 501-506
14. Jin, B.; Gu, H.-B. and Kim, K.-W., "Effect of different conductive additives on charge/discharge properties of LiCoPO₄/Li batteries", *J. Solid State Electrochem.*, **2008**, 12, 105-111
15. Strobel, P.; Tillier, J.; Diaz, A.; Ibarra-Palos, A.; Thiéry, F. and Soupart, J. B., "Search for new manganese-cobalt oxides as positive electrode materials for lithium batteries", *J. Power Sources*, **2007**, 174, 910-915
16. Yildirim, H.; Greeley, J. and Sankaranarayanan, S. K. R. S., "Effect of Concentration on the Energetics and Dynamics of Li Ion Transport in Anatase and Amorphous TiO₂", *J. Phys. Chem. C*, **2011**, 115, 15661-15673

17. Eufinger, K.; Poelman, D.; Poelman, H.; De Gryse, R. and Marin, G. B., "Photocatalytic activity of dc magnetron sputter deposited amorphous TiO₂ thin films", *Appl. Surf. Sci.*, **2007**, 254, 148-152
18. Varghese, O. K.; Gong, D.; Paulose, M.; Grimes, C. A. and Dickey, E. C., "Crystallization and high-temperature structural stability of titanium oxide nanotube arrays", *J. Mater. Res.*, **2003**, 18, 156-165
19. Crawford, G. A.; Chawla, N.; Das, K.; Bose, S. and Bandyopadhyay, A., "Microstructure and deformation behavior of biocompatible TiO₂ nanotubes on titanium substrate", *Acta Biomaterialia*, **2007**, 3, 359-367
20. Muscat, J.; Swamy, V. and Harrison, N. M., "First-principles calculations of the phase stability of TiO₂", *Physical Review B*, **2002**, 65, 224112
21. Tang, H.; Prasad, K.; Sanjines, R.; Schmid, P. E. and Levy, F., "Electrical and optical properties of TiO₂ anatase thin films", *J. Appl. Phys.*, **1994**, 75, 2042-2047
22. Tang, H.; Berger, H.; Schmid, P. E.; Lévy, F. and Burri, G., "Photoluminescence in TiO₂ anatase single crystals", *Solid State Commun.*, **1993**, 87, 847-850
23. Van De Krol, R.; Goossens, A. and Schoonman, J., "Spatial Extent of Lithium Intercalation in Anatase TiO₂", *J. Phys. Chem. B*, **1999**, 103, 7151-7159
24. Olson, C. L.; Nelson, J. and Islam, M. S., "Defect Chemistry, Surface Structures, and Lithium Insertion in Anatase TiO₂", *J. Phys. Chem. B*, **2006**, 110, 9995-10001
25. Stashans, A.; Lunell, S.; Bergstroem, R.; Hagfeldt, A. and Lindquist, S.-E., "Theoretical study of lithium intercalation in rutile and anatase", *Phys. Rev. B: Condens. Matter.*, **1996**, 53, 159
26. Mackrodt, W. C., "First Principles Hartree–Fock Description of Lithium Insertion

- in Oxides: I. The End Members TiO_2 and LiTiO_2 of the System Li_xTiO_2 ", *J. Solid State Chem.*, **1999**, 142, 428-439
27. Koudriachova, M. V.; de Leeuw, S. W. and Harrison, N. M., "Orthorhombic distortion on Li intercalation in anatase", *Phys. Rev. B*, **2004**, 69, 054106
 28. Koudriachova, M. V.; de Leeuw, S. W. and Harrison, N. M., "First-principles study of H intercalation in rutile TiO_2 ", *Physical Review B*, **2004**, 70, 165421
 29. Koudriachova, M. V.; Harrison, N. M. and de Leeuw, S. W., "Density-functional simulations of lithium intercalation in rutile", *Phys. Rev. B: Condens. Matter.*, **2002**, 65, 235423
 30. Södergren, S.; Siegbahn, H.; Rensmo, H.; Lindström, H.; Hagfeldt, A. and Lindquist, S.-E., "Lithium Intercalation in Nanoporous Anatase TiO_2 Studied with XPS", *J. Phys. Chem. B*, **1997**, 101, 3087-3090
 31. Henningsson, A.; Rensmo, H.; Sandell, A.; Siegbahn, H.; Sodergren, S.; Lindstrom, H. and Hagfeldt, A., "Electronic structure of electrochemically Li-inserted TiO_2 studied with synchrotron radiation electron spectroscopies", *J.Chem.Phys.*, **2003**, 118, 5607-5612
 32. Fang, H. T.; Liu, M.; Wang, D. W.; Sun, T.; Guan, D. S.; Li, F.; Zhou, J.; Sham, T. K. and Cheng, H. M., "Comparison of the rate capability of nanostructured amorphous and anatase TiO_2 for lithium insertion using anodic TiO_2 nanotube arrays", *Nanotechnology*, **2009**, 20, 225701
 33. Gong, D.; Grimes, C. A.; Varghese, O. K.; Hu, W.; Singh, R. S.; Chen, Z. and Dickey, E. C., "Titanium Oxide Nanotube Arrays Prepared by Anodic Oxidation", *J. Mater. Res.*, **2001**, 16, 3331

34. Zhao, J.; Wang, X.; Chen, R. and Li, L., "Fabrication of Titanium Oxide Nanotube Arrays by Anodic Oxidation", *Solid State Commun.*, **2005**, 134, 705-710
35. Prakasam, H. E.; Shankar, K.; Paulose, M.; Varghese, O. K. and Grimes, C. A., "A New Benchmark for TiO₂ Nanotube Array Growth by Anodization", *J. Phys. Chem. C*, **2007**, 111, 7235-7241
36. Shankar, K.; Mor, G. K.; Fitzgerald, A. and Grimes, C. A., "Cation Effect on the Electrochemical Formation of Very High Aspect Ratio TiO₂ Nanotube Arrays in Formamide-Water Mixtures", *J. Phys. Chem. C*, **2007**, 111, 21-26
37. Yoriya, S.; Paulose, M.; Varghese, O. K.; Mor, G. K. and Grimes, C. A., "Fabrication of Vertically Oriented TiO₂ Nanotube Arrays Using Dimethyl Sulfoxide Electrolytes", *J. Phys. Chem. C*, **2007**, 111, 13770-13776
38. Choi, J.; Wehrspohn, R. B.; Lee, J. and Gosele, U., "Anodization of Nanoimprinted Titanium: A Comparison with Formation of Porous Alumina", *Electrochim. Acta*, **2004**, 49, 2645-2652
39. Chu, R.; Yan, J.; Lian, S.; Wang, Y.; Yan, F. and Chen, D., "Shape-Controlled Synthesis of Nanocrystalline Titania at Low Temperature", *Solid State Commun.*, **2004**, 130, 789-792
40. Song, Y.-Y.; Schmidt-Stein, F.; Bauer, S. and Schmuki, P., "Amphiphilic TiO₂ Nanotube Arrays: An Actively Controllable Drug Delivery System", *J. Am. Chem. Soc.*, **2009**, 131, 4230-4232
41. Yu, W.; Zhang, Y.; Xu, L.; Sun, S.; Jiang, X. and Zhang, F., "Microarray-Based Bioinformatics Analysis of Osteoblasts on TiO₂ Nanotube Layers", *Colloids Surf.*,

B: Biointerfaces, **2012**, 93, 135-142

42. Cao, X.; Yu, W.-q.; Qiu, J.; Zhao, Y.-f.; Zhang, Y.-l. and Zhang, F.-q., "RGD Peptide Immobilized on TiO₂ Nanotubes for Increased Bone Marrow Stromal Cells Adhesion and Osteogenic Gene Expression", *J. Mater. Sci.: Mater. Med.*, **2012**, 23, 527-536
43. Chen, J.; Zhou, H.; Santulli, A. C. and Wong, S. S., "Evaluating Cytotoxicity and Cellular Uptake from the Presence of Various Processed TiO₂ Nanostructured Morphologies", *Chem. Res. Toxicol.*, **2010**, 23, 871-879
44. Kobayashi, S.; Hamasaki, N.; Suzuki, M.; Kimura, M.; Shirai, H. and Hanabusa, K., "Preparation of Helical Transition-Metal Oxide Tubes Using Organogelators as Structure-Directing Agents", *J. Am. Chem. Soc.*, **2002**, 124, 6550-6551
45. Guo, Y. G.; Hu, J. S.; Liang, H. P.; Wan, L. J. and Bai, C. L., "TiO₂-Based Composite Nanotube Arrays Prepared via Layer-by-Layer Assembly", *Adv. Funct. Mater.*, **2005**, 15, 196-202
46. Kasuga, T.; Hiramatsu, M.; Hoson, A.; Sekino, T. and Niihara, K., "Formation of Titanium Oxide Nanotube", *Langmuir*, **1998**, 14, 3160-3163
47. Cai, Q. Y.; Paulose, M.; Varghese, O. K. and Grimes, C. A., "The Effect of Electrolyte Composition on the Fabrication of Self-Organized Titanium Oxide Nanotube Arrays by Anodic Oxidation", *J. Mater. Res.*, **2005**, 20, 230-236
48. Lai, Y. K.; Sun, L.; Chen, C.; Nie, C. G.; Zuo, J. and Lin, C. J., "Optical and electrical characterization of TiO₂ nanotube arrays on titanium substrate", *Appl. Surf. Sci.*, **2005**, 252, 1101-1106
49. Xiao, X.; Ouyang, K.; Liu, R. and Liang, J., "Anatase Type Titania Nanotube

- Arrays Direct Fabricated by Anodization without Annealing", *Appl. Surf. Sci.*, **2009**, 255, 3659-3663
50. Paulose, M.; Shankar, K.; Yoriya, S.; Prakasam, H. E.; Varghese, O. K.; Mor, G. K.; Latempa, T. A.; Fitzgerald, A. and Grimes, C. A., "Anodic Growth of Highly Ordered TiO₂ Nanotube Arrays to 134 μ m in Length", *J. Phys. Chem. B*, **2006**, 110, 16179-16184
 51. Macak, J. M.; Hildebrand, H.; Marten-Jahns, U. and Schmuki, P., "Mechanistic Aspects and Growth of Large Diameter Self-Organized TiO₂ Nanotubes", *J. Electroanal. Chem.*, **2008**, 621, 254-266
 52. Lin, C.; Chen, S. and Cao, L., "Anodic Formation of Aligned and Bamboo-Type TiO₂ Nanotubes at Constant Low Voltages", *Mater. Sci. Semicond. Process.*, **2013**, 16, 154-159
 53. Wang, D.; Zhou, F.; Liu, Y. and Liu, W., "Synthesis and Characterization of Anatase TiO₂ Nanotubes with Uniform Diameter from Titanium Powder", *Mater. Lett.*, **2008**, 62, 1819-1822
 54. Suzuki, Y. and Yoshikawa, S., "Synthesis and Thermal Analyses of TiO₂-Derived Nanotubes Prepared by the Hydrothermal Method", *J. Mater. Res.*, **2004**, 19, 982
 55. Zhang, M.; Bando, Y. and Wada, K., "Sol-Gel Template Preparation of TiO₂ Nanotubes and Nanorods", *J. Mater. Sci. Lett.*, **2001**, 20, 167-170
 56. Qiu, J. J.; Yu, W. D.; Gao, X. D. and Li, X. M., "Sol-Gel Assisted ZnO Nanorod Array Template to Synthesize TiO₂ Nanotube Arrays", *Nanotechnology*, **2006**, 17, 4695
 57. Huang, S.; Peng, W.; Ning, C.; Hu, Q. and Dong, H., "Nanostructure Transition

- on Anodic Titanium: Structure Control via a Competition Strategy between Electrochemical Oxidation and Chemical Etching", *J. Phys. Chem. C*, **2012**, 116, 22359-22364
58. Macak, J. M. and Schmuki, P., "Anodic Growth of Self-Organized Anodic TiO₂ Nanotubes in Viscous Electrolytes", *Electrochim. Acta*, **2006**, 52, 1258-1264
 59. Dumitriu, C.; Pirvu, C. and Demetrescu, I., "The Electrochemical Formation and Shielding Mechanism of TiO₂ Nanotubes in Organic Electrolytes with Different Viscosity", *J. Electrochem. Soc.*, **2013**, 160, G55-G60
 60. Yoriya, S.; Prakasam, H. E.; Varghese, O. K.; Shankar, K.; Paulose, M.; Mor, G. K.; Latempa, T. J. and Grimes, C. A., "Initial Studies on the Hydrogen Gas Sensing Properties of Highly-Ordered High Aspect Ratio TiO₂ Nanotube-Arrays 20 μ m to 222 μ m in Length", *Sens. Lett.*, **2006**, 4, 334-339
 61. Ya, J.; An, L.; Liu, Z. and Zhao, W., "Investigation of Surface Morphologies of TiO₂ Nanotube Arrays by Anodization in Ethylene Glycol Electrolytes", *J. Optoelectron. Adv. Mater.*, **2011**, 13, 684-688
 62. Mor, G. K.; Varghese, O. K.; Paulose, M.; Shankar, K. and Grimes, C. A., "A review on highly ordered, vertically oriented TiO₂ nanotube arrays: Fabrication, material properties, and solar energy applications", *Sol. Energy Mater. Sol. Cells*, **2006**, 90, 2011-2075
 63. Gan, Y. X.; Gan, B. J.; Clark, E.; Su, L. and Zhang, L., "Converting Environmentally Hazardous Materials into Clean Energy Using a Novel Nanostructured Photoelectrochemical Fuel Cell", *Mater. Res. Bull.*, **2012**, 47, 2380-2388

64. Karthik, S.; Gopal, K. M.; Haripriya, E. P.; Sorachon, Y.; Maggie, P.; Oomman, K. V. and Craig, A. G., "Highly-Ordered TiO₂ Nanotube Arrays Up to 220um in Length: Sse in Water Photoelectrolysis and Dye-Sensitized Solar Cells", *Nanotechnology*, **2007**, 18, 065707
65. Zhang, Z.; Wang, C. C.; Zakaria, R. and Ying, J. Y., "Role of Particle Size in Nanocrystalline TiO₂-Based Photocatalysts", *J. Phys. Chem. B*, **1998**, 102, 10871-10878
66. Yu, J. C.; Zhang, L. and Yu, J., "Direct Sonochemical Preparation and Characterization of Highly Active Mesoporous TiO₂ with a Bicrystalline Framework", *Chem. Mater.*, **2002**, 14, 4647-4653
67. Liu, G.; Hoivik, N. and Wang, K., "Small Diameter TiO₂ Nanotubes with Enhanced Photoresponsivity", *Electrochem. Commun.*, **2013**, 28, 107-110
68. Kim, K.-P.; Lee, S.-J.; Kim, D.-H.; Hwang, D.-K. and Heo, Y.-W., "Dye-Sensitized Solar Cells Based on Trench Structured TiO₂ Nanotubes in Ti Substrate", *Curr. Appl. Phys.*, **2013**, 13, 795-798
69. Oh, H.-J.; Hock, R.; Schurr, R.; Hölzing, A. and Chi, C.-S., "Phase Transformation and Photocatalytic Characteristics of Anodic TiO₂ Nanotubular Film", *J. Phys. Chem. Solids*, **2013**, 74, 708-715
70. Xiong, H.; Slater, M. D.; Balasubramanian, M.; Johnson, C. S. and Rajh, T., "Amorphous TiO₂ Nanotube Anode for Rechargeable Sodium Ion Batteries", *J. Phys. Chem. B Lett.*, **2011**, 2, 2560-2565
71. Kyeremateng, N. A.; Plylahan, N.; dos Santos, A. C. S.; Taveira, L. V.; Dick, L. F. P. and Djenizian, T., "Sulfidated TiO₂ Nanotubes: A Potential 3D Cathode

- Material for Li-Ion Micro Batteries", *Chem. Commun.*, **2013**, 49, 4205-4207
72. Wang, N.; Li, H.; Lv, W.; Li, J.; Wang, J.; Zhang, Z. and Liu, Y., "Effects of TiO₂ Nanotubes with Different Diameters on Gene Expression and Osseointegration of Implants in Minipigs", *Biomaterials*, **2011**, 32, 6900-6911
 73. Brammer, K. S.; Oh, S.; Cobb, C. J.; Bjursten, L. M.; Heyde, H. v. d. and Jin, S., "Improved Bone-Forming Functionality on Diameter-Controlled TiO₂ Nanotube Surface", *Acta Biomaterialia*, **2009**, 5, 3215-3223
 74. Park, J.; Bauer, S.; von der Mark, K. and Schmuki, P., "Nanosize and Vitality: TiO₂ Nanotube Diameter Directs Cell Fate", *Nano Lett.*, **2007**, 7, 1686-1691
 75. Bauer, S.; Park, J.; Faltenbacher, J.; Berger, S.; von der Mark, K. and Schmuki, P., "Size Selective Behavior of Mesenchymal Stem Cells on ZrO₂ and TiO₂ Nanotube Arrays", *Int. Biol.*, **2009**, 1, 525-532
 76. Oh, S.; Brammer, K. S.; Li, Y. S. J.; Teng, D.; Engler, A. J.; Chien, S. and Jin, S., "Stem Cell Fate Dictated Solely by Altered Nanotube Dimension", *Proc. Natl. Acad. Sci.*, **2009**, 106, 2130-2135
 77. Tao, J.; Zhao, J.; Tang, C.; Kang, Y. and Li, Y., "Mechanism Study of Self-Organized TiO₂ Nanotube Arrays by Anodization", *New J. Chem.*, **2008**, 32, 2164-2168
 78. Macak, J. M.; Tsuchiya, H.; Ghicov, A.; Yasuda, K.; Hahn, R.; Bauer, S. and Schmuki, P., "TiO₂ Nanotubes: Self-Organized Electrochemical Formation, Properties and Applications", *Curr. Opin. Solid State Mater. Sci.*, **2007**, 11, 3-18
 79. Fujishima, A. and Honda, K., "Electrochemical photolysis of water at a semiconductor electrode", *Nature*, **1972**, 238, 37-8

80. Mills, A. and Le Hunte, S., "An overview of semiconductor photocatalysis", *J. Photochem. Photobiol. A*, **1997**, 108, 1-35
81. Zwilling, V.; Aucouturier, M. and Darque-Ceretti, E., "Anodic oxidation of titanium and TA6V alloy in chromic media. An electrochemical approach", *Electrochim. Acta*, **1999**, 45, 921-929
82. Beranek, R.; Hildebrand, H. and Schmuki, P., "Self-Organized Porous Titanium Oxide Prepared in H₂SO₄/HF Electrolytes", *Electrochem. Solid-State Lett.*, **2003**, 6, B12-B14
83. Ghicov, A.; Tsuchiya, H.; Macak, J. M. and Schmuki, P., "Titanium oxide nanotubes prepared in phosphate electrolytes", *Electrochem. Commun.*, **2005**, 7, 505-509
84. Su, Z. and Zhou, W., "Formation Mechanism of Porous Anodic Aluminium and Titanium Oxides", *Adv. Mater.*, **2008**, 20, 3663-3667
85. Su, Z. and Zhou, W., "Formation, microstructures and crystallization of anodic titanium oxide tubular arrays", *J. Mater. Chem.*, **2009**, 19, 2301-2309
86. Yoriya, S. and Grimes, C. A., "Self-Assembled TiO₂ Nanotube Arrays by Anodization of Titanium in Diethylene Glycol: Approach to Extended Pore Widening", *Langmuir*, **2010**, 26, 417-420
87. Wang, J. and Lin, Z., "Freestanding TiO₂ Nanotube Arrays with Ultrahigh Aspect Ratio via Electrochemical Anodization", *Chem. Mater.*, **2008**, 20, 1257-1261
88. Wang, J. and Lin, Z., "Anodic Formation of Ordered TiO₂ Nanotube Arrays: Effects of Electrolyte Temperature and Anodization Potential", *The Journal of Physical Chemistry C*, **2009**, 113, 4026-4030

89. Mowbray, D. J.; Martinez, J. I.; García Lastra, J. M.; Thygesen, K. S. and Jacobsen, K. W., "Stability and Electronic Properties of TiO₂ Nanostructures With and Without B and N Doping", *J. Phys. Chem. C*, **2009**, 113, 12301-12308
90. O'Regan, B. and Gratzel, M., "A low-cost, high-efficiency solar cell based on dye-sensitized colloidal TiO₂ films", *Nature*, **1991**, 353, 737-740
91. Macák, J. M.; Tsuchiya, H.; Ghicov, A. and Schmuki, P., "Dye-sensitized anodic TiO₂ nanotubes", *Electrochem. Commun.*, **2005**, 7, 1133-1137
92. Asahi, R.; Morikawa, T.; Ohwaki, T.; Aoki, K. and Taga, Y., "Visible-Light Photocatalysis in Nitrogen-Doped Titanium Oxides", *Science*, **2001**, 293, 269-271
93. Lindgren, T.; Mwabora, J. M.; Avendaño, E.; Jonsson, J.; Hoel, A.; Granqvist, C.-G. and Lindquist, S.-E., "Photoelectrochemical and Optical Properties of Nitrogen Doped Titanium Dioxide Films Prepared by Reactive DC Magnetron Sputtering", *J. Phys. Chem. B*, **2003**, 107, 5709-5716
94. Kosowska, B.; Mozia, S.; Morawski, A. W.; Grzmil, B.; Janus, M. and Kałucki, K., "The preparation of TiO₂-nitrogen doped by calcination of TiO₂·xH₂O under ammonia atmosphere for visible light photocatalysis", *Sol. Energy Mater. Sol. Cells*, **2005**, 88, 269-280
95. Wang, J. and Lin, Z., "Dye-Sensitized TiO₂ Nanotube Solar Cells with Markedly Enhanced Performance via Rational Surface Engineering", *Chem. Mater.*, **2010**, 22, 579-584
96. Huang, B. S.; Tseng, H. H. and Wey, M. Y., "Comparison of visible-light-driven routes of anion-doped TiO₂ and composite photocatalyst", *J. Ceram. Soc. Jpn.*, **2009**, 117, 753-758

97. Dong, L.; Ma, Y.; Wang, Y.; Tian, Y.; Ye, G.; Jia, X. and Cao, G., "Preparation and characterization of nitrogen-doped titania nanotubes", *Mater. Lett.*, **2009**, 63, 1598-1600
98. Wang, J.; Zhao, L.; Lin, V. S. Y. and Lin, Z., "Formation of various TiO₂ nanostructures from electrochemically anodized titanium", *J. Mater. Chem.*, **2009**, 19, 3682-3687
99. Ohsaka, T.; Izumi, F. and Fujiki, Y., "Raman spectrum of anatase, TiO₂", *J. Raman Spectrosc.*, **1978**, 7, 321-324
100. Bersani, D.; Antonioli, G.; Lottici, P. P. and Lopez, T., "Raman study of nanosized titania prepared by sol-gel route", *J. Non-Cryst. Solids*, **1998**, 232-234, 175-181
101. Sreekantan, S.; Hazan, R. and Lockman, Z., "Photoactivity of anatase-rutile TiO₂ nanotubes formed by anodization method", *Thin Solid Films*, **2009**, 518, 16-21
102. Li, G.; Liu, Z. Q.; Lu, J.; Wang, L. and Zhang, Z., "Effect of calcination temperature on the morphology and surface properties of TiO₂ nanotube arrays", *Appl. Surf. Sci.*, **2009**, 255, 7323-7328
103. Yang, Y.; Wang, X. and Li, L., "Crystallization and Phase Transition of Titanium Oxide Nanotube Arrays", *J. Am. Ceram. Soc.*, **2008**, 91, 632-635
104. Zheng, R.; Lin, L.; Xie, J.; Zhu, Y. and Xie, Y., "State of Doped Phosphorus and Its Influence on the Physicochemical and Photocatalytic Properties of P-doped Titania", *J. Phys. Chem. C*, **2008**, 112, 15502-15509
105. Tsuchiya, T.; Hirata, M. and Chiba, N., "Young's modulus, fracture strain, and tensile strength of sputtered titanium thin films", *Thin Solid Films*, **2005**, 484, 152

106. Wang, S. H.; Chen, T. K.; Rao, K. K. and Wong, M. S., "Nanocolumnar titania thin films uniquely incorporated with carbon for visible light photocatalysis", *Appl. Catal. B*, **2007**, 76, 328-334
107. Machunze, R. and Janssen, G. C. A. M., "Stress gradients in titanium nitride thin films", *Surf. Coat. Technol.*, **2008**, 203, 550-553
108. Asahi, R.; Taga, Y.; Mannstadt, W. and Freeman, A. J., "Electronic and optical properties of anatase TiO₂", *Phys. Rev. B*, **2000**, 61, 7459-7465
109. Ding, Z.; Lu, G. Q. and Greenfield, P. F., "Role of the Crystallite Phase of TiO₂ in Heterogeneous Photocatalysis for Phenol Oxidation in Water", *J. Phys. Chem. B*, **2000**, 104, 4815-4820
110. Ting, C. C.; Chen, S. Y. and Liu, D. M., "Structural evolution and optical properties of TiO₂ thin films prepared by thermal oxidation of sputtered Ti films", *J. Appl. Phys.*, **2000**, 88, 4628-4633
111. Yu, J. C.; Lin, J.; Lo, D. and Lam, S. K., "Influence of Thermal Treatment on the Adsorption of Oxygen and Photocatalytic Activity of TiO₂", *Langmuir*, **2000**, 16, 7304-7308
112. Rodríguez Talavera, R.; Vargas, S.; Arroyo Murillo, R.; Montiel Campos, R. and Haro Poniatowski, E., "Modification of the phase transition temperatures in titania doped with various cations", *J. Mater. Res.*, **1997**, 12, 439-443
113. Rahman, M. M.; Krishna, K. M.; Soga, T.; Jimbo, T. and Umeno, M., "Optical properties and X-ray photoelectron spectroscopic study of pure and Pb-doped TiO₂ thin films", *J. Phys. Chem. Solids*, **1999**, 60, 201-210

114. Vargas, S.; Arroyo, R.; Haro, E. and Rodríguez, R., "Effects of cationic dopants on the phase transition temperature of titania prepared by the sol-gel method", *J. Mater. Res.*, **1999**, 14, 3932-3937
115. Al Salim, N. I.; Bagshaw, S. A.; Bittar, A.; Kemmitt, T.; James McQuillan, A.; Mills, A. M. and Ryan, M. J., "Characterisation and activity of sol-gel-prepared TiO₂ photocatalysts modified with Ca, Sr or Ba ion additives", *J. Mater. Chem.*, **2000**, 10, 2358-2363
116. Cromer, D. T. and Herrington, K., "The Structures of Anatase and Rutile", *J. Am. Chem. Soc.*, **1955**, 77, 4708-4709
117. Baur, V. W. H., "Atomabstände und Bindungswinkel im Brookit, TiO₂", *Acta Cryst.*, **1961**, 14, 214-216
118. Bokhimi, X.; Novaro, O.; Gonzalez, R. D.; Lopez, T.; Chimal, O.; Asomoza, A. and Gomez, R., "Copper Precursor Effect on Reducibility and Titania Phases Concentration of Sol-Gel CuTiO₂ Catalyst", *J. Solid State Chem.*, **1999**, 144, 349-353
119. Foger, K. and Anderson, J. R., "Thermally stable SMSI supports: Iridium supported on TiO₂-Al₂O₃ and on Ce-stabilized anatase", *Appl. Catal.*, **1986**, 23, 139-155
120. Xia, B.; Huang, H. and Xie, Y., "Heat treatment on TiO₂ nanoparticles prepared by vapor-phase hydrolysis", *Mater. Sci. Eng. B*, **1999**, 57, 150-154
121. Morgado Jr, E.; de Abreu, M. A. S.; Pravia, O. R. C.; Marinkovic, B. A.; Jardim, P. M.; Rizzo, F. C. and Araújo, A. S., "A study on the structure and thermal stability of titanate nanotubes as a function of sodium content", *Solid State Sci.*,

2006, 8, 888-900

122. Suhail, M. H.; Rao, G. M. and Mohan, S., "DC reactive magnetron sputtering of titanium-structural and optical characterization of TiO₂ films", *J. Appl. Phys.*, **1992**, 71, 1421-1427
123. Wicaksana, D.; Kobayashi, A. and Kinbara, A., "Process effects on structural properties of TiO₂ thin films by reactive sputtering", *J. Vac. Sci. Technol. A*, **1992**, 10, 1479-1482
124. Wiggins, M. D.; Nelson, M. C. and Aita, C. R., "Phase development in sputter deposited titanium dioxide", *J. Vac. Sci. Technol. A*, **1996**, 14, 772-776
125. Macak, J. M.; Tsuchiya, H.; Berger, S.; Bauer, S.; Fujimoto, S. and Schmuki, P., "On wafer TiO₂ nanotube-layer formation by anodization of Ti-films on Si", *Chem. Phys. Lett.*, **2006**, 428, 421-425
126. Ortiz, G. F.; Hanzu, I.; Knauth, P.; Lavela, P.; Tirado, J. L. and Djenizian, T., "TiO₂ nanotubes manufactured by anodization of Ti thin films for on-chip Li-ion 2D microbatteries", *Electrochim. Acta*, **2009**, 54, 4262-4268
127. Zhang, H. and F. Banfield, J., "Thermodynamic analysis of phase stability of nanocrystalline titania", *J. Mater. Chem.*, **1998**, 8, 2073-2076
128. Zhang, H. and Banfield, J. F., "Understanding Polymorphic Phase Transformation Behavior during Growth of Nanocrystalline Aggregates: Insights from TiO₂", *J. Phys. Chem. B*, **2000**, 104, 3481-3487
129. Whittemore Jr, O. J. and Sipe, J. J., "Pore growth during the initial stages of sintering ceramics", *Powder Technol.*, **1974**, 9, 159-164
130. Varela, J. A.; Whittemore, O. J. and Longo, E., "Pore size evolution during

- sintering of ceramic oxides", *Ceram. Int.*, **1990**, 16, 177-189
131. Kumar, K.-N. P.; Keizer, K.; Burggraaf, A. J.; Okubo, T.; Nagamoto, H. and Morooka, S., "Densification of nanostructured titania assisted by a phase transformation", *Nature*, **1992**, 358, 48-51
 132. Kumar, K. N. P.; Engell, J.; Kumar, J.; Keizer, K.; Okubo, T. and Sadakata, M., "Pore-structure stabilization by controlling particle coordination", *J. Mater. Sci. Lett.*, **1995**, 14, 1784-1788
 133. Shannon, R. D., "Phase Transformation Studies in TiO₂ Supporting Different Defect Mechanisms in Vacuum-Reduced and Hydrogen-Reduced Rutile", *J. Appl. Phys.*, **1964**, 35, 3414-3416
 134. Shannon, R. D. and Pask, J. A., "Kinetics of the Anatase-Rutile Transformation", *J. Am. Ceram. Soc.*, **1965**, 48, 391-398
 135. Gouma, P. I.; Dutta, P. K. and Mills, M. J., "Structural stability of titania thin films", *Nanostruct. Mater.*, **1999**, 11, 1231-1237
 136. Huang, J. Y.; Chen, S.; Jo, S. H.; Wang, Z.; Han, D. X.; Chen, G.; Dresselhaus, M. S. and Ren, Z. F., "Atomic-Scale Imaging of Wall-by-Wall Breakdown and Concurrent Transport Measurements in Multiwall Carbon Nanotubes", *Phys. Rev. Lett.*, **2005**, 94, 236802
 137. Huang, J. Y.; Chen, S.; Ren, Z. F.; Chen, G. and Dresselhaus, M. S., "Real-Time Observation of Tubule Formation from Amorphous Carbon Nanowires under High-Bias Joule Heating", *Nano Lett.*, **2006**, 6, 1699-1705
 138. Huang, J. Y., "In Situ Observation of Quasimelting of Diamond and Reversible Graphite–Diamond Phase Transformations", *Nano Lett.*, **2007**, 7, 2335-2340

139. Adachi, M.; Murata, Y.; Okada, I. and Yoshikawa, S., "Formation of Titania Nanotubes and Applications for Dye-Sensitized Solar Cells", *J. Electrochem. Soc.*, **2003**, 150, G488-G493
140. Varghese, O. K.; Gong, D.; Paulose, M.; Ong, K. G. and Grimes, C. A., "Hydrogen sensing using titania nanotubes", *Sensors and Actuators B: Chemical*, **2003**, 93, 338-344
141. Armstrong, G.; Armstrong, A. R.; Bruce, P. G.; Reale, P. and Scrosati, B., "TiO₂(B) Nanowires as an Improved Anode Material for Lithium-Ion Batteries Containing LiFePO₄ or LiNi_{0.5}Mn_{1.5}O₄ Cathodes and a Polymer Electrolyte", *Adv. Mater.*, **2006**, 18, 2597-2600
142. Umebayashi, T.; Yamaki, T.; Itoh, H. and Asai, K., "Analysis of electronic structures of 3D transition metal-doped TiO₂ based on band calculations", *J. Phys. Chem. Solids*, **2002**, 63, 1909-1920
143. Kim, Y. H.; Chang, K. J. and Louie, S. G., "Electronic structure of radially deformed BN and BC₃ nanotubes", *Phys. Rev. B*, **2001**, 63, 205408
144. Bai, X.; Golberg, D.; Bando, Y.; Zhi, C.; Tang, C.; Mitome, M. and Kurashima, K., "Deformation-Driven Electrical Transport of Individual Boron Nitride Nanotubes", *Nano Lett.*, **2007**, 7, 632-637
145. Maruska, H. P. and Ghosh, A. K., "Photocatalytic decomposition of water at semiconductor electrodes", *Solar Energy*, **1978**, 20, 443-458
146. Villafuerte, M.; Juárez, G.; de Heluani, S. P. and Comedi, D., "Hysteretic current–voltage characteristics in RF-sputtered nanocrystalline TiO₂ thin films", *Physica B: Condensed Matter*, **2007**, 398, 321-324

147. Padovani, F. A. and Stratton, R., "Field and thermionic-field emission in Schottky barriers", *Solid-State Electron.*, **1966**, 9, 695-707
148. Zhang, Z. Y.; Jin, C. H.; Liang, X. L.; Chen, Q. and Peng, L. M., "Current-voltage characteristics and parameter retrieval of semiconducting nanowires", *Appl. Phys. Lett.*, **2006**, 88, 073102
149. Stamate, M.; Lazar, G. and Lazar, I., "Anatase - rutile TiO₂ thin films deposited in a d.c. magnetron sputtering system", *Rom J Phys*, **2008**, 53, 217-221
150. Acket, G. A. and Volger, J., "On electrical conduction in reduced rutile", *Physica*, **1964**, 30, 1667-1669
151. Bogomolov, V. N. and Zhuze, V. P., *Sov. Phys. Solid State*, **1964**, 5, 2404
152. Yagi, E.; Hasiguti, R. R. and Aono, M., "Electronic conduction above 4 K of slightly reduced oxygen-deficient rutile TiO_{2-x}", *Phys. Rev. B*, **1996**, 54, 7945-7956
153. Hendry, E.; Wang, F.; Shan, J.; Heinz, T. F. and Bonn, M., "Electron transport in TiO₂ probed by THz time-domain spectroscopy", *Phys. Rev. B*, **2004**, 69, 081101
154. Peng, H. Y.; McCluskey, M. D.; Gupta, Y. M.; Kneissl, M. and Johnson, N. M., "Shock-induced band-gap shift in GaN: Anisotropy of the deformation potentials", *Phys. Rev. B*, **2005**, 71, 115207
155. Nishidate, K. and Hasegawa, M., "Universal band gap modulation by radial deformation in semiconductor single-walled carbon nanotubes", *Phys. Rev. B*, **2008**, 78, 195403
156. Mahanti, S. D.; Hoang, K. and Ahmad, S., "Deep defect states in narrow band-gap semiconductors", *Phys. Rev. B*, **2007**, 401–402, 291-295

157. Robertson, J.; Sharia, O. and Demkov, A. A., "Fermi level pinning by defects in HfO₂-metal gate stacks", *Appl. Phys. Lett.*, **2007**, 91, 132912
158. Arnold, M. S.; Avouris, P.; Pan, Z. W. and Wang, Z. L., "Field-Effect Transistors Based on Single Semiconducting Oxide Nanobelts", *J. Phys. Chem. B*, **2003**, 107, 659-663
159. Huang, M.; Rugheimer, P.; Lagally, M. G. and Liu, F., "Bending of nanoscale ultrathin substrates by growth of strained thin films and islands", *Phys. Rev. B*, **2005**, 72, 085450
160. Lin, X.; He, X. B.; Yang, T. Z.; Guo, W.; Shi, D. X.; Gao, H. J.; Ma, D. D. D.; Lee, S. T.; Liu, F. and Xie, X. C., "Intrinsic current-voltage properties of nanowires with four-probe scanning tunneling microscopy: A conductance transition of ZnO nanowire", *Appl. Phys. Lett.*, **2006**, 89, 043103
161. Mor, G. K.; Varghese, O. K.; Paulose, M.; Mukherjee, N. and Grimes, C. A., "Fabrication of tapered, conical-shaped titania nanotubes", *J. Mater. Res.*, **2003**, 18, 2588-2593
162. Varghese, O. K.; Gong, D.; Paulose, M.; Ong, K. G.; Dickey, E. C. and Grimes, C. A., "Extreme Changes in the Electrical Resistance of Titania Nanotubes with Hydrogen Exposure", *Adv. Mater.*, **2003**, 15, 624-627
163. Matsushita, S. I.; Miwa, T.; Tryk, D. A. and Fujishima, A., "New Mesostructured Porous TiO₂ Surface Prepared Using a Two-Dimensional Array-Based Template of Silica Particles", *Langmuir*, **1998**, 14, 6441-6447
164. Mor, G. K.; Shankar, K.; Paulose, M.; Varghese, O. K. and Grimes, C. A., "Enhanced Photocleavage of Water Using Titania Nanotube Arrays", *Nano Lett.*,

- 2004**, 5, 191-195
165. Jiu, J.; Isoda, S.; Adachi, M. and Wang, H., "Dye-sensitized solar cell based on nanocrystalline TiO₂ with 3–10 nm in diameter", *J Mater Sci: Mater Electron*, **2007**, 18, 593-597
 166. Kwak, E. S.; Lee, W.; Park, N.-G.; Kim, J. and Lee, H., "Compact Inverse-Opal Electrode Using Non-Aggregated TiO₂ Nanoparticles for Dye-Sensitized Solar Cells", *Adv. Funct. Mater.*, **2009**, 19, 1093-1099
 167. Xu, A.; Zhu, J.; Gao, Y. and Liu, H., *Chem. Res. Chin. Univ.*, **2001**, 17, 281
 168. Wang, C.-y.; Bahnemann, D. W. and Dohrmann, J. K., "A novel preparation of iron-doped TiO nanoparticles with enhanced photocatalytic activity", *Chem. Commun.*, **2000**, 0, 1539-1540
 169. Wang, Y.; Hao, Y.; Cheng, H.; Ma, J.; Xu, B.; Li, W. and Cai, S., "The photoelectrochemistry of transition metal-ion-doped TiO₂ nanocrystalline electrodes and higher solar cell conversion efficiency based on Zn²⁺-doped TiO₂ electrode", *J. Mater. Sci.*, **1999**, 34, 2773-2779
 170. Coloma, F.; Marquez, F.; Rochester, C. H. and Anderson, J. A., "Determination of the nature and reactivity of copper sites in Cu-TiO₂ catalysts", *PCCP*, **2000**, 2, 5320-5327
 171. Kim, Y.-H.; Chang, K. J. and Louie, S. G., "Electronic structure of radially deformed BN and BC₃ nanotubes", *Physical Review B*, **2001**, 63, 205408
 172. Wang, G.; Chen, H.; Zhang, H.; Shen, Y.; Yuan, C.; Lu, Z.; Wang, G. and Yang, W., "Current-voltage characteristics of TiO₂PPy complex films", *Phys. Lett. A*, **1998**, 237, 165-168

173. Wahl, A. and Augustynski, J., "Charge Carrier Transport in Nanostructured Anatase TiO₂ Films Assisted by the Self-Doping of Nanoparticles", *The Journal of Physical Chemistry B*, **1998**, 102, 7820-7828
174. Asthana, A.; Shokuhfar, T.; Gao, Q.; Heiden, P.; Friedrich, C. and Yassar, R. S., "A study on the modulation of the electrical transport by mechanical straining of individual titanium dioxide nanotube", *Appl. Phys. Lett.*, **2010**, 97, 072107
175. Shokuhfar, T.; Arumugam, G. K.; Heiden, P. A.; Yassar, R. S. and Friedrich, C., "Direct Compressive Measurements of Individual Titanium Dioxide Nanotubes", *ACS Nano*, **2009**, 3, 3098-3102
176. Zwilling, V.; Darque-Ceretti, E.; Boutry-Forveille, A.; David, D.; Perrin, M. Y. and Aucouturier, M., "Structure and physicochemistry of anodic oxide films on titanium and TA6V alloy", *Surf. Interface Anal.*, **1999**, 27, 629-637
177. Macak, J. M.; Sirotna, K. and Schmuki, P., "Self-organized porous titanium oxide prepared in Na₂SO₄/NaF electrolytes", *Electrochim. Acta*, **2005**, 50, 3679-3684
178. Macák, J. M.; Tsuchiya, H. and Schmuki, P., "TiO₂-Nanoröhren mit hohem Aspektverhältnis durch Anodisieren von Ti", *Angew. Chem.*, **2005**, 117, 2136-2139
179. Macák, J. M.; Tsuchiya, H. and Schmuki, P., "High-Aspect-Ratio TiO₂ Nanotubes by Anodization of Titanium", *Angew. Chem. Int. Ed.*, **2005**, 44, 2100-2102
180. Macak, J. M.; Tsuchiya, H.; Taveira, L.; Aldabergerova, S. and Schmuki, P., "Glattwandige anodische TiO₂-Nanoröhren", *Angew. Chem.*, **2005**, 117, 7629-7632
181. Macak, J. M.; Tsuchiya, H.; Taveira, L.; Aldabergerova, S. and Schmuki, P.,

- "Smooth Anodic TiO₂ Nanotubes", *Angew. Chem. Int. Ed.*, **2005**, 44, 7463-7465
182. Kasuga, T.; Hiramatsu, M.; Hoson, A.; Sekino, T. and Niihara, K., "Titania Nanotubes Prepared by Chemical Processing", *Adv. Mater.*, **1999**, 11, 1307-1311
 183. Du, G. H.; Chen, Q.; Che, R. C.; Yuan, Z. Y. and Peng, L.-M., "Preparation and structure analysis of titanium oxide nanotubes", *Appl. Phys. Lett.*, **2001**, 79, 3702-3704
 184. Suzuki, Y. and Yoshikawa, S., "Synthesis and Thermal Analyses of TiO₂-Derived Nanotubes Prepared by the Hydrothermal Method", *J. Mater. Res.*, **2004**, 19, 982-985
 185. Rodriguez, J. A. and Fernandez-Garcia, M., "Synthesis Properties and Applications of Oxide Nanomaterials", *Wiley*, **2007**, 451
 186. Lbach, H. and Luth, H., "Solid State Physics: An Introduction to Principles of Material Science", *Springer*, **2003**,
 187. Hofmann, P., "Solid State Physics: An Introduction", *Wiley-VCH*, **2008**,
 188. Zhang, Z. Y.; Jin, C. H.; Liang, X. L.; Chen, Q. and Peng, L.-M., "Current-voltage characteristics and parameter retrieval of semiconducting nanowires", *Appl. Phys. Lett.*, **2006**, 88, 073102
 189. Yang, W. and Wolden, C. A., "Plasma-enhanced chemical vapor deposition of TiO₂ thin films for dielectric applications", *Thin Solid Films*, **2006**, 515, 1708-1713
 190. Rausch, N. and Burte, E. P., "Thin high-dielectric TiO₂ films prepared by low pressure MOCVD", *Microelectron. Eng.*, **1992**, 19, 725-728
 191. Hendry, E.; Wang, F.; Shan, J.; Heinz, T. F. and Bonn, M., "Electron transport in

- TiO₂ probed by THz time-domain spectroscopy", *Physical Review B*, **2004**, 69, 081101
192. Stamate, M.; Lazar, G. and Lazar, I., "Anatase-Rutile TiO₂ Thin Films Deposited in a D.C. Magnetron Sputtering System", *Rom. J. Phys.*, **2008**, 53, 217
 193. Peng, H. Y.; McCluskey, M. D.; Gupta, Y. M.; Kneissl, M. and Johnson, N. M., "Shock-induced band-gap shift in GaN: Anisotropy of the deformation potentials", *Physical Review B*, **2005**, 71, 115207
 194. Jun, S. and Cho, Y.-S., "Deformation-induced bandgap tuning of 2D silicon-based photonic crystals", *Opt. Express*, **2003**, 11, 2769-2774
 195. Fa, W.; Hu, F. and Dong, J., "Band gap variations in an AFM tip-deformed metallic carbon nanotube", *Phys. Lett. A*, **2004**, 331, 99-104
 196. Nishidate, K. and Hasegawa, M., "Universal band gap modulation by radial deformation in semiconductor single-walled carbon nanotubes", *Physical Review B*, **2008**, 78, 195403
 197. Mahanti, S. D.; Hoang, K. and Ahmad, S., "Deep defect states in narrow band-gap semiconductors", *Physica B: Condensed Matter*, **2007**, 401–402, 291-295
 198. Huang, M.; Rugheimer, P.; Lagally, M. G. and Liu, F., "Bending of nanoscale ultrathin substrates by growth of strained thin films and islands", *Physical Review B*, **2005**, 72, 085450
 199. Breckenridge, R. G. and Hosler, W. R., "Electrical Properties of Titanium Dioxide Semiconductors", *Physical Review*, **1953**, 91, 793-802
 200. Bogomolov, V. N. and Zhuze, V. P., *Sov. Phys., Solid State*, **1964**, 5, 2404
 201. Yagi, E.; Hasiguti, R. R. and Aono, M., "Electronic conduction above 4 K of

- slightly reduced oxygen-deficient rutile TiO_{2-x} ", *Physical Review B*, **1996**, 54, 7945-7956
202. Amine, K.; Belharouak, I.; Chen, Z. H.; Tran, T.; Yumoto, H.; Ota, N.; Myung, S. T. and Sun, Y. K., "Nanostructured Anode Material for High-Power Battery System in Electric Vehicles", *Adv. Mater.*, **2010**, 22, 3052-3057
 203. Zhou, H. S.; Wang, Y. G.; Li, H. Q. and He, P., "The Development of a New Type of Rechargeable Batteries Based on Hybrid Electrolytes", *Chemsuschem*, **2010**, 3, 1009-1019
 204. Abraham, K. M., "Directions in secondary lithium battery research and development", *Electrochim. Acta*, **1993**, 38, 1233-1248
 205. Winter, M.; Besenhard, J. O.; Spahr, M. E. and Novak, P., "Insertion electrode materials for rechargeable lithium batteries", *Adv. Mater.*, **1998**, 10, 725-763
 206. Rom, I.; Wachtler, M.; Papst, I.; Schmied, M.; Besenhard, J. O.; Hofer, F. and Winter, M., "Electron microscopical characterization of Sn/SnSb composite electrodes for lithium-ion batteries", *Solid State Ionics*, **2001**, 143, 329-336
 207. Du, N.; Zhang, H.; Chen, B.; Wu, J. B.; Ma, X. Y.; Liu, Z. H.; Zhang, Y. Q.; Yang, D.; Huang, X. H. and Tu, J. P., "Porous Co_3O_4 nanotubes derived from $\text{Co}_4(\text{CO})_{12}$ clusters on carbon nanotube templates: A highly efficient material for Li-battery applications", *Adv. Mater.*, **2007**, 19, 4505-+
 208. Chan, C. K.; Zhang, X. F. and Cui, Y., "High Capacity Li Ion Battery Anodes Using Ge Nanowires", *Nano Lett.*, **2007**, 8, 307-309
 209. Jansen, A. N.; Kahaian, A. J.; Kepler, K. D.; Nelson, P. A.; Amine, K.; Dees, D. W.; Vissers, D. R. and Thackeray, M. M., "Development of a high-power lithium-

- ion battery", *J. Power Sources*, **1999**, 81, 902-905
210. Fu, L. J.; Liu, H.; Zhang, H. P.; Li, C.; Zhang, T.; Wu, Y. P.; Holze, R. and Wu, H. Q., "Synthesis and electrochemical performance of novel core/shell structured nanocomposites", *Electrochem. Commun.*, **2006**, 8, 1-4
 211. Chen, X.; Schriver, M.; Suen, T. and Mao, S. S., "Fabrication of 10 nm diameter TiO₂ nanotube arrays by titanium anodization", *Thin Solid Films*, **2007**, 515, 8511-8514
 212. Wang, C. M.; Xu, W.; Liu, J.; Choi, D. W.; Arey, B.; Saraf, L. V.; Zhang, J. G.; Yang, Z. G.; Thevuthasan, S.; Baer, D. R. and Salmon, N., "In situ transmission electron microscopy and spectroscopy studies of interfaces in Li ion batteries: Challenges and opportunities", *J. Mater. Res.*, **2010**, 25, 1541-1547
 213. Huang, J. Y.; Zhong, L.; Wang, C. M.; Sullivan, J. P.; Xu, W.; Zhang, L. Q.; Mao, S. X.; Hudak, N. S.; Liu, X. H.; Subramanian, A.; Fan, H.; Qi, L.; Kushima, A. and Li, J., "In Situ Observation of the Electrochemical Lithiation of a Single SnO₂ Nanowire Electrode", *Science*, **2010**, 330, 1515-1520
 214. Ghassemi, H.; Au, M.; Chen, N.; Heiden, P. A. and Yassar, R. S., "In Situ Electrochemical Lithiation/Delithiation Observation of Individual Amorphous Si Nanorods", *ACS Nano*, **2011**, 5, 7805-7811
 215. Ghassemi, H.; Au, M.; Chen, N.; Heiden, P. A. and Yassar, R. S., "Real-time observation of lithium fibers growth inside a nanoscale lithium-ion battery", *Appl. Phys. Lett.*, **2011**, 99, 123113
 216. Gu, M.; Li, Y.; Li, X.; Hu, S.; Zhang, X.; Xu, W.; Thevuthasan, S.; Baer, D. R.; Zhang, J.-G.; Liu, J. and Wang, C., "In Situ TEM Study of Lithiation Behavior of

- Silicon Nanoparticles Attached to and Embedded in a Carbon Matrix", *ACS Nano*, **2012**, 6, 8439-8447
217. Nie, A.; Gan, L.-Y.; Cheng, Y.; Asayesh-Ardakani, H.; Li, Q.; Dong, C.; Tao, R.; Mashayek, F.; Wang, H.-T.; Schwingenschlögl, U.; Klie, R. F. and Yassar, R. S., "Atomic-Scale Observation of Lithiation Reaction Front in Nanoscale SnO₂ Materials", *ACS Nano*, **2013**,
 218. Liu, X. H.; Zhang, L. Q.; Zhong, L.; Liu, Y.; Zheng, H.; Wang, J. W.; Cho, J.-H.; Dayeh, S. A.; Picraux, S. T.; Sullivan, J. P.; Mao, S. X.; Ye, Z. Z. and Huang, J. Y., "Ultrafast Electrochemical Lithiation of Individual Si Nanowire Anodes", *Nano Lett.*, **2011**, 11, 2251-2258
 219. Wang, C.-M.; Li, X.; Wang, Z.; Xu, W.; Liu, J.; Gao, F.; Kovarik, L.; Zhang, J.-G.; Howe, J.; Burton, D. J.; Liu, Z.; Xiao, X.; Thevuthasan, S. and Baer, D. R., "In Situ TEM Investigation of Congruent Phase Transition and Structural Evolution of Nanostructured Silicon/Carbon Anode for Lithium Ion Batteries", *Nano Lett.*, **2012**, 12, 1624-1632
 220. Yang, H.; Huang, S.; Huang, X.; Fan, F.; Liang, W.; Liu, X. H.; Chen, L.-Q.; Huang, J. Y.; Li, J.; Zhu, T. and Zhang, S., "Orientation-Dependent Interfacial Mobility Governs the Anisotropic Swelling in Lithiated Silicon Nanowires", *Nano Lett.*, **2012**, 12, 1953-1958
 221. Liu, X. H.; Zhong, L.; Huang, S.; Mao, S. X.; Zhu, T. and Huang, J. Y., "Size-Dependent Fracture of Silicon Nanoparticles During Lithiation", *ACS Nano*, **2012**, 6, 1522-1531
 222. Liu, X. H.; Wang, J. W.; Huang, S.; Fan, F.; Huang, X.; Liu, Y.; Krylyuk, S.; Yoo,

- J.; Dayeh, S. A.; Davydov, A. V.; Mao, S. X.; Picraux, S. T.; Zhang, S.; Li, J.; Zhu, T. and Huang, J. Y., "In situ atomic-scale imaging of electrochemical lithiation in silicon", *Nat Nano*, **2012**, 7, 749-756
223. McDowell, M. T.; Ryu, I.; Lee, S. W.; Wang, C.; Nix, W. D. and Cui, Y., "Studying the Kinetics of Crystalline Silicon Nanoparticle Lithiation with In Situ Transmission Electron Microscopy", *Adv. Mater.*, **2012**, 24, 6034-6041
224. Liu, X. H.; Huang, S.; Picraux, S. T.; Li, J.; Zhu, T. and Huang, J. Y., "Reversible Nanopore Formation in Ge Nanowires during Lithiation–Delithiation Cycling: An In Situ Transmission Electron Microscopy Study", *Nano Lett.*, **2011**, 11, 3991-3997
225. Liu, Y.; Hudak, N. S.; Huber, D. L.; Limmer, S. J.; Sullivan, J. P. and Huang, J. Y., "In Situ Transmission Electron Microscopy Observation of Pulverization of Aluminum Nanowires and Evolution of the Thin Surface Al_2O_3 Layers during Lithiation–Delithiation Cycles", *Nano Lett.*, **2011**, 11, 4188-4194
226. Wang, C.-M.; Xu, W.; Liu, J.; Zhang, J.-G.; Saraf, L. V.; Arey, B. W.; Choi, D.; Yang, Z.-G.; Xiao, J.; Thevuthasan, S. and Baer, D. R., "In Situ Transmission Electron Microscopy Observation of Microstructure and Phase Evolution in a SnO_2 Nanowire during Lithium Intercalation", *Nano Lett.*, **2011**, 11, 1874-1880
227. Zhang, L. Q.; Liu, X. H.; Perng, Y.-C.; Cho, J.; Chang, J. P.; Mao, S. X.; Ye, Z. Z. and Huang, J. Y., "Direct observation of Sn crystal growth during the lithiation and delithiation processes of SnO_2 nanowires", *Micron*, **2012**, 43, 1127-1133
228. Zhong, L.; Liu, X. H.; Wang, G. F.; Mao, S. X. and Huang, J. Y., "Multiple-Stripe Lithiation Mechanism of Individual SnO_2 Nanowires in a Flooding Geometry",

Phys. Rev. Lett., **2011**, 106, 248302

229. Kushima, A.; Liu, X. H.; Zhu, G.; Wang, Z. L.; Huang, J. Y. and Li, J., "Leapfrog Cracking and Nanoamorphization of ZnO Nanowires during In Situ Electrochemical Lithiation", *Nano Lett.*, **2011**, 11, 4535-4541
230. Liu, X. H.; Wang, J. W.; Liu, Y.; Zheng, H.; Kushima, A.; Huang, S.; Zhu, T.; Mao, S. X.; Li, J.; Zhang, S.; Lu, W.; Tour, J. M. and Huang, J. Y., "In situ transmission electron microscopy of electrochemical lithiation, delithiation and deformation of individual graphene nanoribbons", *Carbon*, **2012**, 50, 3836-3844
231. Liu, Y.; Zheng, H.; Liu, X. H.; Huang, S.; Zhu, T.; Wang, J.; Kushima, A.; Hudak, N. S.; Huang, X.; Zhang, S.; Mao, S. X.; Qian, X.; Li, J. and Huang, J. Y., "Lithiation-Induced Embrittlement of Multiwalled Carbon Nanotubes", *ACS Nano*, **2011**, 5, 7245-7253
232. Su, Q.; Chang, L.; Zhang, J.; Du, G. and Xu, B., "In Situ TEM Observation of the Electrochemical Process of Individual CeO₂/Graphene Anode for Lithium Ion Battery", *The Journal of Physical Chemistry C*, **2013**, 117, 4292-4298
233. Shin, D. H.; Shokuhfar, T.; Choi, C. K.; Lee, S.-H. and Friedrich, C., "Wettability Changes of TiO₂ Nanotube Surfaces", *Nanotechnology*, **2011**, 22, 315704
234. Wang, C. M.; Yang, Z. G.; Thevuthasan, S.; Liu, J.; Baer, D. R.; Choi, D.; Wang, D. H.; Zhang, J. G.; Saraf, L. V. and Nie, Z. M., "Crystal and electronic structure of lithiated nanosized rutile TiO₂ by electron diffraction and electron energy-loss spectroscopy", *Appl. Phys. Lett.*, **2009**, 94, 233116
235. Koyama, Y.; Mizoguchi, T.; Ikeno, H. and Tanaka, I., "Electronic Structure of Lithium Nickel Oxides by Electron Energy Loss Spectroscopy", *J. Phys. Chem. B*,

2005, 109, 10749-10755

236. Okada, M.; Jin, P.; Yamada, Y.; Tazawa, M. and Yoshimura, K., "Low-energy electron energy loss spectroscopy of rutile and anatase TiO₂ films in the core electron excitation regions", *Surf. Sci.*, **2004**, 566–568, Part 2, 1030-1034
237. Bertoni, G.; Beyers, E.; Verbeeck, J.; Mertens, M.; Cool, P.; Vansant, E. F. and Van Tendeloo, G., "Quantification of crystalline and amorphous content in porous samples from electron energy loss spectroscopy", *Ultramicroscopy*, **2006**, 106, 630-635
238. Lusvardi, V. S.; Barteau, M. A.; Chen, J. G.; Eng Jr, J.; Frühberger, B. and Teplyakov, A., "An NEXAFS investigation of the reduction and reoxidation of TiO₂(001)", *Surf. Sci.*, **1998**, 397, 237-250
239. Akita, T.; Okumura, M.; Tanaka, K.; Ohkuma, K.; Kohyama, M.; Koyanagi, T.; Date, M.; Tsubota, S. and Haruta, M., "Transmission electron microscopy observation of the structure of TiO₂ nanotube and Au/TiO₂ nanotube catalyst", *Surf. Interface Anal.*, **2005**, 37, 265-269
240. Yoshiya, M.; Tanaka, I.; Kaneko, K. and Adachi, H., "First principles calculation of chemical shifts in ELNES/NEXAFS of titanium oxides", *J. Phys.: Condens. Matter*, **1999**, 11, 3217
241. Zheng, H.; Liu, Y.; Mao, S. X.; Wang, J. and Huang, J. Y., "Beam-assisted large elongation of *in situ* formed Li₂O nanowires", *Sci. Rep.*, **2012**, 2,
242. Li, J.; Tang, Z. and Zhang, Z., "H-titanate nanotube: a novel lithium intercalation host with large capacity and high rate capability", *Electrochem. Commun.*, **2005**, 7, 62-67

243. Zhou, Y. K.; Cao, L.; Zhang, F.-b.; He, B.-l. and Li, H.-l., "Lithium Insertion into TiO₂ Nanotube Prepared by the Hydrothermal Process", *J. Electrochem. Soc.*, **2003**, 150, A1246-A1249
244. Armstrong, G.; Armstrong, A. R.; Canales, J. and Bruce, P. G., "Nanotubes with the TiO₂-B structure", *Chem. Commun.*, **2005**, 2454-2456
245. Guan, D.; Cai, C. and Wang, Y., "Amorphous and Crystalline TiO₂ Nanotube Arrays for Enhanced Li-Ion Intercalation Properties", *J. Nanosci. Nanotechnol.*, **2011**, 11, 3641-3650
246. Wei, Z.; Liu, Z.; Jiang, R.; Bian, C.; Huang, T. and Yu, A., "TiO₂ nanotube array film prepared by anodization as anode material for lithium ion batteries", *J. Solid State Electrochem.*, **2010**, 14, 1045-1050
247. Cava, R. J.; Murphy, D. W.; Zahurak, S.; Santoro, A. and Roth, R. S., "The crystal structures of the lithium-inserted metal oxides Li_{0.5}TiO₂ anatase, LiTi₂O₄ spinel, and Li₂Ti₂O₄", *J. Solid State Chem.*, **1984**, 53, 64-75
248. Xiong, H.; Yildirim, H.; Shevchenko, E. V.; Prakapenka, V. B.; Koo, B.; Slater, M. D.; Balasubramanian, M.; Sankaranarayanan, S. K. R. S.; Greeley, J. P.; Tepavcevic, S.; Dimitrijevic, N. M.; Podsiadlo, P.; Johnson, C. S. and Rajh, T., "Self-Improving Anode for Lithium-Ion Batteries Based on Amorphous to Cubic Phase Transition in TiO₂ Nanotubes", *J. Phys. Chem. C*, **2011**, 116, 3181-3187
249. Yildirim, H.; Greeley, J. P. and Sankaranarayanan, S. K. R. S., "Concentration-Dependent Ordering of Lithiated Amorphous TiO₂", *J. Phys. Chem. C*, **2013**, 117, 3834-3845
250. Bechinger, C.; Ferrere, S.; Zaban, A.; Sprague, J. and Gregg, B. A.,

- "Photoelectrochromic windows and displays", *Nature*, **1996**, 383, 608-610
251. Hagfeldt, A. and Graetzel, M., "Light-Induced Redox Reactions in Nanocrystalline Systems", *Chem. Rev.*, **1995**, 95, 49-68
252. Huang, S. Y.; Kavan, L.; Exnar, I. and Grätzel, M., "Rocking Chair Lithium Battery Based on Nanocrystalline TiO₂ (Anatase)", *J. Electrochem. Soc.*, **1995**, 142, L142-L144
253. Smirnov, M. and Baddour-Hadjean, R., "Li intercalation in TiO₂ anatase: Raman spectroscopy and lattice dynamic studies", *The Journal of Chemical Physics*, **2004**, 121, 2348-2355
254. Ohzuku, T.; Takehara, Z. and Yoshizawa, S., "Nonaqueous lithium/titanium dioxide cell", *Electrochim. Acta*, **1979**, 24, 219-222
255. Wagemaker, M.; van de Krol, R.; Kentgens, A. P. M.; van Well, A. A. and Mulder, F. M., "Two Phase Morphology Limits Lithium Diffusion in TiO₂ (Anatase): A ⁷Li MAS NMR Study", *J. Am. Chem. Soc.*, **2001**, 123, 11454-11461
256. Murphy, D. W.; Cava, R. J.; Zahurak, S. M. and Santoro, A., "Ternary Li_xTiO₂ phases from insertion reactions", *Solid State Ionics*, **1983**, 9–10, Part 1, 413-417
257. Lindström, H.; Södergren, S.; Solbrand, A.; Rensmo, H.; Hjelm, J.; Hagfeldt, A. and Lindquist, S.-E., "Li⁺ Ion Insertion in TiO₂ (Anatase). 1. Chronoamperometry on CVD Films and Nanoporous Films", *The Journal of Physical Chemistry B*, **1997**, 101, 7710-7716
258. Wagemaker, M.; Kearley, G. J.; van Well, A. A.; Mutka, H. and Mulder, F. M., "Multiple Li Positions inside Oxygen Octahedra in Lithiated TiO₂ Anatase", *J. Am. Chem. Soc.*, **2002**, 125, 840-848

259. Xu, J.; Jia, C.; Cao, B. and Zhang, W. F., "Electrochemical properties of anatase TiO₂ nanotubes as an anode material for lithium-ion batteries", *Electrochim. Acta*, **2007**, 52, 8044-8047
260. Dylla, A. G.; Xiao, P.; Henkelman, G. and Stevenson, K. J., "Morphological Dependence of Lithium Insertion in Nanocrystalline TiO₂(B) Nanoparticles and Nanosheets", *The Journal of Physical Chemistry Letters*, **2012**, 3, 2015-2019
261. Dylla, A. G.; Henkelman, G. and Stevenson, K. J., "Lithium Insertion in Nanostructured TiO₂(B) Architectures", *Acc. Chem. Res.*, **2013**, 46, 1104-1112
262. Armstrong, A. R.; Armstrong, G.; Canales, J. and Bruce, P. G., "TiO₂-B Nanowires", *Angew. Chem. Int. Ed.*, **2004**, 43, 2286-2288
263. Armstrong, A. R.; Armstrong, G.; Canales, J.; García, R. and Bruce, P. G., "Lithium-Ion Intercalation into TiO₂-B Nanowires", *Adv. Mater.*, **2005**, 17, 862-865
264. Armstrong, G.; Armstrong, A. R.; Canales, J. and Bruce, P. G., "TiO₂ (B) Nanotubes as Negative Electrodes for Rechargeable Lithium Batteries", *Electrochem. Solid-State Lett.*, **2006**, 9, A139-A143
265. Zúkalová, M.; Kalbáč, M.; Kavan, L.; Exnar, I. and Graetzel, M., "Pseudocapacitive Lithium Storage in TiO₂(B)", *Chem. Mater.*, **2005**, 17, 1248-1255
266. Armstrong, A. R.; Arrouvel, C.; Gentili, V.; Parker, S. C.; Islam, M. S. and Bruce, P. G., "Lithium Coordination Sites in Li_xTiO₂(B): A Structural and Computational Study", *Chem. Mater.*, **2010**, 22, 6426-6432
267. Pavasupree, S.; Suzuki, Y.; Yoshikawa, S. and Kawahata, R., "Synthesis of

- titanate, TiO₂ (B), and anatase TiO₂ nanofibers from natural rutile sand", *J. Solid State Chem.*, **2005**, 178, 3110-3116
268. Aravindan, V.; Shubha, N.; Cheah, Y. L.; Prasanth, R.; Chuiling, W.; Prabhakar, R. R. and Madhavi, S., "Extraordinary long-term cycleability of TiO₂-B nanorods as anodes in full-cell assembly with electrospun PVdF-HFP membranes", *Journal of Materials Chemistry A*, **2013**, 1, 308-316
269. Armstrong, G.; Armstrong, A. R.; Canales, J. and Bruce, P. G., "Nanotubes with the TiO₂-B structure", *Chem. Commun.*, **2005**, 0, 2454-2456
270. Liu, S.; Jia, H.; Han, L.; Wang, J.; Gao, P.; Xu, D.; Yang, J. and Che, S., "Nanosheet-Constructed Porous TiO₂-B for Advanced Lithium Ion Batteries", *Adv. Mater.*, **2012**, 24, 3201-3204
271. Ren, Y.; Liu, Z.; Pourpoint, F.; Armstrong, A. R.; Grey, C. P. and Bruce, P. G., "Nanoparticulate TiO₂(B): An Anode for Lithium-Ion Batteries", *Angew. Chem. Int. Ed.*, **2012**, 51, 2164-2167
272. Arico, A. S.; Bruce, P.; Scrosati, B.; Tarascon, J.-M. and van Schalkwijk, W., "Nanostructured materials for advanced energy conversion and storage devices", *Nat Mater*, **2005**, 4, 366-377
273. Poizot, P.; Laruelle, S.; Grugeon, S.; Dupont, L. and Tarascon, J. M., "Nano-sized transition-metal oxides as negative-electrode materials for lithium-ion batteries", *Nature*, **2000**, 407, 496-499
274. Diebold, U., "Structure and properties of TiO₂ surfaces: a brief review", *Appl. Phys. A*, **2003**, 76, 681-687
275. Hu, Y. S.; Kienle, L.; Guo, Y. G. and Maier, J., "High Lithium Electroactivity of

- Nanometer-Sized Rutile TiO₂", *Adv. Mater.*, **2006**, 18, 1421-1426
276. Baudrin, E.; Cassaignon, S.; Koelsch, M.; Jolivet, J. P.; Dupont, L. and Tarascon, J. M., "Structural evolution during the reaction of Li with nano-sized rutile type TiO₂ at room temperature", *Electrochem. Commun.*, **2007**, 9, 337-342
 277. Koudriachova, M. V.; de Leeuw, S. W. and Harrison, N. M., "A new phase of lithiated titania predicted from first principles", *Chem. Phys. Lett.*, **2003**, 371, 150-156
 278. Borghols, W. J. H.; Wagemaker, M.; Lafont, U.; Kelder, E. M. and Mulder, F. M., "Impact of Nanosizing on Lithiated Rutile TiO₂", *Chem. Mater.*, **2008**, 20, 2949-2955
 279. Pfanzelt, M.; Kubiak, P. and Wohlfahrt-Mehrens, M., "Nanosized TiO₂ Rutile with High Capacity and Excellent Rate Capability", *Electrochem. Solid-State Lett.*, **2010**, 13, A91-A94
 280. Huang, X. and Pan, C., "Large-scale synthesis of single-crystalline rutile TiO₂ nanorods via a one-step solution route", *J. Cryst. Growth*, **2007**, 306, 117-122
 281. Bi, Z.; Paranthaman, M. P.; Menchhofer, P. A.; Dehoff, R. R.; Bridges, C. A.; Chi, M.; Guo, B.; Sun, X.-G. and Dai, S., "Self-organized amorphous TiO₂ nanotube arrays on porous Ti foam for rechargeable lithium and sodium ion batteries", *J. Power Sources*, **2013**, 222, 461-466
 282. Shin, J.-Y.; Samuelis, D. and Maier, J., "Sustained Lithium-Storage Performance of Hierarchical, Nanoporous Anatase TiO₂ at High Rates: Emphasis on Interfacial Storage Phenomena", *Adv. Funct. Mater.*, **2011**, 21, 3464-3472
 283. Wang, L.; Wu, X. and Zhang, S., "Electrochemical Properties of Highly Ordered

- TiO₂ Nanotube Arrays as an Anode Material for Lithium-ion Batteries", *Applied Mechanics and Materials*, **2012**, 130, 1281
284. Borghols, W. J. H.; Lützenkirchen-Hecht, D.; Haake, U.; Chan, W.; Lafont, U.; Kelder, E. M.; van Eck, E. R. H.; Kentgens, A. P. M.; Mulder, F. M. and Wagemaker, M., "Lithium Storage in Amorphous TiO₂ Nanoparticles", *J. Electrochem. Soc.*, **2010**, 157, A582-A588
 285. Gao, X. P.; Lan, Y.; Zhu, H. Y.; Liu, J. W.; Ge, Y. P.; Wu, F. and Song, D. Y., "Electrochemical Performance of Anatase Nanotubes Converted from Protonated Titanate Hydrate Nanotubes", *Electrochem. Solid-State Lett.*, **2005**, 8, A26-A29
 286. Okamoto, H., "The Li-Si (Lithium-Silicon) system", *Journal of Phase Equilibria*, **1990**, 11, 306-312
 287. Limthongkul, P.; Jang, Y.-I.; Dudney, N. J. and Chiang, Y.-M., "Electrochemically-driven solid-state amorphization in lithium-silicon alloys and implications for lithium storage", *Acta Mater.*, **2003**, 51, 1103-1113
 288. Key, B.; Morcrette, M.; Tarascon, J.-M. and Grey, C. P., "Pair Distribution Function Analysis and Solid State NMR Studies of Silicon Electrodes for Lithium Ion Batteries: Understanding the (De)lithiation Mechanisms", *J. Am. Chem. Soc.*, **2010**, 133, 503-512
 289. Kasavajjula, U.; Wang, C. and Appleby, A. J., "Nano- and bulk-silicon-based insertion anodes for lithium-ion secondary cells", *J. Power Sources*, **2007**, 163, 1003-1039
 290. Chan, C. K.; Peng, H.; Liu, G.; McIlwrath, K.; Zhang, X. F.; Huggins, R. A. and Cui, Y., "High-performance lithium battery anodes using silicon nanowires", *Nat*

Nano, **2008**, 3, 31-35

291. Baggetto, L.; Niessen, R. A. H.; Roozeboom, F. and Notten, P. H. L., "High Energy Density All-Solid-State Batteries: A Challenging Concept Towards 3D Integration", *Adv. Funct. Mater.*, **2008**, 18, 1057-1066
292. Yang, J.; Winter, M. and Besenhard, J. O., "Small particle size multiphase Li-alloy anodes for lithium-ionbatteries", *Solid State Ionics*, **1996**, 90, 281-287
293. Lee, S. W.; McDowell, M. T.; Choi, J. W. and Cui, Y., "Anomalous Shape Changes of Silicon Nanopillars by Electrochemical Lithiation", *Nano Lett.*, **2011**, 11, 3034-3039
294. Liu, X. H.; Zheng, H.; Zhong, L.; Huang, S.; Karki, K.; Zhang, L. Q.; Liu, Y.; Kushima, A.; Liang, W. T.; Wang, J. W.; Cho, J.-H.; Epstein, E.; Dayeh, S. A.; Picraux, S. T.; Zhu, T.; Li, J.; Sullivan, J. P.; Cumings, J.; Wang, C.; Mao, S. X.; Ye, Z. Z.; Zhang, S. and Huang, J. Y., "Anisotropic Swelling and Fracture of Silicon Nanowires during Lithiation", *Nano Lett.*, **2011**, 11, 3312-3318

Appendix A: The Delithiated and Electrical Behaviors of Individual Amorphous TiO₂ Nanotubes.

A.1. Delithiation Process of Amorphous TNTs

An individual a-TNT was delithiated inside the TEM as shown in Figure A.1(a-d) by reversing the applied bias on the lithiated nanotube. The green arrows in Figure A.1 indicate that the Li₂O layer gradually disappeared during the delithiation process. However, small traces of Li₂O left on the surface after delithiation could be still detected. Furthermore, as illustrated in Figure A.1(e-f), following delithiation, some of the crystalline particles still remained in the amorphous matrix, indicating that part of Li ions are trapped as crystalline phase in the amorphous matrix. This observation provides clues for explaining the irreversible capacity loss that has been reported following the first charge-discharge cycle of amorphous TiO₂ materials.^{4, 32, 259, 281-285} The EELS results illustrated in Figure A.1(g-h) provide detailed evidence on the structural and chemical evolution of the materials following delithiation. In Figure A.1(g), the two energy loss positions of Ti *L* edge after delithiation shifted back to the positions that were similar to the ones of the pristine, indicating the valence of Ti³⁺ oxidized to Ti⁴⁺. The two peaks of the energy loss became a little broad than the pristine due to the small amount of Ti^{4-x} (Li_xTiO₂) remaining in the amorphous matrix, indicating not all Li ions were delithiated. According to Figure A.1(h), the energy loss positions of O *K* edge after delithiation were between the ones of the pristine and lithiated, but more close to the pristine. As previous discussion, the separation distance of the two peaks **(i)** and **(ii)** represents the valence of

Ti. When the valence of Ti^{4+} reduces to Ti^{3+} , the separation will decrease. From the delithiated nanotube, one can notice that the distance of (i) and (ii) increased, indicating the Ti^{3+} oxidized to Ti^{4+} . However, they were not totally the same as the ones of the pristine, demonstrating not all Ti ions are in 4^+ valences after delithiation. In addition, the main peak (ii) of the energy loss became broad and small that was closer to the one of the pristine, indicating most of Li_2O disappeared after delithiation.

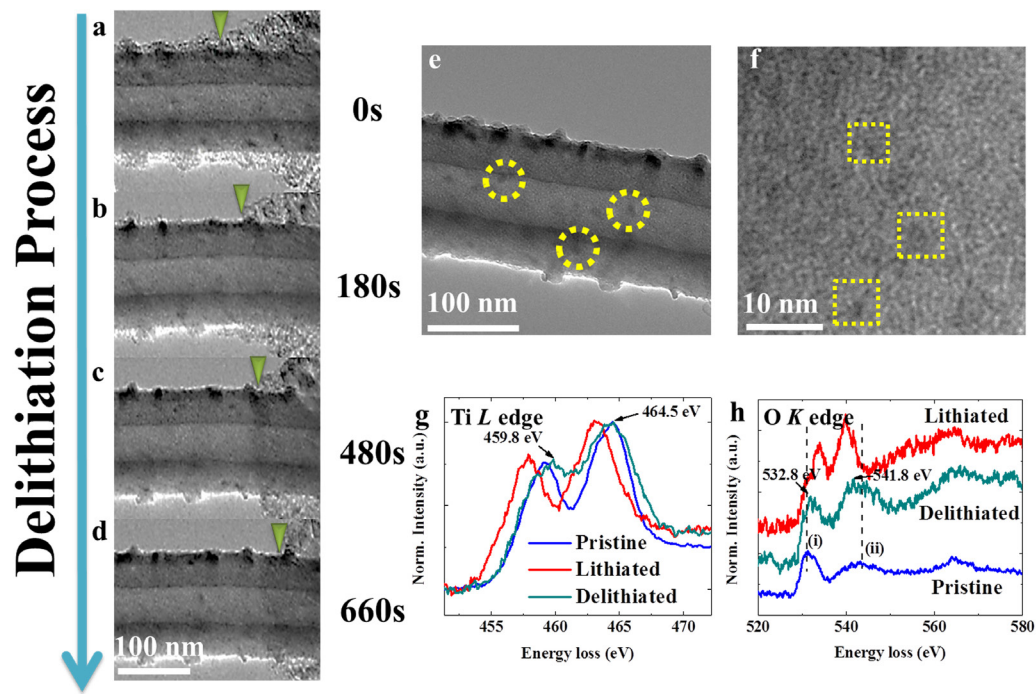


Figure A.1 Snapshot images of the delithiation process for a selected area of a-TNT. (a-d) Delithiation process monitored from beginning (0s) to end (660s). (e-f) The high-magnification TEM images of delithiated an a-TNT show the existence of particles in the amorphous matrix. (g-h) EELS spectrums of Ti *L* edge and O *K* edge after delithiation are compared with the same signals from pristine and lithiated nanotubes, respectively.

A.2. Electrical Behavior of Amorphous TNTs

To further investigate the effect of structural changes on the physical behavior of nanotubes, the electrical conductivity of nanotubes at various states of lithiation/delithiation was recorded (Figure A.2). The pristine a-TNT (black curve) behaved like a semiconductor with low electrical conductivity where only ~50 nA current could be detected at the applied voltage of ± 25 V. Interestingly, after the first lithiation (red curve), the conductivity of the lithiated nanotube increased to 150 nA at the applied voltage of ± 25 V, which is ~300% increase in comparison to the unlithiated nanotube. This enhancement in electrical conductivity can be correlated to the presence of Li ions in the matrix and the formation of crystalline islands of $\text{Li}_2\text{Ti}_2\text{O}_4$. Compared with disordered structures, the atomic ordering can assist the electrons transport in the nanotube.³² After delithiating the nanotube, the electrical conductivity (blue curve) decreased to a level below the fully lithiated nanotube (~100 nA at ± 25 V) as expected. However, the conductivity is still higher than the pristine (unlithiated) case. During delithiation, even though the Li ions would be extracted from crystalline islands ($\text{Li}_2\text{Ti}_2\text{O}_4$), the structure still remained ordered to help increase the electrical conductivity instead of becoming disordered. However, the improvement in the electrical conductivity during the first lithiation/delithiation cycle did not happen at subsequent cycles. In the second lithiation (green curve) and delithiation (pink curve), the electrical conductivity did not vary significantly, indicating that the formation of crystalline islands during lithiation played a key role in increasing the electrical conductivity of lithiated nanotubes.

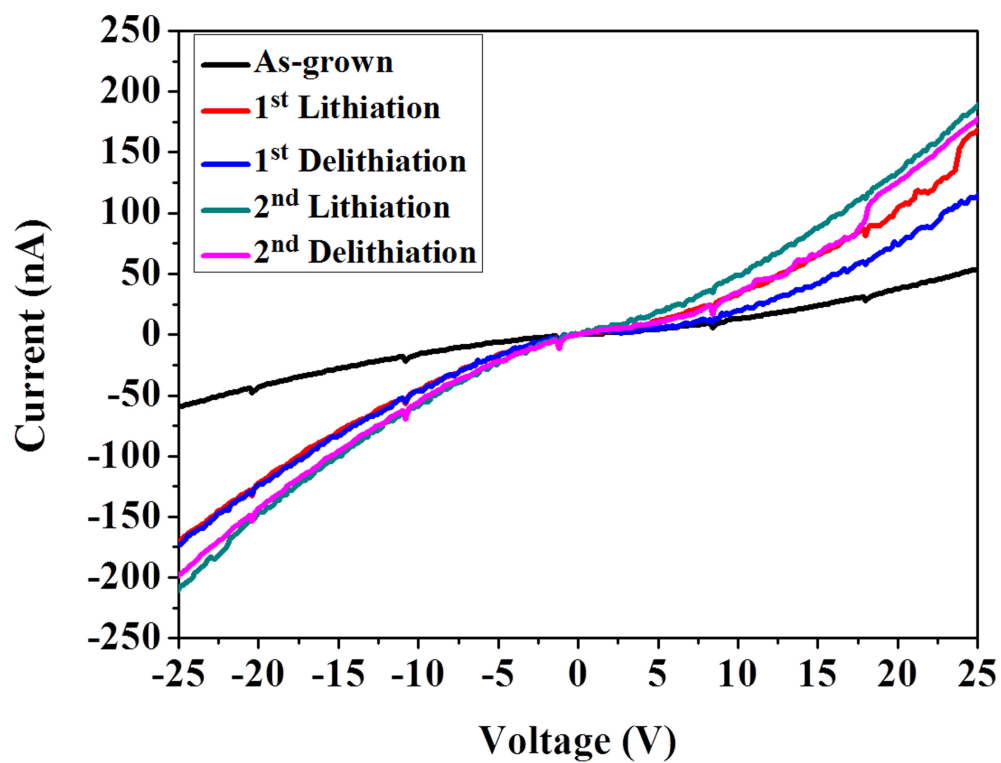
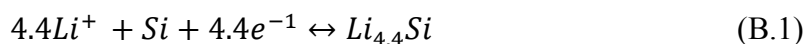


Figure A.2 *I-V* curves of an individual a-TNT under the bias ranging from -25 V to 25 V. Each color represents the nanotube in different states: As-grown (black), 1st lithiation (red), 1st delithiation (blue), 2nd lithiation (green), and 2nd delithiation (pink).

Appendix B: The Electrochemical Property of Si Nanowires

Silicon has attracted much more attention in the battery field based on its high theoretical capacity of 4200 mAh/g for lithium storage when fully lithiated ($\text{Li}_{4.4}\text{Si}$).²⁸⁶ Unlike the traditional anodic graphite with the low capacity of 372 mAh/g that can only accommodate 1/6 lithium atom (LiC_6) after fully charging, Si has the highest capacity in theory among all the potential anode materials. It has been reported that Si can have the capacity of 3579 mAhg⁻¹ in the form of $\text{Li}_{15}\text{Si}_4$ at room temperature and 4212 mAhg⁻¹ in the form of $\text{Li}_{22}\text{Si}_5$ at high temperature.²⁸⁷⁻²⁸⁹ Since Dr. Cui invented the silicon nanowire battery in 2007,²⁹⁰ silicon nanowire has been the most promising candidate as an anode material for lithium ion batteries rather than other types like powder and thin film. The nanowire has its unique properties as an anode, which powder and thin film do not have. It has certain facile strength relaxation because of small nanowire diameter for large volume expansion without the initial fracture that happens in powder or thin film, provides straight electronic path way for transportation, directly contact between nanowire and current collector to increase the conductivity and large surface area for sufficient lithium ions interaction.²⁹⁰ The mechanism of lithiation for silicon nanowires can be expressed as the Equation (B.1):



In theory, one-dimensional Si nanowires can help to accommodate with lateral strains from lithium interaction to improve the capacity retention. However, experimental results²⁸⁹ show the poor cycling retention due to the fracture and pulverization caused by

large volume expansion when charging. The volume expansion after lithium intercalation can be up to 300%^{291, 292} to 400%²⁹⁰ due to the formation of various Li_xSi , which leads to induce large stress on the nanowires to cause fracture and capacity fading after the first several cycles of lithiation/delithiation.

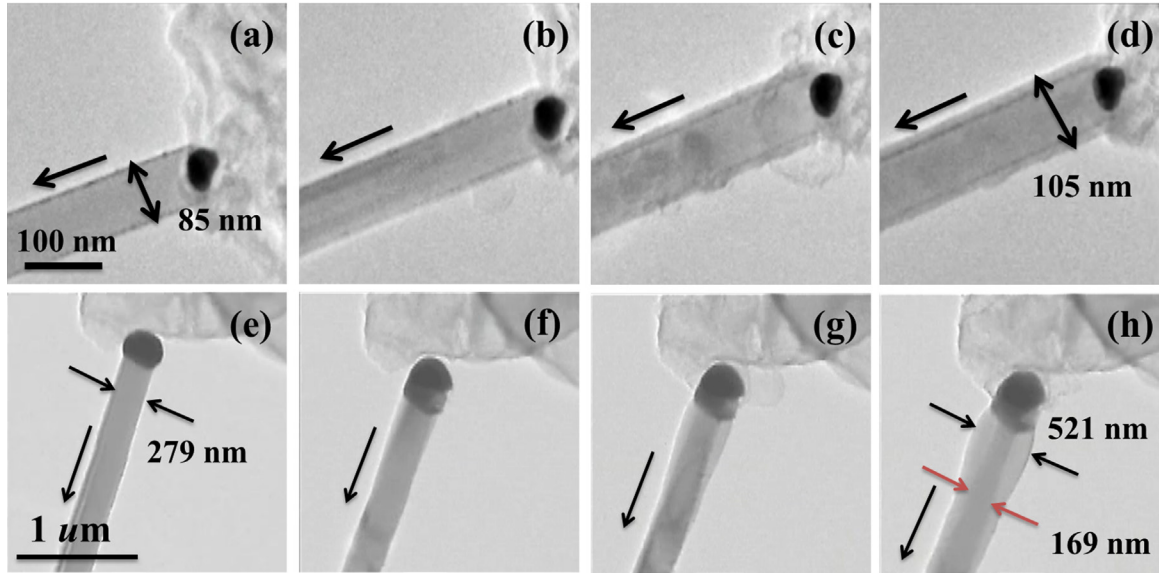


Figure B.1 The volume expansion behavior of two different crystallographic orientations of Si nanowires. (a-d) isotropic volume expansion of individual Si nanowire with $\langle 111 \rangle$ orientation. (e-h) Anisotropic volume expansion of individual Si nanowire with $\langle 112 \rangle$ orientation.

The lithiation processes of single Si nanowires with two different crystallographic orientations were studied in Figure B.1. The Si nanowire with $\langle 111 \rangle$ orientation is shown in Figure B. 1(a-d). The nanowire showed an isotropic volume expansion and the diameter increased from 85 nm to 105 nm in radial direction. Another nanowire with $\langle 112 \rangle$ orientation is also studied in Figure B.1(e-h). Comparing with the one of $\langle 111 \rangle$, however, the $\langle 112 \rangle$ nanowire had an anisotropic volume expansion and the diameter

increased from 279 nm to 521 nm. At the same time, the intrinsic core shrank to 169 nm. The experimental results showed that the preference of lithiation direction was different in various crystallographic orientations of Si nanowires and $[110]$ were the most preferred direction for the diffusion of lithium ions. Large volume expansions were observed during lithiation along (110) planes. Figure B.2 summarized the volume expansion direction of various crystallographic orientations of Si nanowires.

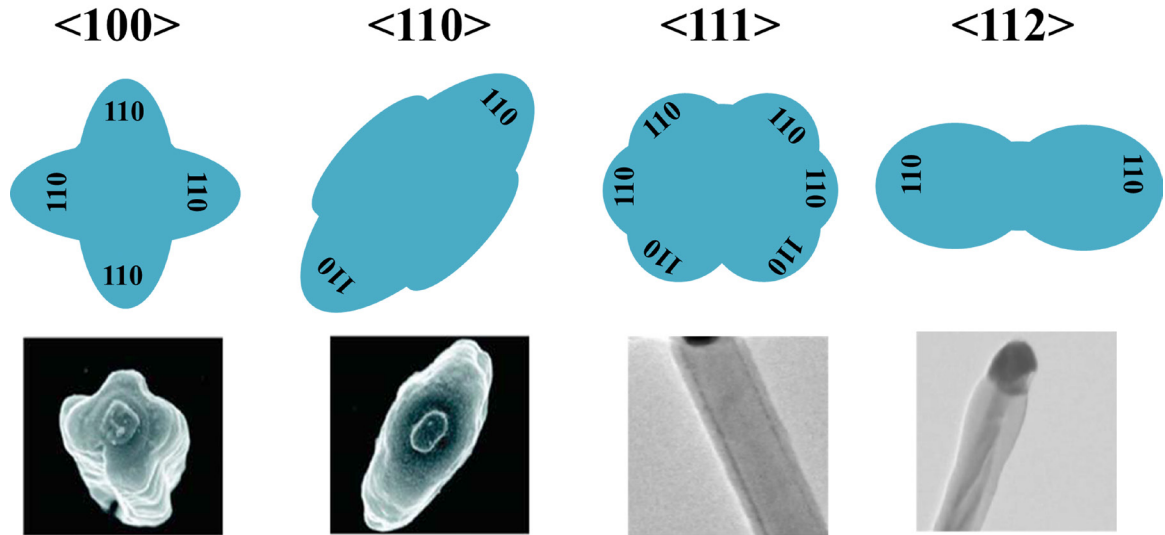


Figure B.2 The cross section of various crystallographic orientations of Si nanowires with corresponding volume expansion of lithiated $\langle 100 \rangle$,^{293, 294} $\langle 110 \rangle$,^{293, 294} $\langle 111 \rangle$, and $\langle 112 \rangle$ nanowires.

The delithiation process was conducted as shown in Figure B.3. The diameter of the nanowire became its original value of 85 nm. The *in situ* electrochemistry results indicated that the charge and discharge could be successfully accomplished.

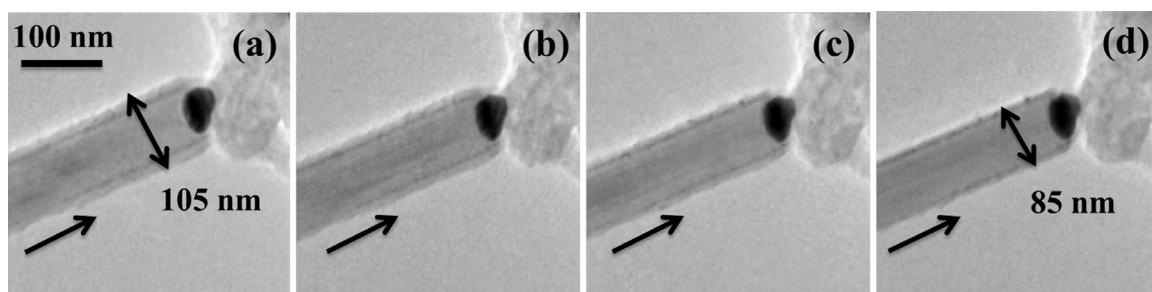
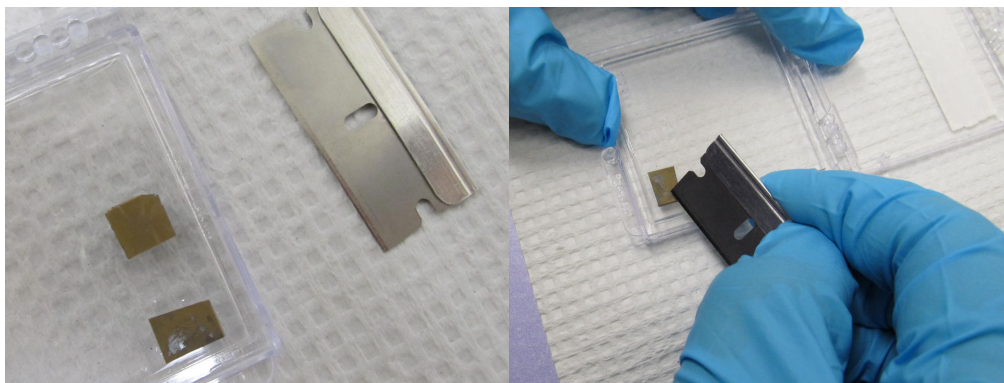


Figure B.3 The delithiation process of individual Si nanowire. (a-d) shows the diameter of the nanowire shrunk back its original 85 nm.

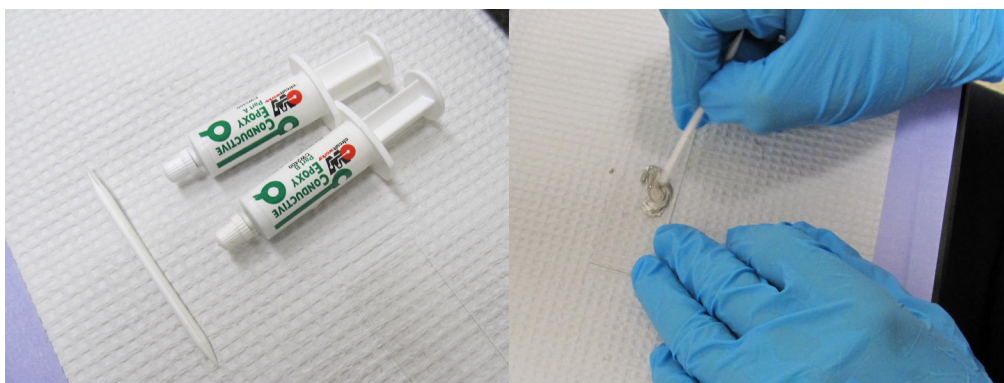
Appendix C: *In Situ* TEM Operation Procedure

C.1. Sample Preparation

1. Scratch the sample surface (TiO_2 , SiNW, *et al.*) by the razor to get some powders.



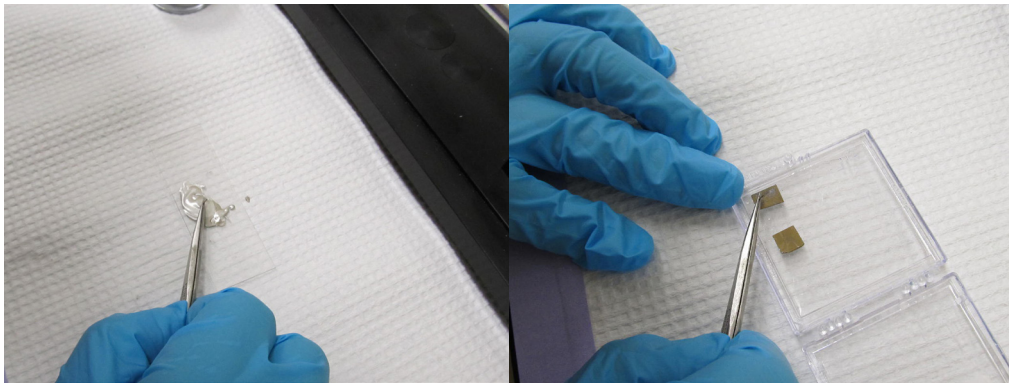
2. Squeeze little, equally amount of conductive epoxy (a) and (b) to the glass slide.
Mix (a) and (b) together by the rod.



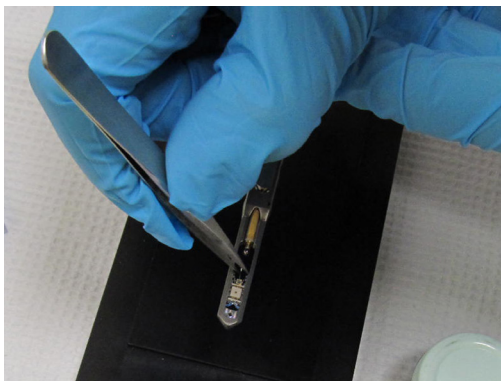
3. Loosen the screw on the STM tip and take the tip out by a straight-top tweezer.



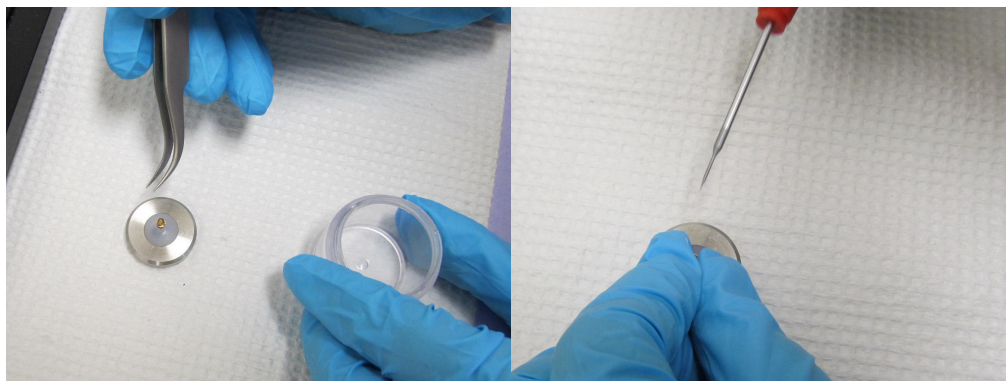
4. Attach the STM tip to the mixed epoxy then touch the powers, which have been scratch from sample.



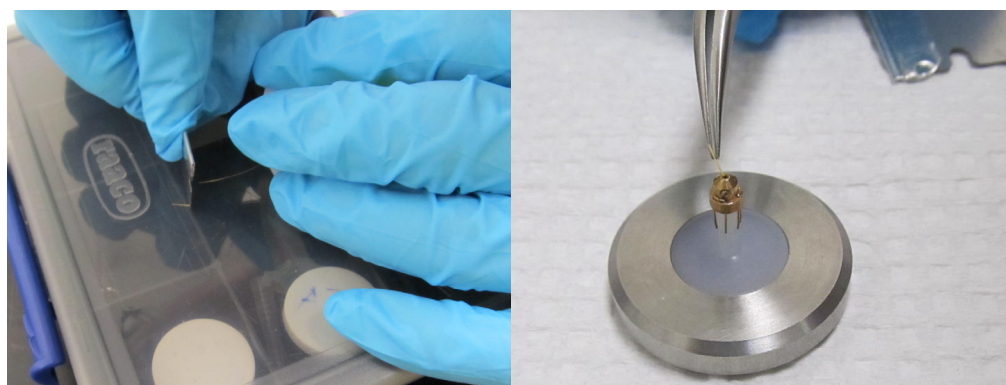
5. Put the STM tip back and tighten the screw



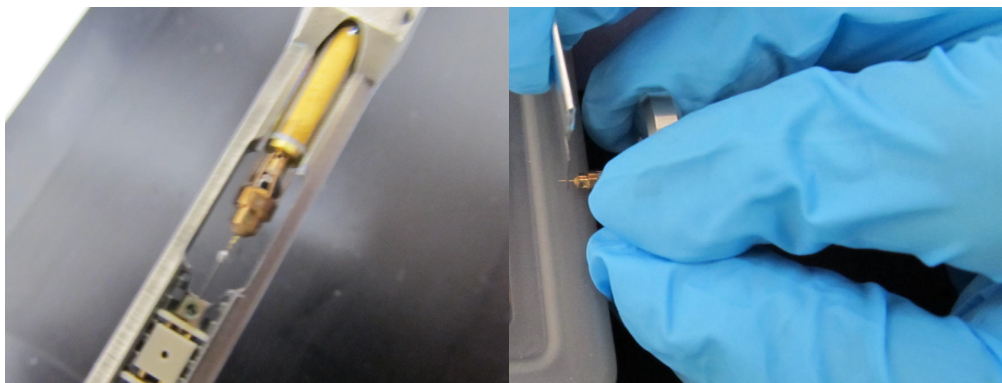
6. Hold one side of the hat and loosen the screw on the side by one round. Then repeat the same procedure to loosen the screw on the other side.



7. Take out the wasted gold wire by tweezer and cut another estimated long new gold wire, then put the wire into the hat. After that, tighten the two screws to make sure the gold wire is stable on the hat.

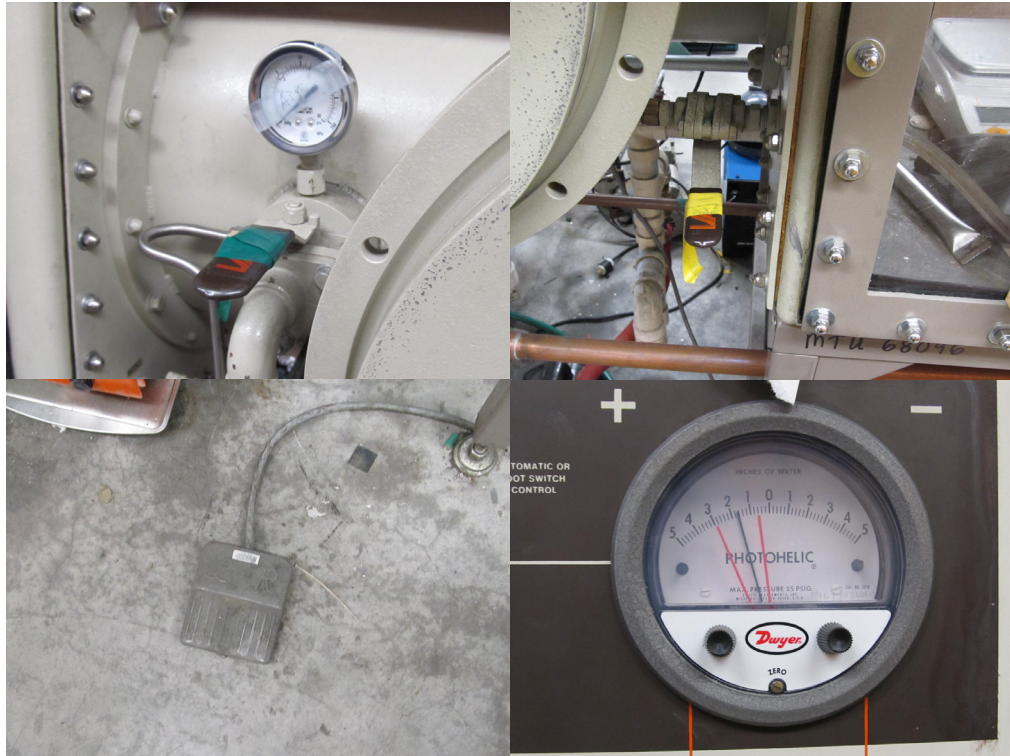


8. Mount the hat by curved-top tweezer and then check the length of the gold wire. If it is short that is far from the STM tip, it will need to prepare another one. If it is long, take the hat out, cut the longer part to make the gold wire as close as it can to the STM tip.

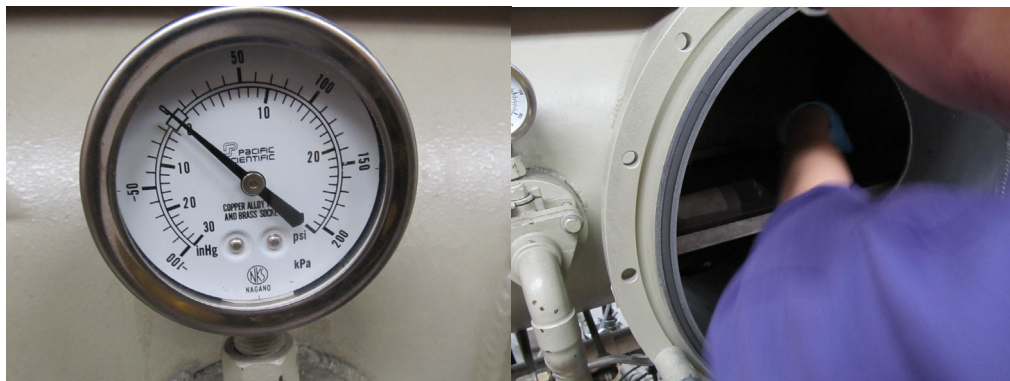


C.2. Glove Box Operation

1. Take the hat with its base into the container and cover it. Bring the container and a tweezer to the glove box.
2. Close the pump valve to stop pumping in the chamber. Then, open the valve that is connected to glove box to input Ar gas to the chamber. At the same time, push panel on the ground to make sure more Ar gas will be induced to the chamber. The indicator on the station can be raised in the range of 2-3.



3. After the indicated arrow pointing 0 for the pressure in the chamber, open the chamber and put the tweezer and container (uncovered) inside.



4. Close the chamber and reopen the pump valve to pump the air inside the chamber. It will last 10-15 minutes for the best condition.



5. Repeat step 2 until the indicator in the pump points to 0. Open the door inside the glove box and transfer the tweezer and container in the glove box.



6. Take the hat with its base at the same time to make sure that the hat sits tightly on the base. One hand holds the base and the other hand holds the Li metal. Scratch the tip of the gold wire on the surface of the metal slightly. After the Li sticks on the tip of the gold wire, put back the Li metal and covers the glass bottle. Put the hat with its base back to the container and cover it. Transfer the container and tweezer back to the chamber. Close the door in the glove box.



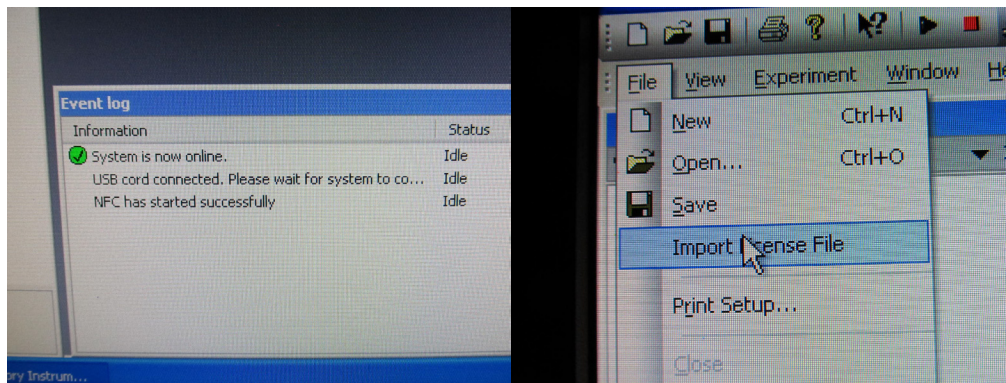
7. Open the chamber and take out the container and tweezer. Turn on the pump station by switching the valve. Take the container back to the TEM room.

C.3. Nanofactory Software Setup

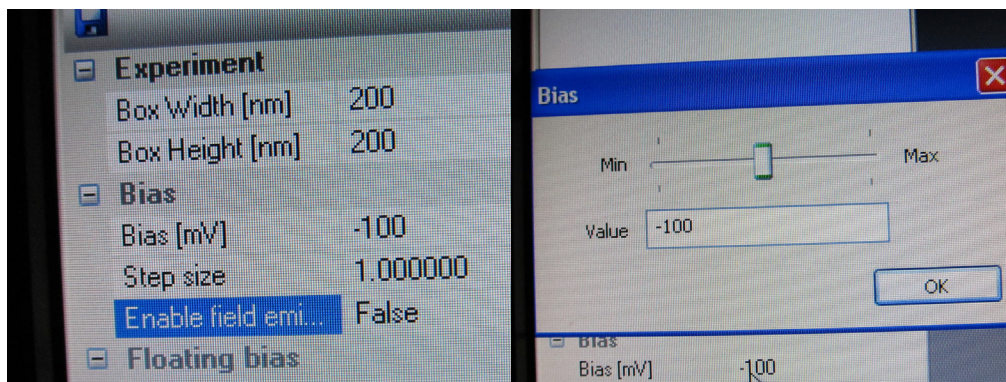
1. Clean the tweezer and container. Take out the hat quickly and mount it on the ball as quickly as possible.
2. Load the in situ holder into the TEM chamber and wait for the vacuum pumping. After inserting the holder, connect the Nanofactory wires on the holder.



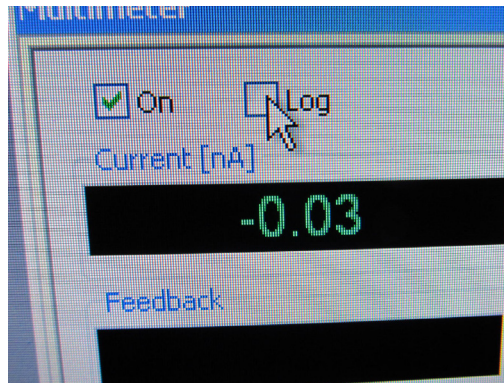
3. Open the software Nanofactory 3 and check whether the wires are connected well.
Then, click the file and select the Import License File, for example, STM File.



4. For applying voltage, enable the field emission option (clicking twice and press enter) and adjust the needed voltage value.



5. To record current, click the log option and the current will be recorded in text file.



6. For IV measurement, click the coordination option and select the (0,0) point. A new coordinate window will show up. Right click on the coordinate option and select Add Point Capture option, an empty IV plot will show up. Click on the Add Point Capture to set the starting and ending voltage (clicking twice and press enter), holding time before starting the test, points on the sample, and range of the current on the y axis. After setting done, click on the start option to measure the IV curve.

The screenshot displays a software interface with three main panels on the left and a large table on the right.

Coordinate explorer (top left): Shows a graph with a red dot at the origin (0.00:0.00).

Workspace explorer (middle left): Shows a tree view with 'Workspace' containing 'License Options' and 'Experiment'. A context menu is open over 'Experiment' with options: 'Add Point Capture', 'Add Image Capture', 'Add Script', and 'Remove'.

Workspace explorer (bottom left): Shows the same tree view, but now 'Coordinate (0.00, 0.00)' is listed under 'Experiment'.

anofactory Instruments - Point (bottom left): A toolbar with icons for file operations and a menu bar with 'View', 'Experiment', and 'Window'.

Members (right): A table listing properties for 'PointCapture1'.

Name	PointCapture1
Exclude	False
Order number	1
Relative	False
Start [mV]	-100.000000
Stop [mV]	100.000000
Acquisition time ...	100
Samples	400
Settling time [ms]	0
Input channel	Current
Output channel	Bias
Dual slope	False
Soft reset	True
Hold time [ms]	0
Processor	
Average number	1
Derivative	-None-
Best fit window	2
Curve specific	
Auto scale	True
Zoom start	-100.000000

Appendix D: Copyright Permissions



LICENSES FOR FIGURE 1.2

This is a License Agreement between Qi Gao ("You") and Nature Publishing Group ("Nature Publishing Group") provided by Copyright Clearance Center ("CCC"). The license consists of your order details, the terms and conditions provided by Nature Publishing Group, and the payment terms and conditions.


All payments must be made in full to CCC. For payment instructions, please see information listed at the bottom of this form.

License Number	3177210224222
License date	Jun 27, 2013
Licensed content publisher	Nature Publishing Group
Licensed content publication	Nature
Licensed content title	Issues and challenges facing rechargeable lithium batteries
Licensed content author	J.-M. Tarascon and M. Armand
Licensed content date	Nov 15, 2001
Volume number	414
Issue number	6861
Type of Use	reuse in a thesis/dissertation
Requestor type	academic/educational
Format	print and electronic
Portion	figures/tables/illustrations
Number of figures/tables/illustrations	1
Figures	Figure 1: Comparison of the different battery technologies in terms of volumetric and gravimetric energy density.
Author of this NPG article	no
Your reference number	
Title of your thesis / dissertation	Nanoscale Electrochemistry by In-Situ Transmission Electron Microscopy
Expected completion date	Jun 2013
Estimated size (number of pages)	200
Total	0.00 USD

LICENSES FOR FIGURE 1.4



[Home](#)[Account Info](#)[Help](#)



ACS Publications
High quality. High impact.

Title: Effect of Concentration on the Energetics and Dynamics of Li Ion Transport in Anatase and Amorphous TiO₂

Author: Handan Yildirim, Jeffrey Greeley, and Subramanian K. R. S. Sankaranarayanan

Publication: The Journal of Physical Chemistry C

Publisher: American Chemical Society

Date: Aug 1, 2011

Copyright © 2011, American Chemical Society

Logged in as:
Qi Gao
Account #: 3000658403

[LOGOUT](#)

PERMISSION/LICENSE IS GRANTED FOR YOUR ORDER AT NO CHARGE

This type of permission/license, instead of the standard Terms & Conditions, is sent to you because no fee is being charged for your order. Please note the following:

- Permission is granted for your request in both print and electronic formats, and translations.
- If figures and/or tables were requested, they may be adapted or used in part.
- Please print this page for your records and send a copy of it to your publisher/graduate school.
- Appropriate credit for the requested material should be given as follows: "Reprinted (adapted) with permission from (COMPLETE REFERENCE CITATION). Copyright (YEAR) American Chemical Society." Insert appropriate information in place of the capitalized words.
- One-time permission is granted only for the use specified in your request. No additional uses are granted (such as derivative works or other editions). For any other uses, please submit a new request.

LICENSES FOR FIGURE 1.6

Permission Request

Permissions <permissions@iop.org>
To: Qi Gao <qgao@mtu.edu>

Mon, Jul 1, 2013 at 5:44 AM

Dear Qi Gao,

Thank you for your request to reproduce IOP Publishing material.

We are happy to grant permission for the use you request on the terms set out below.

If you have any questions, please feel free to contact our Permissions team at permissions@iop.org.

I wish you the best of luck with the completion of your thesis.

Kind regards,

Laura Sharples

Rights & Permissions Officer
IOP Publishing Ltd
Temple Circus, Temple Way, Bristol BS1 6HG

T: +44 (0)117 930 1001

F: +44 (0)117 920 0997

[What do scientific publishers do?](#)

Conditions

Non-exclusive, non-transferrable, revocable, worldwide, permission to use the material in print and electronic form will be granted **subject to the following conditions:**

- Permission will be cancelled without notice if you fail to fulfil any of the conditions of this letter.
- You will make reasonable efforts to contact the author(s) to seek consent for your intended use. Contacting one author acting expressly as authorised agent for their co-authors is acceptable.
- You will reproduce the following prominently alongside the material:
 - o the source of the material, including author, article title, title of journal, volume number, issue number (if relevant), page range (or first page if this is the only information available) and date of first publication
 - o for material being published electronically, a link back to the article (via DOI)
 - o if practical and IN ALL CASES for works published under any of the Creative Commons licences the words "© IOP Publishing. All rights reserved"
- The material will not, without the express permission of the author(s), be used in any way which, in the opinion of IOP Publishing, could distort or alter the author(s)' original intention(s) and meaning, be prejudicial to the honour or reputation of the author(s) and/or imply endorsement by the author(s) and/or IOP Publishing.
- Payment of £0 is received in full by IOP Publishing prior to use.

Please note: IOP does not usually provide signed permission forms as a separate attachment. Please print this email and provide it to your publisher as proof of permission.

From: Qi Gao <qgao@mtu.edu>
To: permissions@iop.org,
Date: 27/06/2013 20:29
Subject: Permission Request

To whom it may concern,

I am writing this email to obtain your permission to reuse a figure in an article that is published in Nanotechnology. I am writing my dissertation and would like to reuse the figure in my PhD dissertation.

Below is the article information:

"Comparison of the rate capability of nanostructured amorphous and anatase TiO₂ for lithium insertion using anodic TiO₂ nanotube arrays"

Authors: Hai-Tao Fang, Min Lu, Da-Wei Wang, Tao Sun, Dong-Sheng Guan, Feng Li, Jigang Zhou, Tsun-Kong Sham and Hui-Ming Cheng

Source: Nanotechnology, Volume 20, 2009, pp. 225701

The figure I am going to use is: Figure 4 Tenth cycle charge-discharge curves of the amorphous ATNTA electrode.

The title of my thesis is "Nanoscale Electrochemistry by In-situ Transmission Electron Microscopy" and will be published in August 2013 in Michigan Technological University.

Please let me know if you need any further information regarding this request. I appreciate your attention,

Regards,

Qi Gao

This email (and attachments) are confidential and intended for the addressee(s) only. If you are not the intended recipient please notify the sender, delete any copies and do not take action in reliance on it. Any views expressed are the author's and do not represent those of IOP, except where specifically stated. IOP takes reasonable precautions to protect against viruses but accepts no responsibility for loss or damage arising from virus infection. For the protection of IOP's systems and staff emails are scanned automatically.

IOP Publishing Limited Registered in England under Registration No 467514. Registered Office: Temple Circus, Bristol BS1 6HG England Vat No GB 461 6000 84.

Please consider the environment before printing this email

LICENSES FOR CHAPTER 4

All payments must be made in full to CCC. For payment instructions, please see information listed at the bottom of this form.

License Number	3152610820297
Order Date	May 19, 2013
Publisher	American Institute of Physics
Publication	Journal of Applied Physics
Article Title	Structural instabilities in TiO ₂ nanotubes
Author	T. Shokuhfar, Q. Gao, A. Ashtana, K. Walzack, et al.
Online Publication Date	Nov 22, 2010
Volume number	108
Issue number	10
Type of Use	Thesis/Dissertation
Requestor type	Author (original article)
Format	Print and electronic
Portion	Excerpt (> 800 words)
Will you be translating?	No
Title of your thesis / dissertation	Nanoscale Electrochemistry by In-Situ Transmission Electron Microscopy
Expected completion date	Jun 2013
Estimated size (number of pages)	200
Total	0.00 USD

LICENSES FOR CHAPTER 5



Qi Gao <qgao@mtu.edu>

Re: Can I ask for reprint permission?

2 messages

nalwa@mindspring.com <nalwa@mindspring.com>
 Reply-To: nalwa@mindspring.com
 To: Qi Gao <qgao@mtu.edu>

Tue, Jul 23, 2013 at 12:04 PM

Dear Dr. Gao:

American Scientific Publishers grants you permission to reuse the following article in your PhD thesis (Nanoscale Electrochemistry by In-situ Transmission Electron Microscopy) after citing full reference.

"A Real Time Observation of Phase Transition of Anatase TiO₂ Nanotubes Into Rutile Nanoparticles by In-Situ Joule Heating Inside Transmission Electron Microscope"

Authors: Asthana, A.; Shokuhfar, T.; Gao, Q.; Heiden, P.A.; Friedrich, C.; Yassar, R.S.

Source: Advanced Science Letters, Volume 3, Number 4, December 2010 , pp. 557-562(6)

Best wishes,

H. S. Nalwa

—Original Message—

From: Qi Gao
 Sent: Jul 23, 2013 9:00 AM
 To: science@aspbs.com
 Subject: Can I ask for reprint permission?

Dear Editor-in Chief Prof. Nalwa,
 I am writing this email to obtain your permission to reuse an article that is published in Advanced Science Letters. I am a co-author for this article and I would like to reuse this in my PhD thesis.

Below is the article information:

"A Real Time Observation of Phase Transition of Anatase TiO₂ Nanotubes Into Rutile Nanoparticles by In-Situ Joule Heating Inside Transmission Electron Microscope"

Authors: Asthana, A.; Shokuhfar, T.; Gao, Q.; Heiden, P.A.; Friedrich, C.; Yassar, R.S.

Source: Advanced Science Letters, Volume 3, Number 4, December 2010 , pp. 557-562(6)

The title of my thesis is "Nanoscale Electrochemistry by In-situ Transmission Electron Microscopy" and will be published in August 2013.

Please let me know if you need any further information regarding this request. I appreciate your attention,

Regards,
Qi Gao

LICENSES FOR CHAPTER 6

All payments must be made in full to CCC. For payment instructions, please see information listed at the bottom of this form.

License Number	3174580278371
Order Date	Jun 23, 2013
Publisher	American Institute of Physics
Publication	Applied Physics Letters
Article Title	A study on the modulation of the electrical transport by mechanical straining of individual titanium dioxide nanotube
Author	A. Asthana, T. Shokuhfar, Q. Gao, P. Heiden, et al.
Online Publication Date	Aug 17, 2010
Volume number	97
Issue number	7
Type of Use	Thesis/Dissertation
Requestor type	Author (original article)
Format	Print and electronic
Portion	Excerpt (> 800 words)
Will you be translating?	No
Title of your thesis / dissertation	Nanoscale Electrochemistry by In-Situ Transmission Electron Microscopy
Expected completion date	Jun 2013
Estimated size (number of pages)	200
Total	0.00 USD

LICENSES FOR CHAPTER 7

This is a License Agreement between Qi Gao ("You") and Springer ("Springer") provided by Copyright Clearance Center ("CCC"). The license consists of your order details, the terms and conditions provided by Springer, and the payment terms and conditions.

All payments must be made in full to CCC. For payment instructions, please see information listed at the bottom of this form.

License Number	3174601324235
License date	Jun 23, 2013
Licensed content publisher	Springer
Licensed content publication	Applied Physics A: Materials Science & Processing
Licensed content title	Deformation-driven electrical transport in amorphous TiO ₂ nanotubes
Licensed content author	A. Asthana
Licensed content date	Jan 1, 2012
Volume number	109
Issue number	1
Type of Use	Thesis/Dissertation
Portion	Full text
Number of copies	1
Author of this Springer article	Yes and you are the sole author of the new work
Order reference number	
Title of your thesis / dissertation	Nanoscale Electrochemistry by In-Situ Transmission Electron Microscopy
Expected completion date	Jun 2013
Estimated size(pages)	200
Total	0.00 USD

LICENSES FOR FIGURE 10.1

This is a License Agreement between Qi Gao ("You") and Elsevier ("Elsevier") provided by Copyright Clearance Center ("CCC"). The license consists of your order details, the terms and conditions provided by Elsevier, and the payment terms and conditions.

All payments must be made in full to CCC. For payment instructions, please see information listed at the bottom of this form.

Supplier	Elsevier Limited The Boulevard, Langford Lane Kidlington, Oxford, OX5 1GB, UK
Registered Company Number	1982084
Customer name	Qi Gao
Customer address	1908 Woodmar Dr HOUGHTON, MI 49931
License number	3183391322521
License date	Jul 06, 2013
Licensed content publisher	Elsevier
Licensed content publication	Electrochimica Acta
Licensed content title	Electrochemical properties of anatase TiO ₂ nanotubes as an anode material for lithium-ion batteries
Licensed content author	Jinwei Xu, Caihong Jia, Bin Cao, W.F. Zhang
Licensed content date	1 November 2007
Licensed content volume number	52
Licensed content issue number	28
Number of pages	4
Start Page	8044
End Page	8047
Type of Use	reuse in a thesis/dissertation
Portion	figures/tables/illustrations
Number of figures/tables /illustrations	2
Format	both print and electronic
Are you the author of this Elsevier article?	No
Will you be translating?	No
Order reference number	
Title of your thesis/dissertation	NANOSCALE ELECTROCHEMISTRY BY IN-SITU TRANSMISSION ELECTRON MICROSCOPY
Expected completion date	Aug 2013

Estimated size (number of pages)	200
Elsevier VAT number	GB 494 6272 12
Permissions price	0.00 USD
VAT/Local Sales Tax	0.00 USD / 0.00 GBP
Total	0.00 USD

LICENSES FOR FIGURE 10.2(a-b)



RightsLink®

[Home](#)

[Account Info](#)

[Help](#)



ACS Publications
High quality. High impact.

Title: Lithium Coordination Sites in Li_xTiO₂(B): A Structural and Computational Study
Author: A. Robert Armstrong, Corinne Arrouvel, Valentina Gentili, Stephen C. Parker, M. Saiful Islam, and Peter G. Bruce

Publication: Chemistry of Materials

Publisher: American Chemical Society

Date: Dec 1, 2010

Copyright © 2010, American Chemical Society

Logged in as:

Qi Gao

Account #:

3000658403

[LOGOUT](#)

PERMISSION/LICENSE IS GRANTED FOR YOUR ORDER AT NO CHARGE

This type of permission/license, instead of the standard Terms & Conditions, is sent to you because no fee is being charged for your order. Please note the following:

- Permission is granted for your request in both print and electronic formats, and translations.
- If figures and/or tables were requested, they may be adapted or used in part.
- Please print this page for your records and send a copy of it to your publisher/graduate school.
- Appropriate credit for the requested material should be given as follows: "Reprinted (adapted) with permission from (COMPLETE REFERENCE CITATION). Copyright (YEAR) American Chemical Society." Insert appropriate information in place of the capitalized words.
- One-time permission is granted only for the use specified in your request. No additional uses are granted (such as derivative works or other editions). For any other uses, please submit a new request.

If credit is given to another source for the material you requested, permission must be obtained from that source.

LICENSES FOR FIGURE 10.2(c-d)

This is a License Agreement between Qi Gao ("You") and Elsevier ("Elsevier") provided by Copyright Clearance Center ("CCC"). The license consists of your order details, the terms and conditions provided by Elsevier, and the payment terms and conditions.

All payments must be made in full to CCC. For payment instructions, please see information listed at the bottom of this form.

Supplier	Elsevier Limited The Boulevard, Langford Lane Kidlington, Oxford, OX5 1GB, UK
Registered Company Number	1982084
Customer name	Qi Gao
Customer address	1908 Woodmar Dr HOUGHTON, MI 49931
License number	3183400648392
License date	Jul 06, 2013
Licensed content publisher	Elsevier
Licensed content publication	Journal of Solid State Chemistry
Licensed content title	Synthesis of titanate, TiO ₂ (B), and anatase TiO ₂ nanofibers from natural rutile sand
Licensed content author	Sorapong Pavasupree, Yoshikazu Suzuki, Susumu Yoshikawa, Ryoji Kawahata
Licensed content date	October 2005
Licensed content volume number	178
Licensed content issue number	10
Number of pages	7
Start Page	3110
End Page	3116
Type of Use	reuse in a thesis/dissertation
Intended publisher of new work	other
Portion	figures/tables/illustrations
Number of figures/tables /illustrations	1
Format	both print and electronic
Are you the author of this Elsevier article?	No
Will you be translating?	No
Order reference number	

Title of your thesis/dissertation	NANOSCALE ELECTROCHEMISTRY BY IN-SITU TRANSMISSION ELECTRON MICROSCOPY
Expected completion date	Aug 2013
Estimated size (number of pages)	200
Elsevier VAT number	GB 494 6272 12
Permissions price	0.00 USD
VAT/Local Sales Tax	0.00 USD / 0.00 GBP
Total	0.00 USD

LICENSES FOR FIGURE 10.3

This is a License Agreement between Qi Gao ("You") and John Wiley and Sons ("John Wiley and Sons") provided by Copyright Clearance Center ("CCC"). The license consists of your order details, the terms and conditions provided by John Wiley and Sons, and the payment terms and conditions.

All payments must be made in full to CCC. For payment instructions, please see information listed at the bottom of this form.

License Number	3183710557300
License date	Jul 07, 2013
Licensed content publisher	John Wiley and Sons
Licensed content publication	Advanced Materials
Licensed content title	Nanosheet-Constructed Porous TiO ₂ -B for Advanced Lithium Ion Batteries
Licensed copyright line	Copyright © 2012 WILEY-VCH Verlag GmbH & Co. KGaA, Weinheim
Licensed content author	Shaohua Liu,Haiping Jia,Lu Han,Julian Wang,Pengfei Gao,Dongdong Xu,Jun Yang,Shunai Che
Licensed content date	May 18, 2012
Start page	3201
End page	3204
Type of use	Dissertation/Thesis
Requestor type	University/Academic
Format	Print and electronic
Portion	Figure/table
Number of figures/tables	1
Original Wiley figure/table number(s)	Figure 4 (a) and (c)
Will you be translating?	No
Total	0.00 USD

LICENSES FOR FIGURE 10.4 (b-d)

This is a License Agreement between Qi Gao ("You") and Elsevier ("Elsevier") provided by Copyright Clearance Center ("CCC"). The license consists of your order details, the terms and conditions provided by Elsevier, and the payment terms and conditions.

All payments must be made in full to CCC. For payment instructions, please see information listed at the bottom of this form.

Supplier	Elsevier Limited The Boulevard, Langford Lane Kidlington, Oxford, OX5 1GB, UK
Registered Company Number	1982084
Customer name	Qi Gao
Customer address	1908 Woodmar Dr HOUGHTON, MI 49931
License number	3183711264979
License date	Jul 07, 2013
Licensed content publisher	Elsevier
Licensed content publication	Journal of Crystal Growth
Licensed content title	Large-scale synthesis of single-crystalline rutile TiO ₂ nanorods via a one-step solution route
Licensed content author	Xiangping Huang, Chunxu Pan
Licensed content date	1 August 2007
Licensed content volume number	306
Licensed content issue number	1
Number of pages	6
Start Page	117
End Page	122
Type of Use	reuse in a thesis/dissertation
Intended publisher of new work	other
Portion	figures/tables/illustrations
Number of figures/tables /illustrations	1
Format	both print and electronic
Are you the author of this Elsevier article?	No
Will you be translating?	No
Order reference number	

Title of your thesis/dissertation	NANOSCALE ELECTROCHEMISTRY BY IN-SITU TRANSMISSION ELECTRON MICROSCOPY
Expected completion date	Aug 2013
Estimated size (number of pages)	200
Elsevier VAT number	GB 494 6272 12
Permissions price	0.00 USD
VAT/Local Sales Tax	0.00 USD / 0.00 GBP
Total	0.00 USD

LICENSES FOR FIGURE 10.4(e-f)

This is a License Agreement between Qi Gao ("You") and John Wiley and Sons ("John Wiley and Sons") provided by Copyright Clearance Center ("CCC"). The license consists of your order details, the terms and conditions provided by John Wiley and Sons, and the payment terms and conditions.

All payments must be made in full to CCC. For payment instructions, please see information listed at the bottom of this form.

License Number	3183720475881
License date	Jul 07, 2013
Licensed content publisher	John Wiley and Sons
Licensed content publication	Advanced Materials
Licensed content title	High Lithium Electroactivity of Nanometer-Sized Rutile TiO ₂
Licensed copyright line	Copyright © 2006 WILEY-VCH Verlag GmbH & Co. KGaA, Weinheim
Licensed content author	Y.-S. Hu, L. Kienle, Y.-G. Guo, J. Maier
Licensed content date	Apr 10, 2006
Start page	1421
End page	1426
Type of use	Dissertation/Thesis
Requestor type	University/Academic
Format	Print and electronic
Portion	Figure/table
Number of figures/tables	2
Original Wiley figure/table number(s)	Figure 2(a) Figure 5
Will you be translating?	No
Total	0.00 USD